ABSTRACT

Title of dissertation: ATOMIC LAYER DEPOSITION OF CADMIUM TELLURIDE FOR THE PASSIVATION OF MERCURY CADMIUM TELLURIDE

James W. Pattison, Doctor of Philosophy 2021

Dissertation directed by: Prof. Lourdes Salamanca-Riba
Department of Materials Science & Engineering

Mercury cadmium telluride (MCT) is an important infrared (IR) detector material due to high quantum efficiency and the ability to tune the bandgap, covering important IR wavelengths from near-infrared (~1 μm) to very-long wavelength infrared (>12 μm) detection. Focal Plane Arrays (FPAs) are used to image in the infrared and consist of photodiodes that absorb IR photons, generating charge carriers that create an electric signal used to form an image by combining the signals from all of the photodiodes. Decreasing photodiode size increases the resolution of optical systems incorporating MCT FPAs, but challenges current state-of-the-art passivation processes. Passivation is needed to increase the signal-to-noise of a system by rendering benign the charge carrier transport. Physical-vapor-deposited (PVD) CdTe is the incumbent passivation material for MCT, but fails when applied to the next generation of MCT photodiodes because of non-conformal deposition. Atomic layer deposition (ALD) is a superior deposition technique in this regard because the vapor-phase chemicals enable conformal exposure of the surface as opposed to line-of-sight deposition in PVD. ALD of CdTe requires deposition temperature lowering to suppress out-gassing of Hg at elevated temperature, which leads to mercury vacancy formation, reducing signal-to-noise of any eventual detector. Previous demonstration of CdTe ALD was spontaneous above ~200 °C for chemisorbed dimethylcadmium (DMCd) to react with diethyltellurium (DETe). However, this temperature is incompatible with MCT devices, because of the loss of Hg from the material. This dissertation attempts to overcome the low temperature requirement of current CdTe ALD using a novel approach in which argon plasma successfully decomposes the chemisorbed DMCd, replacing temperature induced thermal decomposition, and induced CdTe growth using either DETe or bis(trimethylsilyl)telluride as the tellurium precursors at low temperatures. Film deposition conditions were developed through deposition on silicon substrates, and the process was transferred to MCT samples, demonstrating low temperature deposition, conformal deposition, and passivation of the MCT surface. The films were characterized by in-situ spectroscopic ellipsometry (SE), x-ray photoelectron spectroscopy (XPS), x-ray diffraction (XRD), and transmission electron microscopy (TEM). Photoconductive decay (PCD) measurements were made of MCT material passivated by CdTe ALD, demonstrating effective passivation through enhanced minority carrier lifetime.

ATOMIC LAYER DEPOSITION OF CADMIUM TELLURIDE FOR THE PASSIVATION OF MERCURY CADMIUM TELLURIDE

by

James Pattison

Dissertation submitted to the Faculty of the Graduate School of the
University of Maryland, College Park, in partial fulfillment
of the requirements for the degree of
Doctor of Philosophy
2021

Dissertation Committee:

Professor Lourdes Salamanca-Riba, Chair
Professor Neil Goldsman
Doctor Brenda VanMil
Professor Raymond Phaneuf
Professor Luz Martinez-Miranda

"Matter is plastic in the face of Mind." - Philip K. Dick

Acknowledgements

I would like to express my deep gratitude to my wife, Jessy Jean Brown-Pattison for her unwavering support during this very long journey: light and love.

I would like to express my deep gratitude to:

My advisor at University of Maryland, College Park, Prof. Lourdes Salamanca-Riba, for her guidance and patience during this difficult project and time in my life. Her direction on the project pushed me to be a better experimentalist, and her defect chemistry course is knowledge I use every single day as an MCT scientist.

My committee members Prof. Luz Martinez-Miranda for her patience and willingness to join at late notice from me, Prof. Neil Goldsman for his support and advice, and Prof. Raymond Phaneuf for his exacting critique, and his numerous conversations with me about surface science over the years.

My advisor at US Army Research Laboratory, Dr. Brenda VanMil for her friendship and handing off more than a bit of MOCVD lived experience to make me a better scientist. Thanks for being a good cubicle neighbor and teammate!

Dr. Priyalal Wijewarnasuriya for all the mentorship, MCT knowledge and deep friendship. More good times to come, even as we are now competitors!

Andy Hewitt for the AFM, deep philosophy in cube land and continued friendship.

Can't thank enough: Noel O'Toole and Bruce Rayner from KJLC for friendship and ALD wisdom.

Dr. Yuanping Chen for his friendship, continued collaboration and hard work to get me over the finish line with the CdTe ALD reactor and growths. I have learned so much about CdTe, but not enough, from him!

Rob Burke (Bobby Hustle) for friendship and our continued work with passing off of the CdTe ALD reactor!

Dr. Nibir Dhar for his support from DARPA MTO; my first teammates and friends Matt Chin and Dr. Barbara Nichols, my optoelectronics family Eric DeCuir, Yuanping Chen, Greg Brill, Wije, Kimberly Olver, Greg Meissner, Sina Simingalam; Kevin Doyle, Stuart Farrell, and Harry Hier, Ryan Enck. To my awesome leadership team that cheered me on during good times and bad: Meredith Reed, Anand Sampath, Paul Sunal, Phil Perconti, Keith Krappels. To Prof. Dave Smith, HsinWei Wu, and Brain Tracy from Arizona State University for all the TEM support. Thanks to Syed Qadri from Naval Research Lab for the XRD work. Very special thanks to Ishwara Bhat from Rensselaer Polytechnic Institute for teaching me about CdTe MOCVD through publications and through conversations over the years. Thanks to Raytheon folks during my conversion to factory research life: Chad Fulk, Dan Lofgreern, Eli Gordon, and Heater Leifeste.

Table of Contents

List of Tables

List of Figures

List of Abbreviations

acetyl bromide	AcBr
angle of incidence	AOI
US Army Research Laboratory	ARL
angle-resolved x-ray photoelectron spectroscopy	ARXPS
Arizona State University	ASU
atomic force microscopy	AFM
atomic layer deposition	ALD
binding energy	BE
bis(trimethylsilyl)telluride	BTMSTe
cadmium	Cd
cadmium telluride	CdTe
chemical vapor deposition	CVD
coefficient of thermal expansion	CTE
diethyltellurium	DETe
dimethylcadmium	DMCd
electron-hole	eh
focal plane array	FPA
generation-recombination	GR
growth per cycle	GPC
high-aspect ratio	HAR
inductively coupled plasma	ICP
infrared	IR
kinetic energies	KE
layer-by-layer	LBL
lifetime spectroscopy	LS
long-wave	LW
low-energy electron diffraction	LEED
mercury	Hg
mercury cadmium telluride	MCT
metal organic chemical vapor deposition	MOCVD
mid-wave	MW
molecular beam epitaxy	MBE
monomethylcadmium	MMCd
nanoparticle	NP
photoconductive decay	PCD
photoelectrons	PE
physical vapor deposition	PVD
plasma-assisted ald, or pa-	PA-ALD
radio frequency	RF

reflection high-energy electron diffraction	RHEED
relative sensitivity factor	RSF
Shockley-Read-all recombination	SRH
signal-to-noise	SNR
spectroscopic ellipsometer/ellipsometry	SE
take-off-angles	TOA
transmission electron microscopy	TEM
trimethylaluminum	TMA
trimethylsilyl chloride	TMSCl
ultra-high vacuum	UHV
x-ray photoelectron spectroscopy	XPS

Chapter 1. **Introduction**

Atomic layer deposition (ALD) of cadmium telluride (CdTe) is a novel deposition technique that could be essential for surface passivation of next-generation mercury cadmium telluride ($Hg_{1-x}Cd_xTe$; MCT) semiconductor devices and sensors. Some requirements for effective surface passivation of MCT devices are conformal deposition, low temperature during deposition, and control of crystallinity, which the ALD process detailed here satisfies. Also, ALD offers a novel deposition technique complementary to the established CdTe deposition techniques of molecular beam epitaxy (MBE), evaporation and metal-organic chemical vapor deposition (MOCVD). ALD CdTe is capable as a conformal deposition technique where these other deposition techniques fall short. CdTe is the ideal passivation material for MCT devices, due to compatibility of material parameters between CdTe and MCT. Table 1.1 lists the values of lattice constants, bandgap, and coefficient of thermal expansion (CTE) for CdTe and $Hg_{0.75}Cd_{0.25}Te$ at 80 K and 300 K. CdTe is transparent to infrared (IR) light (bandgap ~1.6 eV) to act as a window material allowing transmission of IR into the sensor. The wide bandgap of CdTe, as compared to MCT, is essential for effective surface passivation. The CTE matching between CdTe and MCT is important for the optimal functioning of MCT sensors, which must be cooled from 300 K to operate nominally at 80 K without causing excessive strain between the two materials.

Table 1.1. Composition (x-value) and temperature dependence of CdTe and MCT parameters of lattice parameter,[1] bandgap,[2] and CTE.[3]

	x-value	Temperature (K)	Lattice Constant (Å)	Bandgap (eV)	CTE (10^{-6} K^{-1})
CdTe	1	80	6.474	1.607	4.364
		300	6.482	1.490	5.090
$Hg_{0.75}Cd_{0.25}Te$	0.25	80	6.459	0.164	4.388
		300	6.467	0.341	5.180

1.1. Surface Passivation of Single-Crystal Semiconductors

In semiconductor devices in general, the surface limits the performance by presenting an abrupt termination of the crystal lattice. The bulk-like termination of the crystal at the surface can be energetically unstable and the surface energy spontaneously minimizes, resulting in dangling chemical bonds and surface reconstructions of the crystal.[4] In the bulk of the crystal, away from the surface, periodicity of the crystal structure is maintained, but at the surface a different structure and symmetry is introduced. This fundamentally different crystal structure on the surface alters the electrical transport of the device, typically to the detriment of the device function, through the introduction of energy states (bonding/anti-bonding orbitals) in the electronic band structure of the material.[5] A generalized example of the energy states created by the abrupt termination of the semiconductor surface can be seen in Figure 1.1.

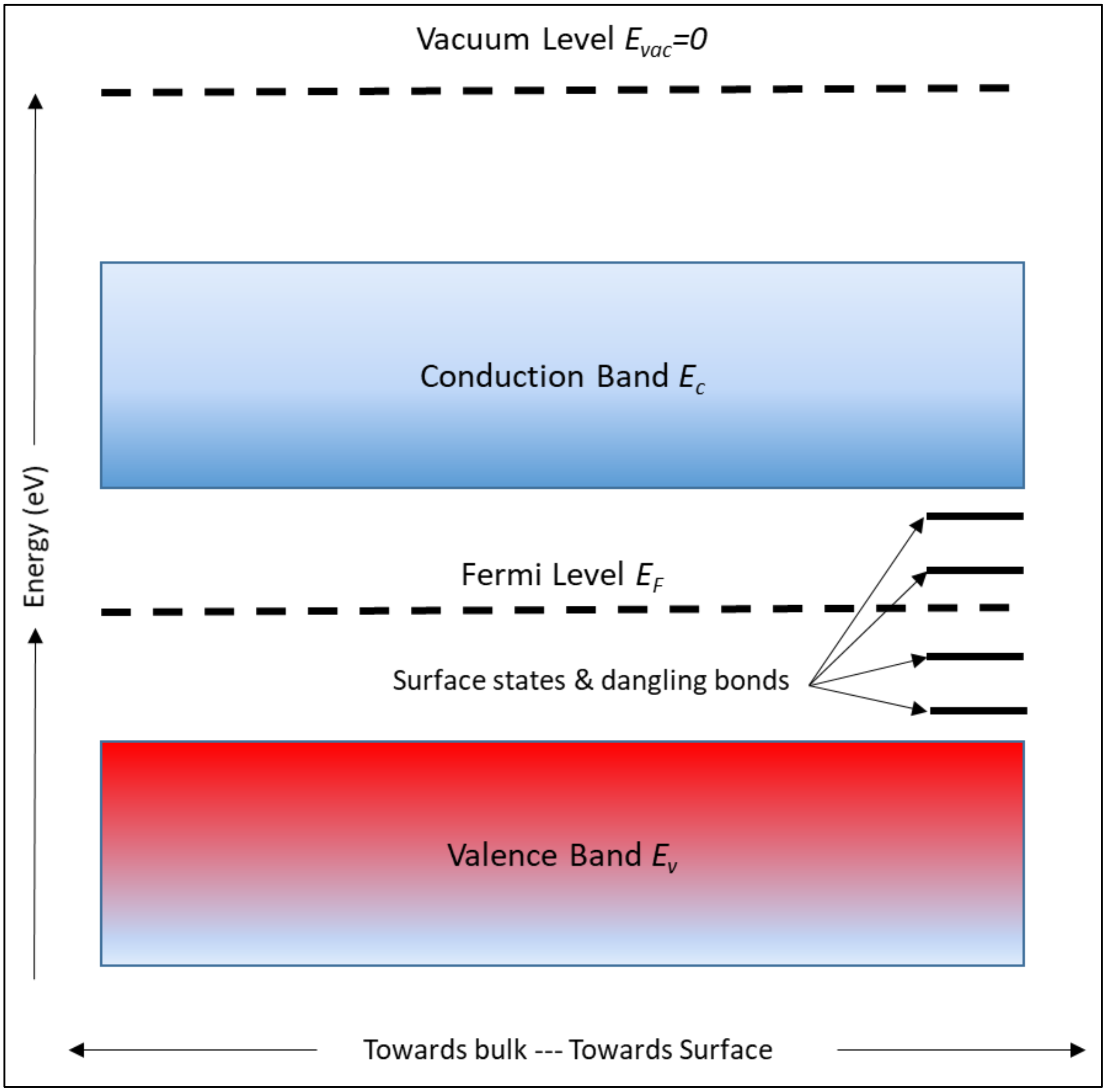

Figure 1.1. Generalized energy band diagram of a semi-infinite semiconductor showing energy levels of surface states and dangling bonds formed by abrupt termination of the crystal lattice by the surface.

The energy states present sites for recombination of charge carriers and also can bend the energy bands of the semiconductor. In MCT, the band bending can be on the order of the band gap itself, leading to shunting pathways for charge carriers at or near the surface.[6-9] Also, the surface is subject to contamination due to impurities and oxide formation, which also alters the electronic structure of the material to the detriment of device performance. The process of terminating the crystal surface with another semiconductor or insulator is known as *surface passivation*;[6,10] this mitigates the effect of surface states. The significance of using CdTe, a wider bandgap semiconductor, to passivate MCT, a narrow bandgap semiconductor, is that a heterojunction is formed, where the valence band (VB) and conduction band (CB) offsets between the narrow and wide gap semiconductors creates a barrier to both minority and majority carriers at the interface. A general energy diagram of passivation is seen in **Error! Reference source not found.**.

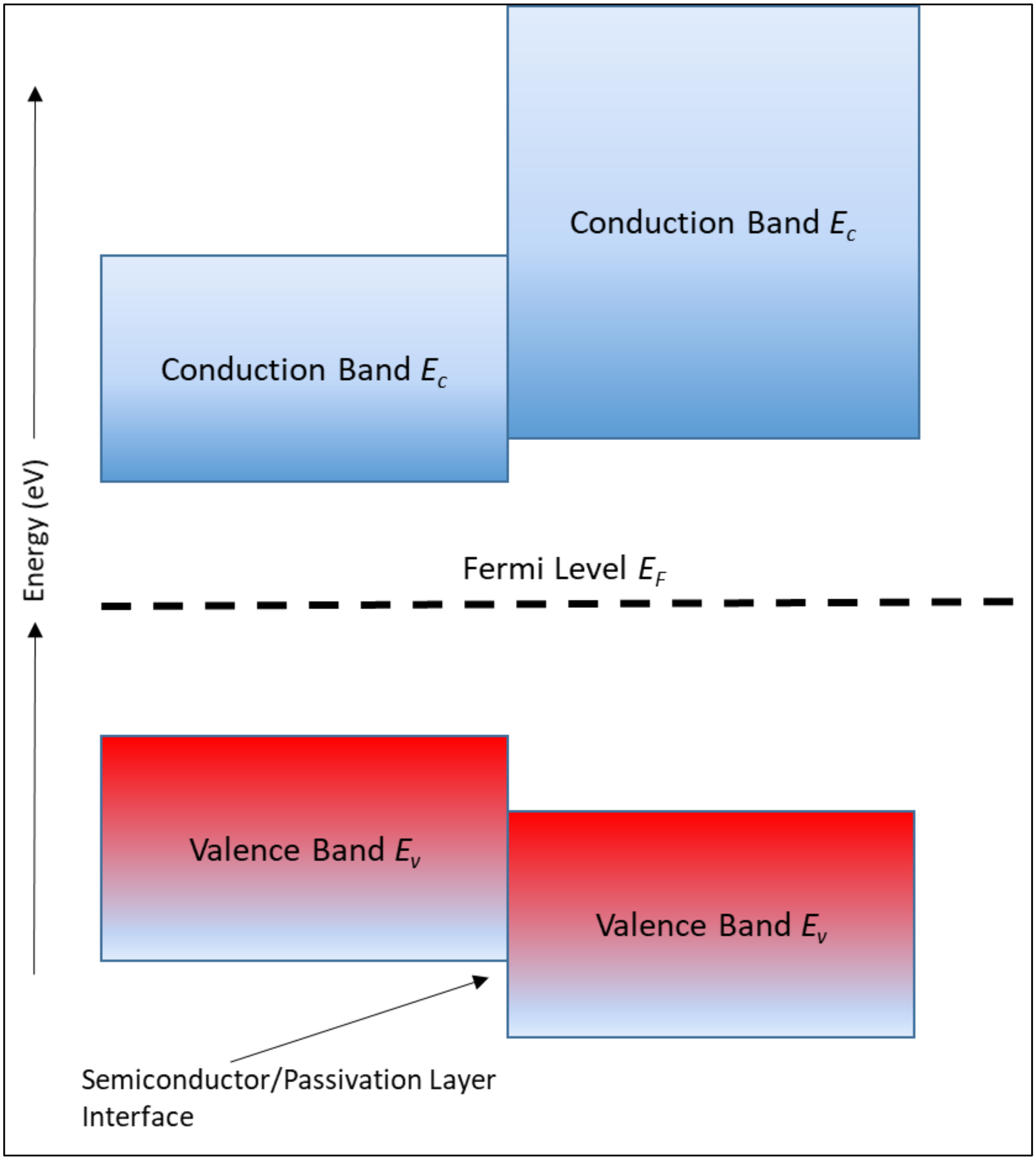

Figure 1.2. Passivation of semiconductor (left) surface states and dangling bonds through epitaxy of wider bandgap passivation layer (right) creating VB and CB offsets which are barriers to minority and majority carriers reaching the surface.

Passivation by epitaxy or deposition onto the crystal surface becomes increasingly critical to device performance of increasingly smaller devices, because the surface area to bulk volume ratio grows and non-ideal surface passivation contributions increase with decreasing pixel size. Passivation quality is dependent on material quality. Thus, characterization of the passivation material and process is required. This work lays out the details for the development of novel passivation processes for MCT devices and the material characterizations required to study the effectiveness of the passivation.

1.2. MCT Detector Technology Background

In order to provide context for this work concerning CdTe ALD, background on MCT devices is provided. MCT is an important single-crystal semiconductor material used for detection of IR light. MCT has a direct transition bandgap and has a very high absorption coefficient, which is tunable and engineered through growing material of varying x-value (Cd composition). As an alloy of $(HgTe)_{1-x}$, a semimetal with Eg ~-0.3 eV, and $(CdTe)_x$ a semiconductor with Eg ~1.5 eV, alloy bandgaps are nearly linear versus composition, spanning from the visible spectrum out into the far infrared. Alloys from x=0 (HgTe) to 1 (CdTe) vary in lattice constant by only 0.3% over this entire composition range.[11] These intrinsic characteristics make MCT the most important electronic material for fabricating IR detectors that can be tuned to various wavelengths.

Photodiodes fabricated from MCT are used in military and commercial IR detectors having specific performance requirements such as resolution, operating temperature, and spectral bandwidth.[12] An important approach to improving the resolution and performance of MCT detectors is to reduce the size and increase the density of individual photodiodes that make up detector arrays.

Commercially available MCT detectors have performance that is limited by intrinsic material properties (Auger recombination lifetime and/or radiative recombination lifetime of charge carriers; described below). However, next generation devices that are currently under research and development have moved towards smaller devices which have surface limited performance.

Detection of IR light is an area of interest for military for target detection, identification, and surveillance. A two-dimensional array of IR detectors is known as a focal plane array (FPA), the sensing components in IR cameras. An FPA is an array of photodiodes, which are p-n junctions that are reverse biased.[5,13,14] A diagram of a pn-diode can be seen in Figure 1.3.

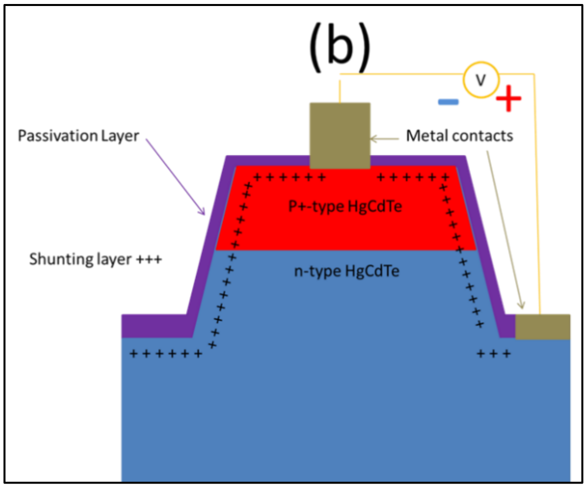

Figure 1.3. Cross-sectional schematic of a pn-junction fabricated from MCT. The CdTe passivation is deposited along the surface of the diode, including the pn-junction region.

Each photodiode constitutes one pixel that can detect photons that are at or above the bandgap of the absorbing material. The flux of these absorbed photons create electron-hole (eh)-pairs that drift under reverse bias, creating a photocurrent in the device, which is then read out by an external circuit, converted to a voltage and interpreted as the brightness of a particular pixel. Constructed together as an image, the electrical signal from an FPA enables imaging in short-wave IR (1-3 mm), mid-wave IR (3-5 mm), and long-wave IR (9-14 mm) spectra. These spectral bands are called the “atmospheric windows” where the gaseous molecules (e.g. H_2O, CO_2) that make up our atmosphere are transparent to infrared light. The next generation of detector technology is moving to larger epitaxial substrates and smaller device dimensions in order to increase the density of detectors within a single FPA and thereby increase image resolution, which extends the application space of the FPA.[15] A decrease in device dimension increases the surface area to bulk volume ratio of the device, and therefore the surface effects dominate over the bulk in smaller devices. This creates a number of non-trivial engineering challenges, one of which is electrical passivation of the surface of the detector material.[16] Passivation of the semiconductor surface occurs when an additional layer of semiconductor or insulator of greater band gap than the absorber is deposited onto that surface. The passivation layer satisfies dangling surface bonds and prevents recombination sites. Passivation also prevents further detrimental oxidation of the surface. The passivation layer should have a similar lattice constant to the underlying semiconductor in order to prevent strain precipitated dislocations, and contain a minimum of trapped ions within the material itself and at the interface between MCT and the passivation layer. For the MCT material system, CdTe passivation by MBE is the incumbent technology. However, as discussed below, this deposition method falls short for the requirements of next generation MCT devices.

The operating temperature of the FPA is governed by the spectral band of the detector. In the mid-wave (MW) and long-wave (LW), cryogenic temperatures (<80 K) are needed to suppress the thermal generation of charge carriers because MCT is a narrow bandgap material and even room temperature conditions create high densities of eh-pairs, and any additional IR photons that make up the signal are drowned out by noise. Diodes in reverse bias have parasitic currents, known as dark currents, which are present even without illumination of the diode.[17] Several important contributions to dark currents are diffusion current, generation-recombination (GR) current in the bulk, GR on the surface, and shunt current. Diffusion currents are the result of operating the diode in reverse bias, where minority carriers are injected by the electrodes, and can be suppressed by operation at low temperature. GR currents result from the thermal generation and recombination of carriers in the depletion region or at the surface of the diode at GR centers. E-h pairs created from illumination of the diode can also undergo recombination at GR centers. These GR centers are defect related states in the gap that are introduced by non-optimized growth and processing or insufficient surface passivation, and therefore can be suppressed by optimized growth, processing, and surface passivation (Figure 1.4a). Shunt currents result from a low-resistance, high charge density surface layer created through the trapping of charges by the passivation layer or by accumulation or inversion of the carrier type. As the low-resistance pathway is in parallel with the diode, any current flowing through the PN junction would shunt through the surface, increasing the dark current. The trapped charge density can be reduced through maintaining a pristine pre-passivation surface. Shunt currents are suppressed through effective surface passivation (Figure 1.4b).

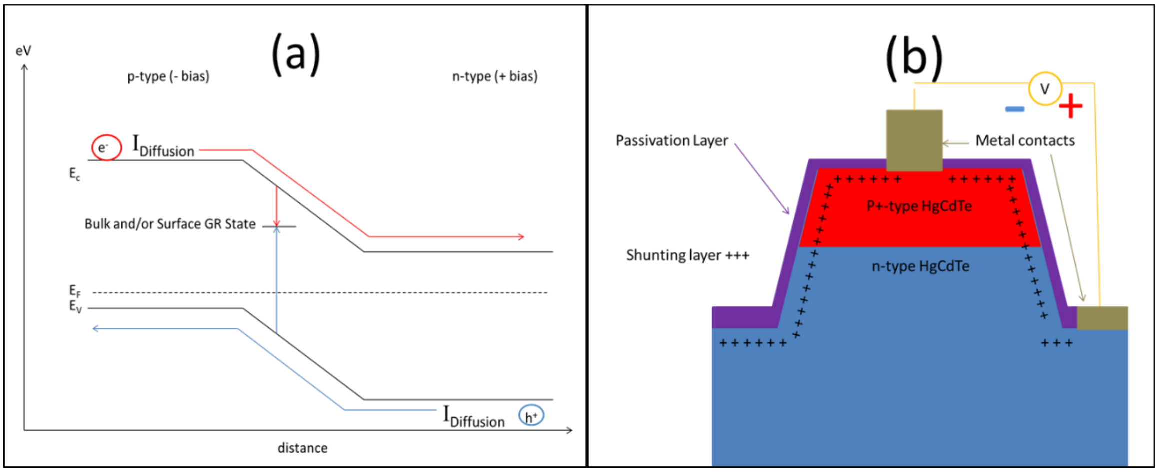

Figure 1.4. (a) Energy band diagram of MCT diode in reverse bias, illustrating the diffusion dark currents and the GR (defect state) dark current. (b) Cartoon of MCT photodiode in reverse bias. Trapped charges are represented by the + symbol, indicating a low resistance shunting path.

The overall performance of MCT devices is an intricate interplay between bulk and surface crystal quality, processing conditions, operating temperature, spectral band, image background and the resulting diode characteristics. As most of these parameters are optimized and near-ideal in current off-the-shelve IR cameras, the surface passivation presents a unique challenge for further optimization of the MCT device.

1.3. Statement of Problem I – Hg vacancy formation

The Hg-Te bond in MCT is much weaker than the Cd-Te bond and vulnerable to the temperature required for each processing step from growth through fabrication of detectors, which is one motivation for attempting to develop a low temperature ALD process: to avoid outgassing mercury (Hg), which degrades detector performance by creating Hg-vacancies. These vacancies act as GR centers, locations where any eh-pair created by photon absorption can then recombine, which is called Shockley-Read-Hall (SRH) recombination.[18,19] The other two important recombination mechanisms in MCT devices are Auger recombination and radiative recombination (discussed in Chapter 3) which are intrinsic to the semiconductor material and depend on temperature, alloy fraction, and doping level. Auger recombination is when a hole in the valence band and an electron in the conduction band recombine, and the excess energy is transferred to an electron in the conduction band, raising its energy. Auger recombination is described as a three-body interaction, because one hole and two electrons are required to participate. Radiative recombination occurs when an electron in the conduction band and a hole in the valence band recombine, and emit a photon with energy equal to the band-gap of the semiconductor. Low processing temperature of CdTe ALD is essential to suppress SRH recombination due to Hg vacancies.

1.4. Statement of Problem II – Decreasing Pixel Size

As the size of the individual photodiode decreases in newer generations of FPA technology, the diode's operation becomes increasingly dominated by contributions from the crystal surface. For optoelectronic materials, the surface generally presents a region for recombination of free carriers at a rate different from the bulk. If this rate of carrier recombination is higher than the bulk recombination rate, a device fabricated from this crystal will have surface limited performance, rather than an intrinsically limited bulk performance. The semiconductor surface must be passivated in order to suppress the influence of the surface on carrier recombination in optoelectronic devices. State-of-the-art passivation of MCT surfaces is accomplished by MBE of CdTe onto the clean MCT surface. Characterization of the effect of passivation is typically done by measuring recombination rates of the unpassivated surface versus the passivated surface (see Chapter 7).

Decreasing pixel size presents a challenge to MBE passivation of MCT. As MBE is a line-of-sight deposition technology, increasingly higher aspect ratios are progressively more difficult to passivate by MBE. To provide an example of the directionality of MBE of CdTe onto MCT, trenches were fabricated into MCT by inductively coupled plasma etching, followed by MBE deposition of CdTe. While the deposition appears conformal on the top and sidewall of the structures, voids were found in the v-shaped trenches when examined with scanning electron microscopy (

Figure 1.5). Voids present pathways for dark current to shunt across the surface, increasing SRH recombination at the surface. Therefore, a more conformal deposition technique such as ALD is desired.

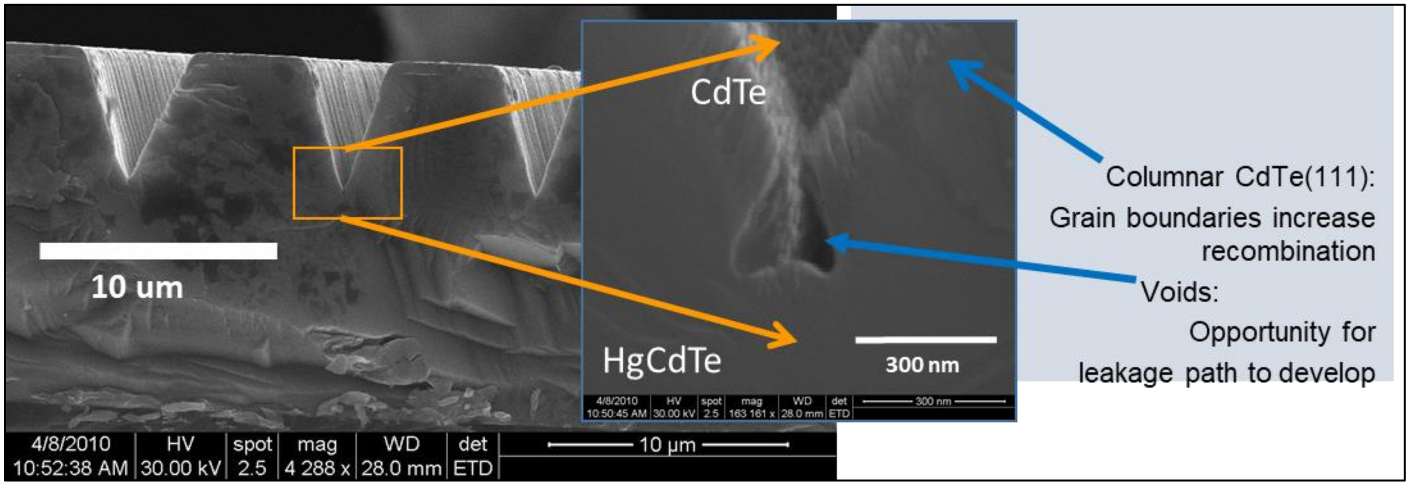

Columnar CdTe(111):
Grain boundaries increase recombination

Voids:
Opportunity for leakage path to develop

Figure 1.5. SEM image of void formation from the line-of-sight-fashion of MBE deposition.

1.5. Goals and Outline of Thesis

The goals of this dissertation are to demonstrate low-temperature conformal ALD of CdTe for the passivation of MCT and also to further the understanding of CdTe crystal growth in ALD.

- Chapter 2. Literature Review and Background of CdTe Growth by Chemical Deposition
    - Contains a literature review of CdTe growth by MOCVD and ALD and a discussion of the chemistries found throughout the thesis.
- Chapter 3. Experimental Procedures in the ALD Reactor and Characterization Techniques of the ALD
    - Describes the experiments and conditions used to grow CdTe in the ALD reactor and the characterization techniques used to optimize growth conditions and understand ALD film microstructure, chemistry, and electrical performance.
- Chapter 4. Argon Plasma Enabled Low Temperature ALD of CdTe
    - Describes the experiment and characterization that demonstrate CdTe ALD at low temperature, with the use of argon plasma metastable species, a novel approach to promote reactivity of ALD precursors without the use of high temperature.
- Chapter 5. Plasma Enabled Atomic Layer Deposition of CdTe from Bis(trimethylsilyl)telluride and Dimethylcadmium
    - Describes the experiment and characterization of temperature dependent CdTe ALD from the precursors bis(trimethylsilyl)telluride

    and dimethylcadmium, in an effort to substitute a new precursor for Te that is less hazardous than diethyltellurium.

- Chapter 6. Promoting Increased Growth-Per-Cycle in CdTe ALD by Solution-Phase Based Techniques
  - Describes increasing the growth-per-cycle of CdTe ALD process by introduction of Acetyl Bromide as a co-reactant.
  - Describes attempts at thermal CdTe ALD through precursor molecular design.
  - Provides evidence from in-situ spectroscopic ellipsometry for thermal growth of CdTe by introducing dichloromethane as the vapor-phase equivalent of a solvent based on liquid-phase, solution-based chemistry as a path towards thermal ALD of CdTe at 75 °C.
- Chapter 7. Minority Carrier Lifetime of HgCdTe Passivated by CdTe ALD
  - Describes passivation of MCT substrates using the Acetyl Bromide technique
  - Reports the results of temperature dependent photoconductive decay (PCD) measurements of unpassivated MCT substrates versus CdTe ALD passivated MCT substrates to model the recombination rates and extract the SRH parameters, which demonstrates effective passivation.
  - Reports the results of PCD measurements at 77 K of a series of samples, which demonstrates effective passivation

- Chapter 8. Conclusions and Future Work
    - The novel contributions and results are summarized here and the directions of future work are outlined.

Chapter 2. Literature Review and Background of CdTe Growth by Chemical Deposition

ALD is a unique thin film deposition technique. Thin films can be deposited using physical vapor deposition (PVD) techniques such as MBE, thermal evaporation, sputtering, or chemical vapor deposition (CVD) techniques such as MOCVD and ALD. In PVD, the source materials are physically transported to the substrate surface and absorb there to form the thin film. In CVD, the source materials (precursors) are carried into a flow of gas (carrier gas) to the substrate surface, where the precursors undergo a chemical reaction to form the thin film and chemical reaction by-products. The term “precursor” indicates that these source materials are the reactants to a chemical reaction and the thin film and by-products are the products of the chemical reaction. ALD as defined below is a subset of CVD and is compared and contrasted to CVD in the next sections. In CVD the precursors are injected into the carrier gas and arrive at the substrate surface in a continuous manner, and the substrate surface temperature is such that the chemical reactions are promoted at the surface and not in the gas-phase. The gas phase reactions are undesirable, since precursors reacting in the gas-phase can lead to particle nucleation and subsequent contamination of the growth surface. CVD techniques can deposit onto the substrate surface in a conformal fashion due to the vapor-phase nature of the precursors, whereas in some PVD techniques (i.e., MBE) the source materials deposit in a non-conformal, line-of-sight fashion.

Attempts at ALD of CdTe have leaned heavily on past work in MOCVD of CdTe, which is reviewed here to provide background on the chemistry that occurs during MOCVD. Past work in CdTe MOCVD (and the small number of published reports on CdTe ALD) occur at temperatures too high for passivation of MCT, where Hg outgassing occurs.[3]

2.1. ALD Definition and Example

Given the requirements for passivation stated in Chapter 1, ALD shows promise for deposition of passivation layers on MCT. ALD is a unique variation on thin-film chemical vapor deposition (CVD), first introduced by Suntola, et al.[20] for large area, thin film ZnS for display applications. Instead of flowing all the precursors simultaneously, in ALD each precursor is injected, or pulsed, separately. These precursor pulses are separated by a purge step; after each precursor pulse is stopped, the growth chamber is purged with carrier gas to remove excess precursor off of the surface and exhausted through the vacuum system. Thus, ALD has the advantage of completely separating the precursors temporally and spatially, which avoids any opportunity for gas-phase reactions. Because the precursors are separately pulsed, ultra-reactive precursors can be used to promote growth, whereas in CVD this would lead to gas-phase precursor reaction and nucleation leading to particle contamination of the growth surface. Additionally, ALD is "self-limited": the deposition occurs during each injection event, where precursor molecules irreversibly chemisorb onto available surface sites, resulting in layer-by-layer growth due to the self-limited nature of precursor chemisorption. The substrate is exposed to each precursor gas individually, where the substrate surface becomes saturated with up to a monolayer of precursor molecules, followed by purging of the reaction vessel with inert gas, leaving a saturated surface but no vapor phase precursor available to react. The term "self-limited" refers to the fact that up to one monolayer (and no more than one monolayer) can chemisorb on the substrate surface. The self-limited nature results from the molecular structure of the precursor, where the central atom (e.g. cadmium [Cd]) is bound with ligands (chemical functional groups, e.g. methyl groups [-CH_3]) to form the precursor molecule (dimethylcadmium [DMCd] see

Figure 2.1).

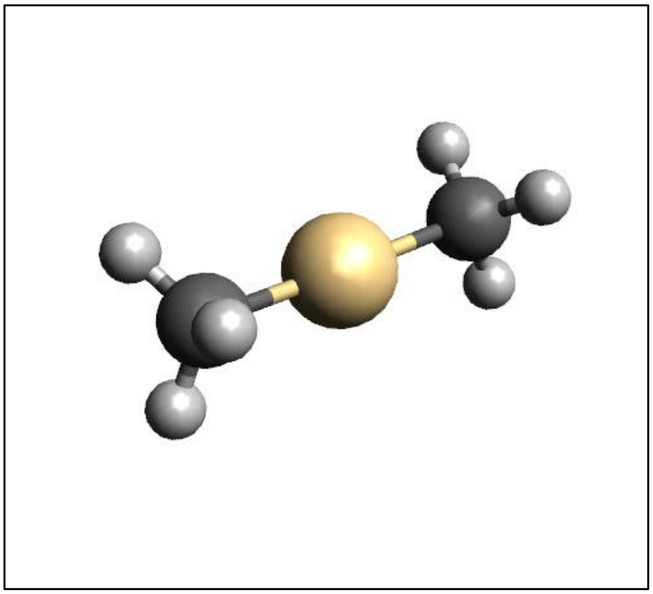

Figure 2.1. Model of dimethylcadmium: central Cd atom (gold), bonded to two methyl groups, which consist of a carbon (black), and three hydrogen (grey) atoms. Drawn using Avogadro.[21]

The ligands are not reactive towards each other but are reactive towards the surface. When the precursor chemisorbs on the surface, the ligands can either re-configure around the central atom, dissociate from the central atom, or react with surface sites. At least one ligand remains attached to the central atom and this limits any additional precursor from chemisorbing. Then a second precursor gas is introduced, and surface reactions take place, followed by an additional purge cycle. This is repeated for a number of cycles to achieve the desired thickness. Each half-cycle results in a terminal surface functional group, where no additional precursor can be chemisorbed.

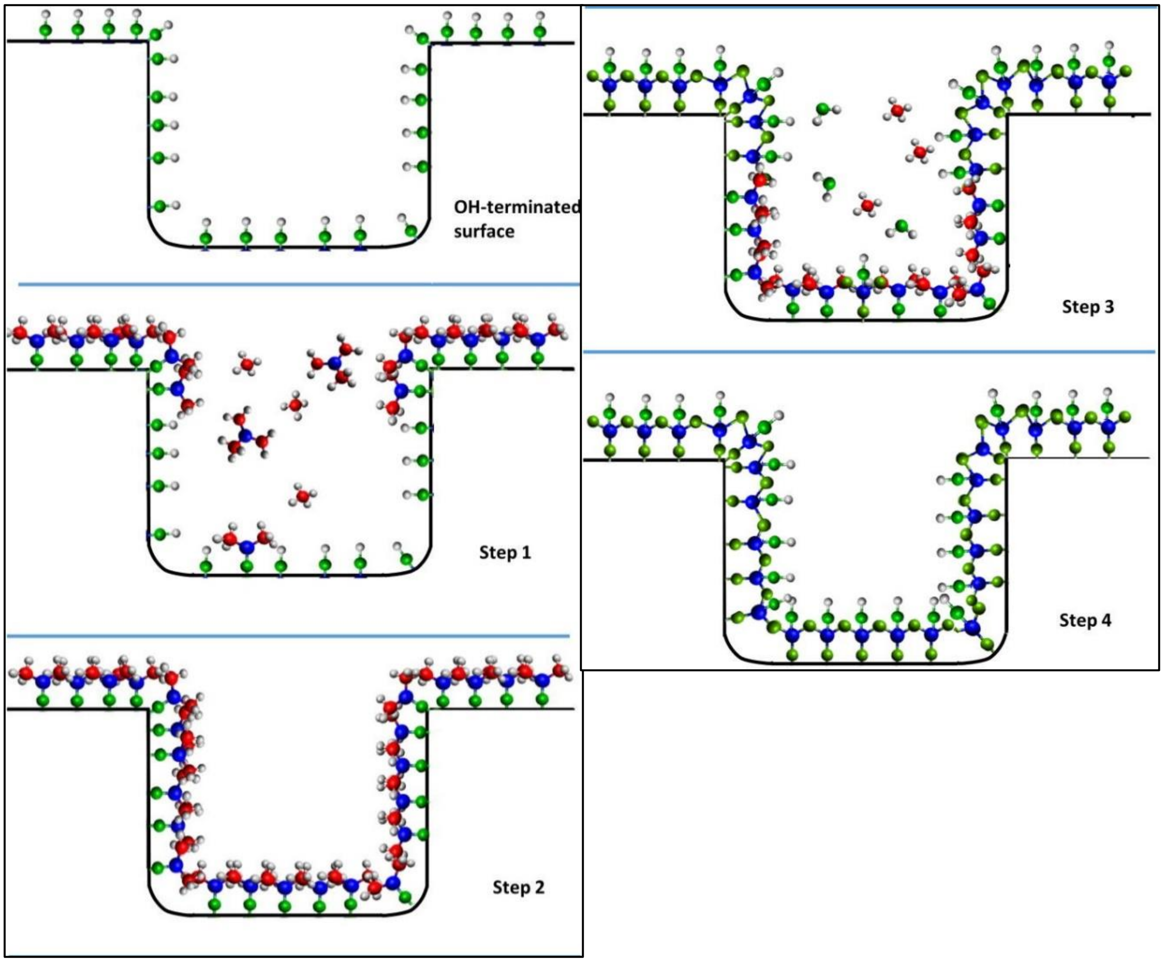

Figure 2.2. ALD of Al_2O_3 from TMA and H_2O, illustrating the self-limited nature of each precursor pulse.[22] The starting surface is OH-terminated and the steps are 1) pulsing TMA results in Al-CH_3 or Al-$(CH_3)_2$ terminated surface and excess TMA molecules, 2) purging excess TMA from reactor, 3) pulsing H_2O reacts with surface to produce OH sites and methane along with excess water molecules, and 4) purging reactants and excess water returns the surface to starting conditions, completing one ALD cycle.

2.1.1. Thermal versus Plasma Assisted ALD

For an example of ALD, in the case of ALD of Al_2O_3 on silicon, **Error! Reference source not found.** shows a schematic of the process for forming the ALD layer from trimethylaluminum (TMA) and water as precursors. The first step is introduction of TMA in to the reaction chamber, with an inert carrier gas such as nitrogen or argon. The TMA is highly reactive and pyrophoric in ambient conditions with water vapor. Under low vacuum of the ALD environment, TMA reacts with surface hydroxyl groups, eliminating methane in the process. The surface is now terminated with methyl groups, which will not react with any additional TMA, thus preventing more than one monolayer to chemisorb. Then, the chamber is purged with inert carrier gas, removing any unreacted precursor in the gas phase, and leaving a surface that is inert towards additional TMA vapor. After purging TMA, water vapor is pulsed into the chamber. The water reacts with the surface methyl groups, eliminates methane, and regenerates a surface site (hydroxyl group). After an additional purge, the surface is returned to TMA active hydroxyl terminated state, ready for additional reaction with TMA. This completes one cycle of ALD. This is an example of “thermal ALD”, where the available thermal energy is sufficient to allow for co-reactivity between precursor and surface site enables film deposition.

Thermal ALD is contrasted to plasma-assisted ALD, or PA-ALD where the use of a plasma step is necessary for growth. When discussing any form of CdTe ALD, for brevity the term ALD will be used even where PA-ALD is more exact. As will be demonstrated in the ALD of CdTe, plasma is required to create a surface that is co-reactive towards tellurium precursors, but at a low enough temperature to avoid outgassing of Hg. ALD has the advantage of being highly conformal due to the vapor phase precursors, with deposition over a range of challenging microstructures. In addition, ALD can be performed at low temperatures, which is required for deposition on temperature sensitive MCT substrates. With the proper choice of precursor chemistries, deposition should be possible over a range of temperatures. Also, the use of a plasma can activate surface-chemisorbed precursors, as described below.

2.2. Cadmium Telluride ALD

Deposition of CdTe onto MCT by ALD has previously been demonstrated only at higher temperatures.[23] The motivation for this work is to find a lower process temperature in order to effectively passivate MCT surfaces without damaging temperature effects on the MCT. Previous work on MOCVD and ALD of CdTe is reviewed here, in order to identify the rate limiting step of thermal ALD, and propose a hypothesis on how to overcome it. The hypothesis is tested in this thesis.

A common thread between MOCVD and ALD can be found in the precursor chemistries. In both regimes, precursors should be volatile so that under the optimized deposition conditions, gaseous molecules of organometallic precursors present in the deposition chamber completely saturate the surface sites on the substrate. In one set of experiments in this work, DMCd and diethyltellurium (DETe) were chosen because of their off-the-shelf availability, established growth by MOCVD,[24-28] sufficient vapor pressure and relative stability. Also, the self-limited chemisorption of both, which is necessary in ALD, was previously demonstrated.[23] In general, shorter-chain alkyl ligand(s) on the metal atom such as DMCd and DETe results in more volatile and more reactive precursors, and these two precursors are available commercially as electronic grade chemicals with good shelf-life. Both MOCVD and ALD of CdTe using DMCd and DETe have been shown to occur only at temperatures >200 °C[23-25,28-30] indicating that DMCd and DETe are not co-reactive below this temperature. However, previous work in MOCVD demonstrated that deposition occurs mainly through pyrolysis of the surface adsorbed DMCd into cadmium metal sites.[25] These sites, in turn, can catalyze decomposition of DET. Creating Cd metal surface sites at high temperature would be detrimental to MCT. But, plasma has been shown to decompose surface adsorbed precursors in a number of ALD processes, rather than elevated temperature: deposition of platinum through decomposition of surface adsorbed platinum precursors by oxygen plasma,[31] growth of ruthenium films through reduction by ammonia plasma,[32] and even activation of hydrogen-passivated silicon surface sites by remote argon plasma exposure,[33] which in the absence of plasma requires thermal desorption at a high substrate temperature (~500 °C).[34] All of these examples occur at nominally (~100 °C) low temperatures. Therefore, the use of plasma was investigated to promote low temperature CdTe ALD. The main hypothesis of this entire work is that plasma can promote the decomposition of surface chemisorbed DMCd into Cd metal, which in turn catalytically decomposes tellurium precursors, forming CdTe thin film and volatile by-products.

Another tellurium precursor bis(trimethylsilyl)telluride (BTMSTe) was also investigated as a tellurium source. This precursor could be successfully substituted for DETe in the CdTe ALD process described above, but with a few caveats discussed in Chapter 7.

2.2.1. Surface chemistry of the deposition of single crystal CdTe thin films by CVD

CVD and ALD processes can be defined through their elementary chemical reactions[35] which are the most direct single-step reactions that take reactants to products, or in this case, precursor to film. In most cases, precursor to film involves more than one elementary reaction, and ALD by definition has at least two. In CVD the substrate temperature must be at a minimum temperature to promote film growth from the reactivity of the precursors, but not too high a temperature as to lead to unwanted side reactions, such as rough film growth rather than smooth film growth. Because the surface is hotter than the precursor gases, the surface provides enough thermal energy for the incoming molecules to decompose and/or react at the surface and only at the surface (not in the gas phase). The other requirement of CVD is that the volatile precursors themselves are not too reactive with each other as they mix in the gas phase inside the reactor, in order to avoid nucleation of particles on the surface, but reactive components only when adsorbed on the surface. Hence, volatile inorganics (such as HCl gas) and metalorganics (such as TMA) are used as sources because they provide enough flux of molecules out of the container and into the reactor to result in film growth. When all the requirements are met, the conditions are within the “process window” for film growth. During CVD, the substrate is exposed to both or all of the chemical sources at the same time, where the thermal decomposition and subsequent reaction of precursors occurs only on the substrate surface. The rate of reaction and hence deposition is dependent on the diffusion to and reaction at the substrate surface. This leads to a time-dependence of the film thickness, meaning that to achieve the desired thickness, the film is grown for a set time, and the growth rate in CVD is measured in thickness/time, e.g., nm/sec.

In ALD, the substrate is exposed to each source independently and sequentially. Each precursor pulse saturates the surface, and then the next incoming precursor pulse reacts with the surface adsorbed species to deposit material monolayer-by-monolayer. Since each sub-reaction occurs independently, the thickness is dependent on the number of precursor pulses, or cycles, rather than the product of reaction rate * time. Thickness can be controlled down to the individual sub-cycle elementary reaction. For example, the MOCVD of CdTe in general consists of exposing the surface to both DMCd and DETe at temperatures >200 °C. The reaction rate shows an Arrhenius dependence on substrate temperature above this minimum,[29,30] so the deposition rate is dependent on growth time and substrate temperature. However, during thermal ALD of CdTe,[23] in general, the substrate is exposed to DMCd, then the chamber is purged, then substrate is exposed to DETe, and one complete monolayer of CdTe results. Therefore, the total thickness of the CdTe layer is controlled by the number of cycles of DMCd pulse, purge, DETe pulse, and purge. This way, the exact number of monolayers is controlled by number of cycles, and it is not necessary to have precise control over the length of time it takes to deposit CdTe by MOCVD. When combined with a suitable in-situ characterization method, the elementary reactions are readily observed in ALD.

2.2.2. Empirical Model for the Chemical Reactions during ALD of CdTe

The MOCVD of CdTe has been observed to occur by the following reaction equations. The overall chemical reaction between DMCd and DETe can be described as:

$$(\mathrm{CH_3})_2\mathrm{Cd}_{(\mathrm{g})} + (\mathrm{CH_3CH_2})_2\mathrm{Te}_{(\mathrm{g})} \rightarrow \mathrm{CdTe}_{(\mathrm{s})} + 2\mathrm{C_3H_8}_{(\mathrm{g})} \qquad \textbf{2.1}$$

where one mole of DMCd reacts with one mole of DETe in the gas phase to produce one mole of solid CdTe and two moles of gaseous propane. However, the overall reaction can be broken down into the elementary reactions that better describe the reactions taking place on the growing film surface, where the surface atomic site is denoted by Sf:

$$\mathrm{Sf}_{(\mathrm{s})} + (\mathrm{CH_3})_2\mathrm{Cd}_{(\mathrm{g})} \rightarrow \mathrm{Sf\text{-}Cd(CH_3)}_{(\mathrm{s})} + {}^{\bullet}\mathrm{CH_3}_{(\mathrm{g})} \qquad \textbf{2.2}$$

$$\mathrm{Sf\text{-}Cd(CH_3)}_{(\mathrm{s})} \rightarrow \mathrm{Sf\text{-}Cd}_{(s)} + {}^{\bullet}\mathrm{CH_3}_{(\mathrm{g})} \qquad \textbf{2.3}$$

$$\mathrm{Sf\text{-}Sf\text{-}Cd}_{(s)} + (\mathrm{CH_3CH_2})_2\mathrm{Te}_{(\mathrm{g})} \rightarrow \mathrm{Sf\text{-}CdTe}_{(\mathrm{s})} + 2\,{}^{\bullet}\mathrm{CH_2CH_3}_{(\mathrm{g})} \qquad \textbf{2.4}$$

The bullet symbol $^{\bullet}$ indicates a radical, i.e., a methyl radical is a product of reactions *2.2* and *2.3*, and an ethyl radical in *2.4*.

2.2.3. Promoting surface chemistry through argon metastable exposures

In this work, the CdTe ALD is hypothesized to be accomplished through the same elementary reaction pathways, with the exception that the substrate temperature can now be lowered, and the decomposition of DMCd into Cd metal is not promoted through pyrolysis, but rather through exposure to argon plasma. Argon metastable species form in the remote inductively coupled plasma (ICP) source located upstream of the substrate surface.[36] Argon metastable species (Ar*) are defined as argon atoms that are in an excited energy state, where the valence electrons are at an elevated energy level compared with the ground state. Metastable species of Ar* have long lifetimes (~seconds) because they have forbidden electric dipole radiative transitions back to the ground state and, therefore, can transfer energy from their electronic states through collisions with the substrate surface.[37,38] Due to the laminar flow established in the ALD reactor, Ar* can be carried in the vapor phase to the substrate surface, and promote decomposition. Ar* is proposed to be the activating species that is capable of removing the methyl ligand from chemisorbed DMCd. Previous work has demonstrated that surfaces exposed to Ar* at low temperature can promote chemical reactions at the substrate surface that otherwise require high temperature such as: removing hydrogen passivation from silicon surfaces,[33] ALD of Silicon by alternating pulses of SiH_4 and then Ar* [39] or MOCVD of silicon using SiH_4 and Ar*.[38] At the nominal pressure of ~1 Torr (the same as the ALD reactor during deposition), the Ar* concentration is as high as 1.2 x 10^{11} cm^{-3},[40] which is comparable within an order of magnitude with standard ICP densities at lower pressures (~10^{12}).[41]

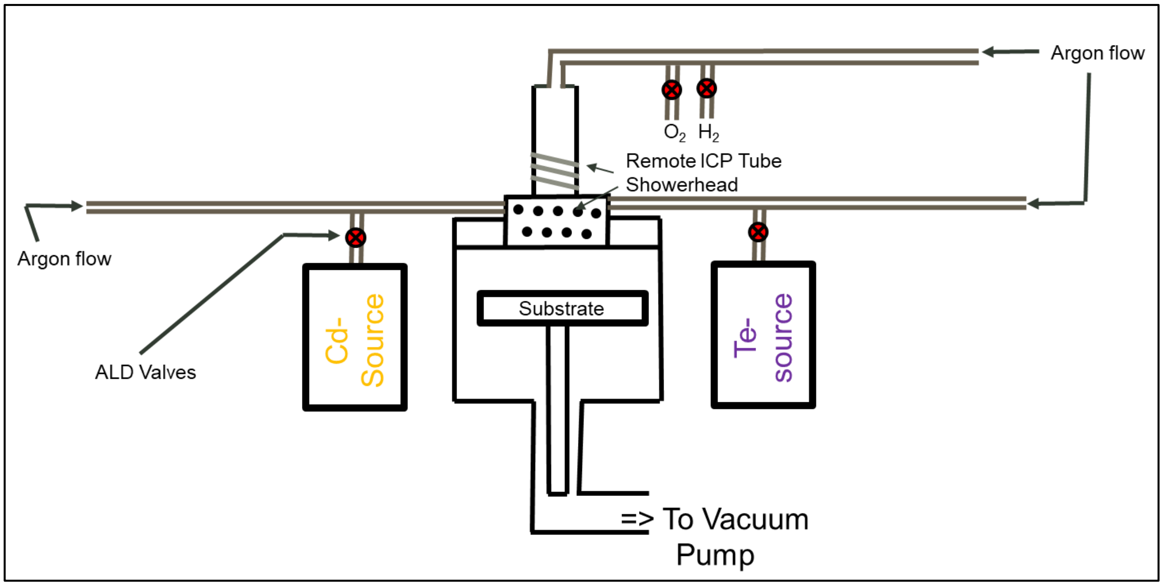

Figure 2.3. Schematic of flow through the ALD reactor. The remote ICP tube is located upstream of the substrate. During plasma exposure, Ar* promotes decomposition of DMCd on the substrate surface.

The ALD reactor (discussed in Chapter 3) uses argon as a carrier gas and has an inductively coupled plasma (ICP) tube located remotely and upstream of the substrate holder in the reactor (Figure 2.3), to allow testing of the hypothesis that generation and exposure to an argon plasma decomposes the chemisorbed DMCd species to the subsequent Cd atom. Competing reaction mechanisms on the surface during CdTe ALD are also present when using bis(trimethlsilyl)telluride (BTMSTe). In this case, the mechanisms are more complex than indicated by the simple mechanism presented above, and will be discussed in detail in Chapter 5.

2.2.4. Organometallic Chemistry of Cadmium and Tellurium Precursors

The molecular structure of the ALD precursors are important for understanding the- growth mechanisms. Figure 2.4 illustrates the precursors used in this work, along with their formal oxidation states, shown through proposed dissociation reactions. The oxidation state influences the ability or inability to undergo thermal ALD reactions because reactivity between molecules with central atoms of similar oxidation state is impeded due to similar reduction-oxidation potentials.[35,42]

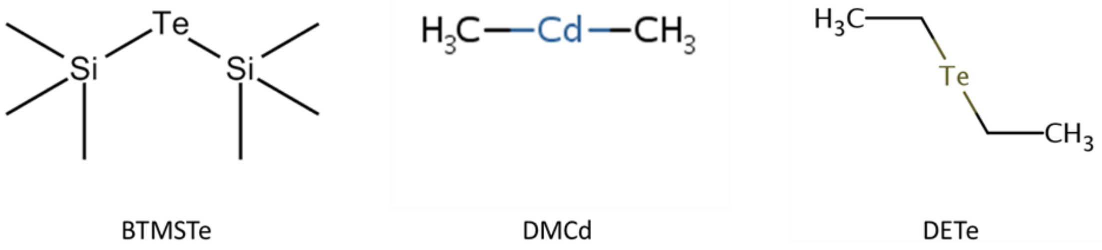

$$((CH_3)_3Si)_2Te \rightarrow 2(CH_3)_3Si^{2+} + Te^{2-}$$

$$(CH_3)_2Cd \rightarrow 2(CH_3)^{2-} + Cd^{2+}$$

$$(CH_3CH_2)_2Te \rightarrow 2(CH_3CH_2)^{2-} + Te^{2+}$$

Figure 2.4. Chemical structure of CdTe ALD precursors: bis(trimethylsilyl)tellurium, diethyltellurium and dimethylcadmium, along with their formal oxidation states illustrated through hypothetical dissociation reactions.

DMCd consists of a central cadmium atom bound to two methyl ligand groups. In general, metal-alkyl bonds lead to very high precursor volatility that decreases as the number of carbons in the alkyl ligand increase (i.e., volatility of methyl ligand > ethyl > propyl >butyl > …). For example, DMCd has a vapor pressure of 21 Torr at 20 °C while diethylcadmium has a vapor pressure of <1

Torr at 20 °C. Other alkyl-cadmiums besides DMCd are not commercially available. Asymmetric alkylcadmiums such as diisopropylethylcadmium are not stable and decompose into elemental cadmium and diisopropylbutane by-products upon exposure to light or room temperature. DMCd is extremely hazardous due to the combination of high vapor pressure and high toxicity. Inhalation must be avoided at all costs.

DMCd was used in the past to create carbon-carbon bonds in organic synthesis and has since been replaced with Grignard reagents, which are much safer. DMCd reacts with acetyl halides (e.g., acetyl bromide) to produce acetone and cadmium bromide as in equation 2.5:

$$\mathrm{(CH_3)_2Cd_{(l)} + 2CH_3COBr_{(l)} \rightarrow CdBr_{2(s)} + 2(CH_3)_2CO} \qquad \textbf{\textit{2.5}}$$

This chemistry is explored in Chapter 6 to promote higher growth-per-cycle.

Cadmium is a Group 12 transition metal. Transition metals have distinct reactivity derived from the order of which their electron d-orbitals are filled as we move across the periodic table. However, group 12 metals (Zn, Cd, Hg) have filled d-shells, and no oxidation states other than +1 or +2 are known. These states are formed by removing electrons from the 4s, 5s, and 6s shells for Zn, Cd, and Hg, respectively, rather than losing any of their d-shell electrons. The filled d-shell provides an energetically unfavorable (exceedingly stable) shell from which to remove electrons,[42,43] hence only the +1 and +2 oxidation states are found in Group 12 metalorganics. Since the bonding electrons come from the s-shell, the resulting molecules are linear. For deposition of CdS from DMCd and

H_2S gas on CdS itself, density functional theory simulations[44] have indicated that the energy barrier for the transition of a physisorbed linear DMCd molecule to a physisorbed bent metastable state is the rate limiting step for deposition using DMCd, and the molecule transitions to a chemisorbed state through the loss of a methyl ligand, resulting in a cadmium surface atom terminated with a methyl group pointing up in the growth direction, a monomethylcadmium (MMCd) molecule. There is some prior work using ultra-high vacuum (UHV) exposures of surfaces to DMCd and analysis by XPS that demonstrates the methyl ligand can chemisorb on the surface along with the MMCd molecule, and the entire DMCd can absorb molecularly as well.[45] In some specific cases, the entire molecule has been shown to absorb on the surface, terminating the surface with a dimethylcadmium group. Whether in this case the molecule is chemisorbed or physisorbed cannot be determined through XPS alone.

DETe consists of a central tellurium atom bound to two ethyl groups. Again, the volatility of alkyl tellurides follows the trend of the cadmium ligand series (i.e., volatility of methyl ligand > ethyl > i-propyl >t-butyl > …). The two ethyl groups are tetrahedrally coordinated to the central tellurium atom. The sp^3 hybridized orbitals of the tellurium are involved in the bonding, resulting in a bent molecule (Figure 2.4), just like the hydrogen atoms on the oxygen atom in water. The other two sp^3 orbitals are fully occupied, so the DETe molecule is an 18-electron system, with 16 coming from the Te and each ethyl ligand donating one electron.

Bis(trimethylsilyl)tellurium (BTMSTe) (Figure 2.4) geometry is similar to DETe, in that the silyl ligands are tetrahedrally coordinated to the central Te atom like the ethyl ligands in DETe. However, the formal oxidation state of the Te atom is -2 due to the high acidity of the silyl ligand, as opposed to the oxidation state of +2 for Te in DETe due to the electron donating, basic nature of the methyl anion. This precursor along with its selenium analog and bis(triethylsilyl) variants were reported by Pore, et al.[46] and tested in room temperature liquid solutions as potential ALD co-reactants against a host of inorganic and organic metal compounds. Metal halides were shown to be very reactive to the BTMSTe family of compounds. However, metal alkyls which have methyl ligands show little or no reactivity to BTMSTe. This could be due to the alkyl ligands on the silyl group, which are chemically identical (i.e., unreactive) to the alkyl groups on metal alkyls. An article reported using a hybrid ALD/CVD deposition process to deposit germanium antimony telluride (GST) on various metal and insulating substrates.[46] The germanium compounds and antimony compounds were deposited using layer-by-layer ALD sub-cycles, but the BTMSTe precursor wasn't active as a tellurium source unless exposed to a hydrogen containing plasma during pulsing of this chemical, leading to a non-self-limited CVD behavior, where the amount of material deposited during the sub-cycle could be greater than one monolayer, depending on the pulse time. Additionally, the authors claimed that if they first exposed the starting substrate surface (native oxide of silicon; SiO_2) to BTMSTe, this actually stopped any further growth beyond the initial chemisorption of BTMSTe, suggesting that the BTMSTe molecule can render the surface inert towards further growth. This phenomenon of stopping further growth after initial chemisorption of silyl-ligand containing precursors was observed by Bent et al. and was used for selective area epitaxy by ALD. The trimethylsilyl ligand is also present in a commonly encountered photolithography chemical hexamethyldisilazane (HMDS) used as an adhesion promoter for photoresists. HMDS is also known as bis(trimethylsilyl)amine. Calling it by that name highlights the chemical similarity to BTMSTe, where the nitrogen atom has been substituted by a tellurium atom. Hydrophobic photoresists have difficulty adhering to the native oxide surface of silicon, so HMDS is used as a surfactant molecule. Exposing silicon native oxide to HMDS vapor (by placing a wafer surface upside down over a beaker containing hot HMDS, for example) allows the hydrophobic nitrogen atom to bond to the polar surface oxides, then terminating the surface with hydrophobic, non-polar methylsilyl groups.

The Gwon group discovered a thermal ALD process using methanol, which they claimed to react with the BTMSTe in-situ to generate H_2Te, with methoxy-trimethyl silane as the volatile by-product.[47,48] Using solution-based chemistries, Stuczynski et al. at Bell Labs studied the reaction of DMCd with bis(isopropyldimethylsilyl)telluride (BIPDMSTe), an analogue of BTMSTe, where one methyl group on the silyl ligand is replaced by an iso-propyl group.[49] The selenium analogue of BTMSTe was also studied. Stuczynski et al. discovered that mixing DMCd and BIPDMSTe (and other silylchalcogenide analogues) together resulted in no reaction. However, immediately upon injection of polar solvent into the system, CdTe precipitated out of solution. “Dealkylsilation” is the noun they used to describe the exchange of the silyl ligand of the Te molecule with the methyl group on DMCd, resulting in synthesis of CdTe. The solvents studied were dichloromethane, trichloroethane, toluene, and saturated hydrocarbons (e.g., octane, decane). The use of dichloromethane produced CdSe precipitate from the DMCd, BTMSSe solution instantaneously at room temperature, while the less polar solvents had a longer reaction half-life. Using toluene as the solvent resulted in a half-life of days, while the saturated hydrocarbons as solvent resulted in a half-life of a week. This indicates that the polar nature of the solvent enhances the kinetics of the reactions. Perhaps this is the mechanism behind the use of methanol by Gwon et al.[48] and explains their need to inject methanol during each precursor pulse, not only the BTMSTe, which they claim reacts with methanol. Saturating the atmosphere of their chamber with methanol would allow for residual methanol physisorption on the substrate surface, where methanol would act as a solvent to mimic solution-based chemistry in the vapor-phase system of the ALD reactor.

Stuczynski et al.[49] even explicitly suggest using this scheme in the vapor phase, and hence thermal ALD was attempted and discussed in Chapter 6.

Combination of all the above conditions and caveats using DMCd, plasma, and BTMSTe or DETe, has led to the developed PA-ALD process used in this work. In general, the process is: initiated growth by exposure(s) to DMCd first, purging the DMCd, then argon plasma decomposition of this surface, followed by purging, then exposure to pulses of Te-precursor, followed by purging. The process is then repeated for the desired number of cycles/thickness, enabling a PA-ALD of CdTe at arbitrary temperature with a growth rate between 0.3 and 0.6 Å/cycle.

The previous work in MOCVD of CdTe has demonstrated that the deposition occurs by pyrolysis of surface-adsorbed DMCd, followed by catalytic decomposition of tellurium precursors into CdTe and by-products.[25] The use of argon plasma to decompose the DMCd rather than pyrolysis is explored in this work in an attempt to enable low temperature CdTe ALD. Additionally, thermal ALD of CdTe was explored briefly.

Chapter 3. Experimental Procedures in the ALD Reactor and Characterization Techniques of the ALD

Deposition of CdTe by ALD was explored in the ALD reactor. In-situ characterization during growth in the reactor was provided by a spectroscopic ellipsometer (SE) which monitored growth in real time and enabled development of deposition parameters both within a single experiment and from experiment to experiment. Ex-situ x-ray photoelectron spectroscopy (XPS) was used to confirm the presence of CdTe, stoichiometry and also to examine the presence of contaminants other than Cd and Te (i.e., C, Si, O, and Br). Transmission electron microscopy (TEM) was used to image cross-sections of the ALD films grown on both Si/SiO_2 and MCT, identifying the films as CdTe through lattice fringe spacing measurements and indexing to the crystal directions of CdTe. Atomic Force Microscopy (AFM) was used to generate amplitude and phase maps of the ALD film topography to reveal growth mechanisms. Photoconductive decay measurements (PCD) of the minority carrier recombination rates in both ALD passivated and unpassivated samples characterized the passivation quality of the CdTe ALD, confirming that CdTe ALD passivated surfaces have higher lifetime compared to unpassivated surfaces.

3.1. The ALD Reactor

The deposition chamber in which this work was carried out was a continuous flow ALD-150LX reactor built by Kurt J. Lesker Company (KJLC) (see Figure 3.1) located at the US Army Research Laboratory (ARL) in Adelphi, MD. The reactor is designed so that a sample can be placed on a 6” diameter platen directly into a continuous laminar vertical flow of gas. The operating pressure is ~ 1 Torr, which ensures the gas flow in the reactor is in the viscous flow regime, rather than molecular flow found in ultra-high vacuum (UHV) chambers. During deposition argon carrier gas is streamed from the top of the reactor through the plasma port to the bottom of the reactor at the exhaust port, where the gas is pumped out through a vacuum foreline to a process pump. Additionally, there are four precursor inlet lines allowing for physically separated points of injection of precursor into the carrier gas. Argon continuously flows through the four precursor lines during deposition. The lines insert into a showerhead that is designed to disperse the precursor uniformly into the carrier gas stream and to focus the precursor into the center of the viscous flow so that the precursor molecules are hitting the sample surface with an optimal distribution compared to simply injecting the precursor through the top of the plasma port. Additionally, there is a curtain gas dispersion plate that allows for argon flow down the sides of the reactor. Curtain gas flow rates can be controlled separately from either the plasma carrier gas flow or the precursor carrier gas flow. The curtain gas aids in focusing the precursor injection onto the substrate surface and also helps to suppress deposition onto the sidewalls or the analytical port windows. This effectively eliminates the need to clean the windows, and allows for continuous monitoring of the substrate surface by SE throughout many depositions without altering the optical signal from deposition on the windows.

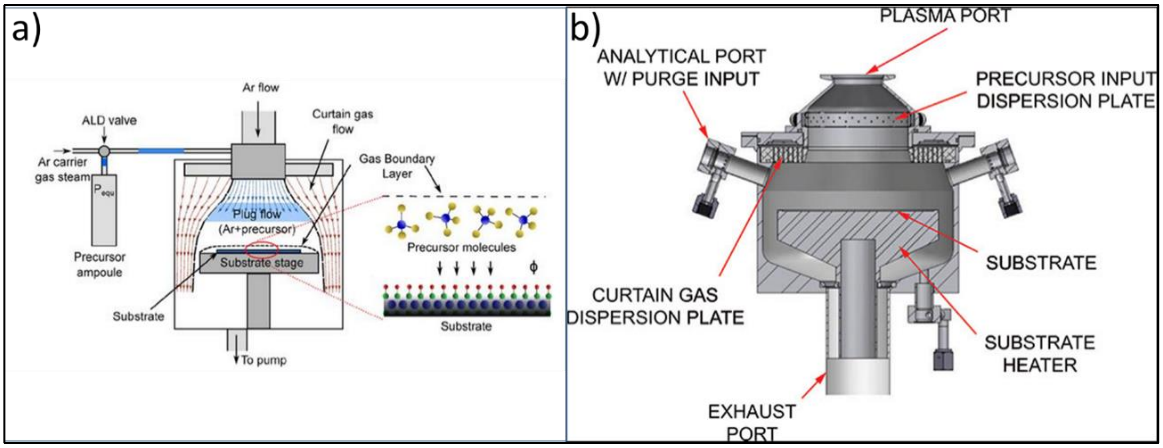

Figure 3.1. Cross-sectional view of the ALD reactor. a) Cartoon illustrating the laminar flow within the reactor at an operating pressure of 1 Torr. b) View of the precursor input, plasma port, and analytical ports.[50]

3.1.1. Plasma Source

An ICP source is mounted on top at the plasma port. This source consists of a sapphire tube with a three-turn coil wrapped around the bottom half. The coil is coupled to a radio frequency (RF) power source with an automatic matching circuit that allows for up to 1000 W of power to be applied to the coil and network at a frequency of 13.56 MHz. The automatic matching network (“automatch”) allows for minimizing the reflection of the RF power back to the coil, and maximizes the power applied to the plasma. Due to the spiral shape of the coil, as the current through the coil moves in one direction, a magnetic field is induced according to the Lorentz Right-Hand Rule, in the direction perpendicular to the current. When the current changes direction, the electric and magnetic fields do too. This entire switching of currents and fields occurs at the frequency of the RF voltage supply, at 13.56 million times per second. As gas flows through the ICP tube, the power from the ICP coil transfers to and excites the gas, creating populations of ions, metastable species, neutrals, and ground-state molecules or atoms. These species in turn travel to and collide with the substrate surface, where they then undergo reactions with surface adsorbed molecules or films. The ICP source is used to promote growth at lower temperatures where the thermal energy from the substrate temperature alone is insufficient to promote spontaneous ALD reactions.

3.1.2. Analytical Ports

The ALD Chamber has two optical ports on opposite sides of the cylindrical chamber where the SE source and detector are mounted, situated at 70° angle of incidence (AOI) to the growth substrate. The source lamp and the detector are mounted so as to lie within the plane of incidence.

3.1.3. Experimental Conditions

The process pressure of the chamber during process development was 1 Torr monitored by a capacitance monometer. The plasma gas feed chemistries studied were pure argon gas and a variety of H_2/Ar gas mixtures. The substrates were introduced into the process reactor through a gate valve coupled to a load lock, which reaches a base pressure of 10^{-6} Torr or better before introduction into the reactor. The pressure inside the load lock is then raised to ~50 mTorr higher than the reactor using argon purge gas, and only then is the gate valve opened. This enables the introduction of the substrates to the chamber under a positive pressure into the reactor to ensure any hazardous chemistries within the reactor are continually purged through the reactor vacuum manifold and not into the load lock. A robotic load arm was used to carry the wafers into the reactor and loaded onto the heated substrate by lift pins. This procedure is interlocked into the opening of the gate valve, and would abort if the pressure differential is not achieved, and designed by the ALD reactor manufacturer.

3.2. Spectroscopic Ellipsometry

Spectroscopic ellipsometry is a characterization technique that can measure the optical constants of thin films by measuring a change in the (elliptical) polarization of light that has reflected from or transmitted through those films. By constructing a model of the index of refraction (n) and extinction coefficient (k) of each layer in a stack of thin films, the measured data can be fitted against the model, and refinement of the model until the data fits well enables extraction of n and k of each layer in the stack.[51] By using a spectrum of wavelengths to characterize the film as opposed to a single wavelength, the model can be overdetermined: the number of equations is (much) greater than the number of unknown parameters, and the dispersion of n and k versus wavelength can be measured. This powerful technique enables the in-situ characterization of the growing ALD film in order to extract the growth per cycle, thickness, and dielectric function. SE in general involves an inversion problem of taking measured parameters Psi and Delta and inverting them into the complex dielectric function, and comparing with the modeled dielectric function. The measurement of Psi and Delta can be both precise and accurate, but inversion into thickness and dielectric function can be model dependent. By minimizing the error in the fit data to be measured, both the dielectric function and thickness of several layers in a stack within a model can be fitted well to the measured data.

The technique can measure the change in polarization rather than simply reflectivity and, although optical in nature, exceeds the diffraction limit and can measure the thickness and dielectric function of even sub-monolayer thick films.

In general, the SE experiment consists of: light of known polarization amplitude and angle is reflected off the sample surface, collected and the polarization amplitude and angle measured. Measurement can be done when the sample is mounted in the ALD reactor chamber (in-situ SE) and during growth as a function of time (dynamic in-situ SE).

The mounted in-situ SE is a JA Woollam M2000[52] which has a source mounted on one of the analytical ports and a detector mounted opposite to the source on the other analytical port, as shown in

Figure 3.2. The source consists of a tungsten lamp and rotating polarizer. Source light of a known polarization is reflected from the growing surface and collected at the detector, which consists of a multiplexed silicon photodetector array, collecting and analyzing many channels simultaneously, which enables data collection as a function of time. The data collection interval can be as short as 50 milliseconds, allowing for dynamic in-situ characterization of ALD growth and the structure of the surface. SE is sensitive not only to the film properties, but also extremely sensitive to the conditions of the surface, down the single-atom thickness and monolayer termination of the surface and is compatible with ambient pressure and low vacuum conditions, unlike other single-atom-thickness sensitive methods such as reflection high-energy electron diffraction (RHEED) and low-energy electron diffraction (LEED), which use electrons as the probe beam. The electron-source techniques are incompatible with the operating

pressure of the reactor during deposition (1 Torr), as the mean free path of the electron is negligible at these pressures.

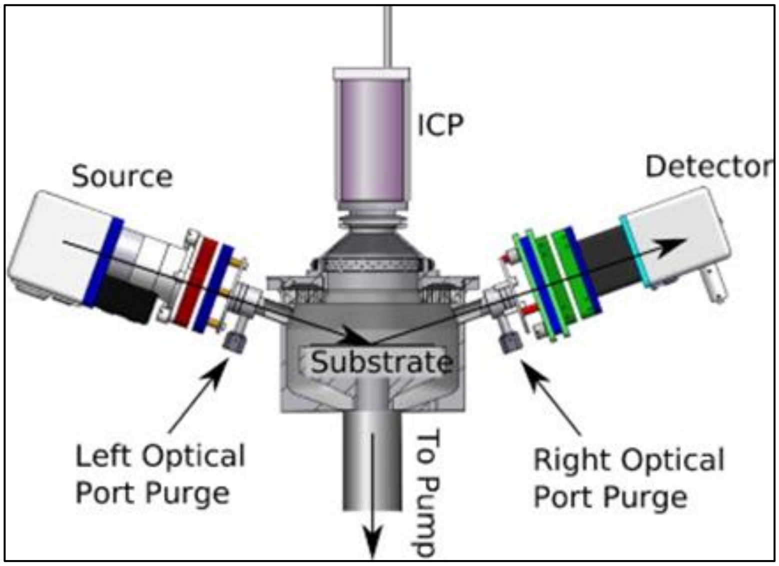

Figure 3.2. Cross-sectional view of the ALD reactor. The SE hardware consists of a light source of well-known polarization which reflects off of the substrate surface and is collected at the detector. The angle of incidence and reflection are ~70° from the surface normal.

Light is a transverse electromagnetic wave that consists of a traveling and oscillating electric field and a magnetic field that is perpendicular to the electric field (E-field) (see **Error! Reference source not found.**.3 and **Error! Reference source not found.**). The fields can remain in a single plane, or rotate along the axis of the direction of travel, defined here as the z-direction. The wave has an E-field amplitude and a phase. Two light waves travelling along the same z-axis can have their phases aligned in phase, be 90° to each other out of phase, or somewhere in between. When the phases are aligned, meaning the crests and troughs of the two waves happen at the same point in space and time, the light has linear polarization, and we can define the direction and magnitude of the resulting polarization. This linearly polarized light now has the electric field oscillating in a single plane. When the two waves are completely out of phase, meaning the crests of one wave happen at the troughs of the other, we call this circularly polarized light. This circular polarization of light now has the E-field rotating about the direction of travel as a function of space and time. Any phase in between these two extremes results in elliptically polarized light. Unpolarized light has E-fields pointing equally in random orthogonal directions as a function of space and time. Examples of sources of unpolarized light include sunlight, incandescent bulbs, and flame. When unpolarized sources such as these reflect off of specular surfaces at a certain angle, the reflected light is polarized at the same certain angle. Examples of polarized light include viewing sunshine reflected off of a lake, or off asphalt in the distance where the reflected light has large intensity of polarization parallel to the plane of the reflecting surface. The incident ray of light and the reflected ray of light lie within the plane of incidence.

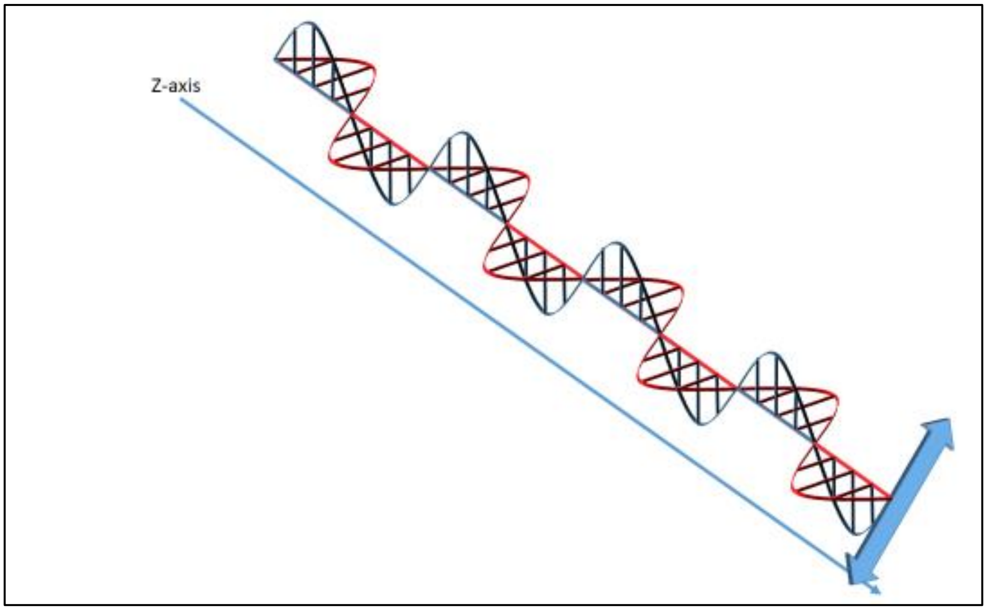

Figure 3.3. Two light waves with their E-fields aligned 0° out of phase. One wave has E-field along the x-axis and the other along y. The blue arrow indicates projection of the resulting E-field amplitude onto the xy-plane.

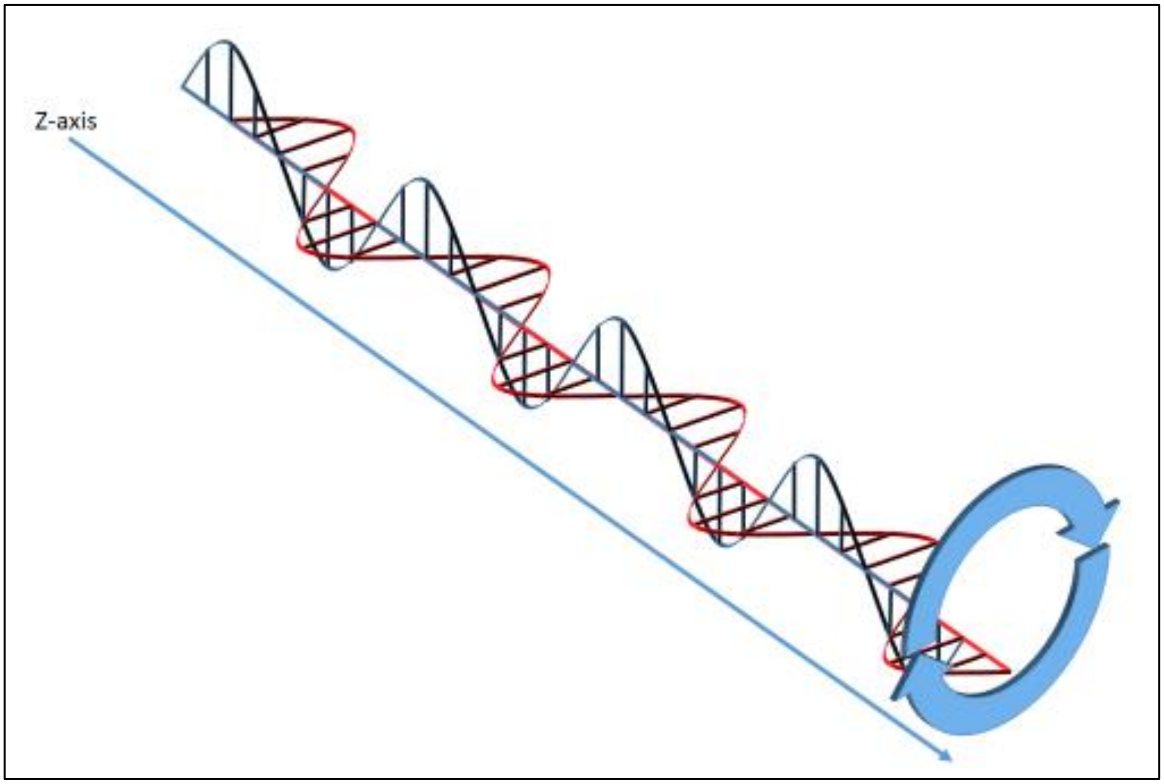

Figure 3.4. Two light waves with their E-fields completely out of phase (90° out of phase). The blue circle indicates the projection of E-field amplitude on the xy-plane with circular polarization.

When light of a known polarization is reflected off of a single film or stack of films, the polarization of the reflected beam is changed by the film stack. The SE can measure the complex reflection ratio **ρ** of the incident and reflected beams, which have a real-valued amplitude and phase of the reflected beam's electric field. The fundamental equation of SE is:

$$\rho = \tan\Psi\, e^{i\Delta} \qquad \textbf{\textit{3.1}}$$

The amplitude ratio **Ψ** and phase difference **Δ** between the incident beam R_i and the reflected beam R_r can be calculated. Defining E_p and E_s as the complex-valued electric fields of the light, E_p is parallel to the plane of incidence, and E_s is orthogonal to the plane of incidence. Controlling the linear polarization state of the incident beam, and measuring the elliptical polarization of the reflected beam, the ratio of parallel parts of the incident and reflected beams can be calculated, and similarly with the perpendicular parts of the incident and reflected beams to calculate the complex reflection coefficients R_p and R_s:

$$R_p = \frac{E_{ip}}{E_{rp}} = \frac{A_{rp}}{A_{ip}} exp\left(i(\delta_{rp} - \delta_{ip})\right) \tag{3.2}$$

$$R_s = \frac{E_{is}}{E_{rs}} = \frac{A_{rs}}{A_{is}} exp\left(i(\delta_{rs} - \delta_{is})\right) \tag{3.3}$$

where ip, rp, is, and rs are the incident (i) and reflected (r) beams parallel (p) and orthogonal (s) to the plane of incidence, A is the amplitude and delta is the phase angle of the beam. Then **ρ** can be equated:

$$\rho = \frac{R_p}{R_s} \tag{3.4}$$

Therefore:

$$\tan\Psi\, e^{i\Delta} = \frac{\frac{A_{rp}}{A_{ip}} exp\left(i(\delta_{rp} - \delta_{ip})\right)}{\frac{A_{rs}}{A_{is}} exp\left(i(\delta_{rs} - \delta_{is})\right)} \tag{3.5}$$

And therefore tan(**Ψ**) is the amplitude ratio and **Δ** is the phase difference of incident and reflected beams. The SE measures two ellipsometry parameters, **Ψ** and **Δ**, at each wavelength. In a multilayered stack of film, such as a CdTe layer on top of a SiO_2 layer on top of Si, each layer has a complex reflection ratio ρ (equation **Error! Reference source not found.**) that is dependent on t hickness and dielectric function, which is the square of the complex index of refraction N (**Error! Reference source not found.**)**Error! Reference source not found.**:

$$N = n - ik \quad \textbf{3.6}$$

where n is the index of refraction and k is the extinction coefficient.

The complex reflection ratios and coefficients can now be restated in terms of the complex index of refraction as a function of the angle of incidence and wavelength of light. Using Fresnel's equations of reflection gives expressions for a multilayered stack of materials in terms of complex reflection R_s and R_p for a stack of films from ambient (layer 0) through the last stack (layer m):

$$R_{s,p}^{0,1,2,\dots,m} = \frac{r_{s,p}^{0,1} + R_{s,p}^{0,1,2,\dots,m} exp(-i2\varphi_i)}{1 + r_{s,p}^{0,1} R_{s,p}^{0,1,2,\dots,m} exp(-i2\varphi_i)} \quad \textbf{3.7}$$

where φ_i is the difference in phase induced to the beam when travelling through the ith layer from top to bottom of stack, where i is the layer from 0 to mth. The phase difference is dependent on film thickness of the ith layer d_i, wavelength of incident light lambda, θ_i angle of incidence going from ith to (i+1)th according to Snell's law and N^i the complex index of the ith layer as defined above:

$$\varphi_i = 2\pi\left(\frac{d_i}{\lambda}\right) N_i \cos\theta_i \quad \textbf{3.8}$$

Snell's law is:

$$N_i \sin\theta_i = N_{i+1} \sin\theta_{i+1} \quad \textbf{3.9}$$

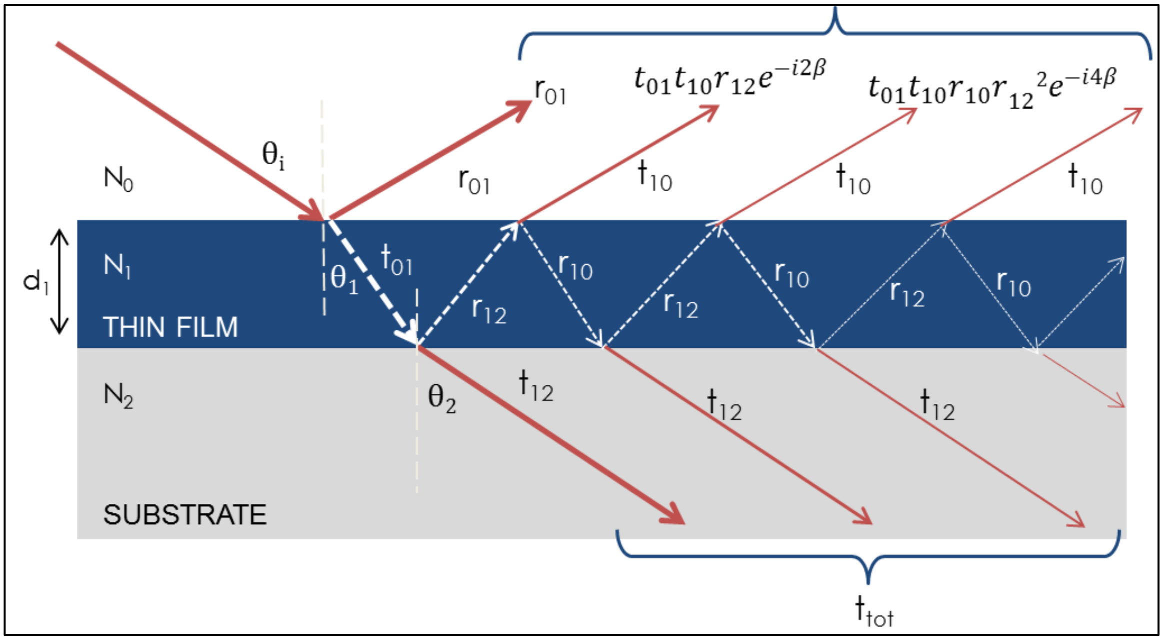

Figure 3.5. Reflection (r) and transmission (t) of light from a film (blue) on top of a substrate (gray), showing the angle-dependent Snell's law dependency of θ and N used in the stack model of equation *3.7*.[52]

The derivation above highlights how the ellipsometry parameters are measured exactly, and how they must be inverted numerically using a stack model to come to the final index of refraction and thickness for each layer in a stack. The procedure for modelling the sample surface by in-situ SE consists of measuring the starting substrate surface before growth, fixing some starting variables, then initiating growth and continued measurement of thickness as the film grows, ceasing growth, measuring the static film to minimize error, then re-fitting of the dynamic data to minimize error in fit across the time-dependent growth data. The SE software (CompleteEase) provides a number of built-in complex refraction index dispersion models and the Cauchy model[51] was used to fit the thickness and index of the CdTe ALD layers. The Cauchy model is an empirical equation for the index of refraction n of the materials in the stack as a function of three independent variables to fit to derive thickness:

$$\mathrm{N}(\lambda) = \frac{\mathrm{A}}{\lambda} + \frac{\mathrm{B}}{\lambda^2} + \frac{\mathrm{C}}{\lambda^4} \qquad \textbf{\textit{3.10}}$$

The software aids in finding the best fit to the A, B, and C parameters to derive the index of refraction and invert the above SE equations to find a value for thickness of each film but cannot be found for the substrate. The light beam becomes incoherent travelling through the thick substrate and loses polarization sensitivity, because the substrate is much thicker than the coherence length of the beam. The nominal thickness values were checked against other characterization techniques to ensure the validity. This provided a robust quantitative technique for observation of the film during growth. While the precision and accuracy in the modelled thickness and index can be dependent on the model, in-situ SE is invaluable for rapidly optimizing the ALD parameters. Also the SE can be used as a qualitative measure of change in optical constants. The raw data values of **Ψ** and **Δ** alone can indicate that a change in optical properties (e.g., thickness and index) is underway, and also when a film's optical constants have reached steady state (e.g., the growth has ended).

A growth model for all experiments carried out in this dissertation was created using CompleteEase software that controls the SE hardware, and models the optical constants and thickness of the growing surface, substrates, and interfaces. The model can calculate a thickness value and the optical constants of each layer. The raw ellipsometry parameters Δ and Ψ can be observed as a function of time. A Cauchy model was used to model the ALD layer on to of a built-in Si substrate model (including the native oxide). This then allows the thickness of the ALD layer versus time to be observed during process development.

3.3. X-ray Photoelectron Spectroscopy

XPS is a powerful surface characterization technique that enables analysis of the chemical composition and oxidation states of atoms contained within ~10 nm of the surface. This is accomplished by illuminating the surface of the sample in a UHV chamber with monochromatic x-rays (photons), which, if the x-ray energy is sufficient will ionize the atoms in the surface and eject photoelectrons (PE), which have a spectrum of kinetic energies (KE). The ejection of photoelectrons from the surface of a material by photons of sufficient energy is known as the Photoelectric Effect. UHV conditions are necessary to collect PE scattered by the sample; higher pressure interferes by further scattering of the electrons from gas molecules. The PE are collected into an energy analyzer to count the number of PE vs. their KE. The x-rays travel deeply into the material, scattering electrons from both the bulk and the surface (~10s of nm). The PE scattered from the bulk have a high probability of undergoing scattering events, and lose their initial KE through inelastic scattering events. PE coming from the surface have a very low scattering probability, and most of these surface PE scatter inelastically. The elastically scattered PE create the signal peaks observed in the XPS spectrum, while the inelastically scattered PE contribute to the background (see Figure 3.6). Careful calibration of the whole XPS analysis system (source energy, detector work function) allows the KE to be converted into binding energy (BE), and thus able to count PE vs BE. Since the exciting x-rays are monochromatic, or of nominally unique energy, the calculated BE is nominally unique to the core electrons of each element on the periodic table, and each core electron has a characteristic BE shift away from the nominal BE based on the oxidation state. A general schematic for the XPS experimental set-up, including concepts discussed here is found in Figure 3.6.

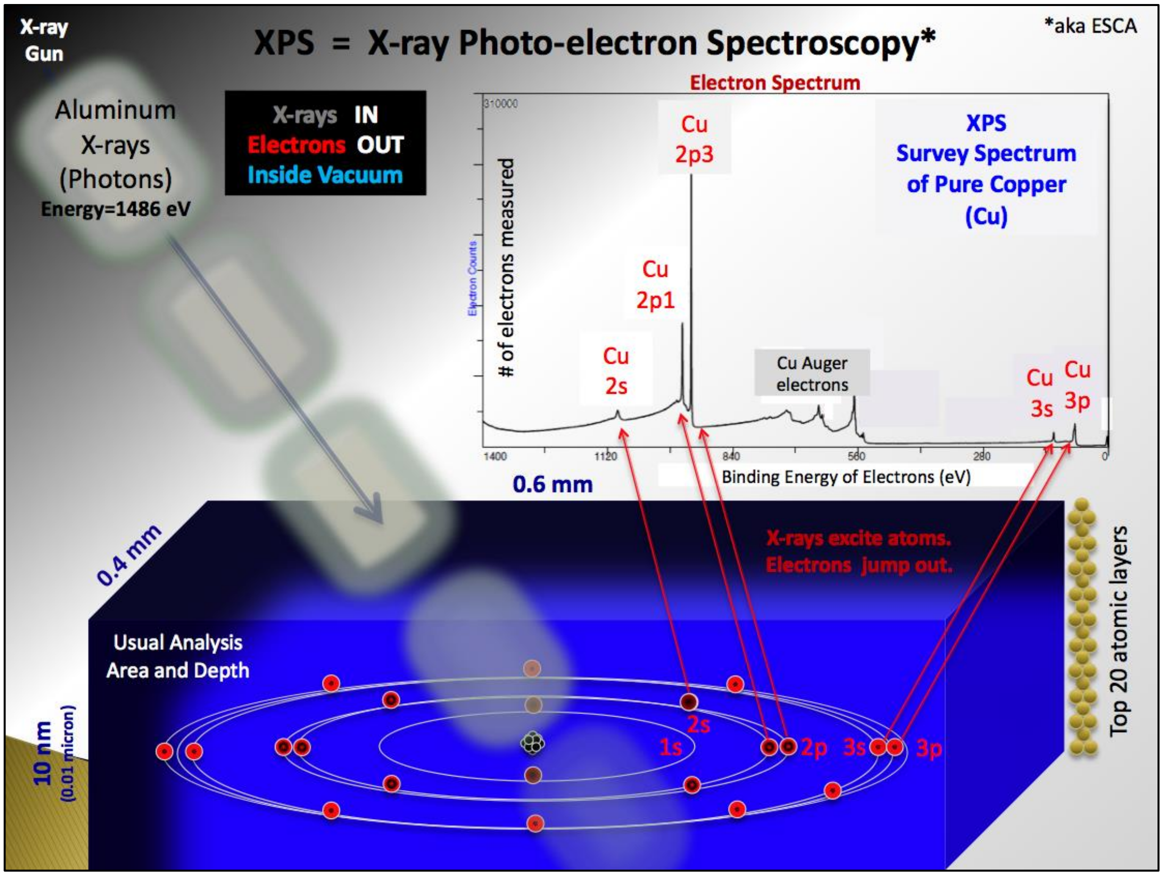

Figure 3.6. The physics of XPS illustrating the x-ray induced ejection of photoelectrons, or the photoelectric effect. Image courtesy of Wikipedia Public Domain Images.

The PE ejected from the sample have KE according to:

$$\mathrm{KE} = \mathrm{h\nu} - \mathrm{BE} - \varphi \qquad \textbf{\textit{3.11}}$$

where $h\nu$ is the x-ray source energy and φ is the work function of the detector. Thus the binding energy can be calculated if source energy and detector work function are known:

$$\mathrm{BE} = \mathrm{h\nu} - \mathrm{KE} - \varphi \qquad \textbf{\textit{3.12}}$$

The work function is different for each instrument and is calibrated from a known sample, e.g. thin film gold or copper. For the XPS instrument to create the spectrum of intensity vs. BE, the magnetic sector detector is placed close in space to the surface being analyzed, and a specific KE is measured by selecting the appropriate magnet conditions. Therefore, XPS can "sweep" the sector across various KEs (BEs) to analyze the BE spectrum of the photoelectrons coming from the material. An energetically broad sweep can be made (survey scan), followed by a very detailed, slow scan (detail scan) at higher energy resolution.

In general, quantification by XPS is based on integration of the peak area of the collected PE intensity signal after background subtraction versus BE (Figure 3.6), which is used to calculate *n*, the total number of atoms/cm^3. The intensity *I* of the specific peak is given as:

$$I = nf\sigma\theta\gamma\lambda AT \qquad \textbf{\textit{3.13}}$$

where f is the x-ray flux in photons/cm^2 sec, σ is the photoelectric cross-section of the electron orbital being collected, T is angular efficiency factor between x-ray and ejected PE, gamma (γ) is the efficiency factor for PE generation from that orbital, λ is the mean free path of the ejected PE, A is the area of the sample probed, and theta is the take-off angle (TOA). As previously stated, all these factors are empirically determined at and specific to each XPS chamber. Solving for n, the atomic density:

$$n = \frac{I}{f\sigma\theta\gamma\lambda AT} \qquad \textbf{\textit{3.14}}$$

$$n = \frac{I}{RSF} \qquad \textbf{\textit{3.15}}$$

The constant of proportionality in the denominator is called the relative sensitivity factor (RSF), and differs between instruments. The RSF is a convolution of the instrument response, transfer function of the detector, take-off angle of the sample to detector, and photoelectron yield of each specific element. The commercially available XPS software package MultiPak (developed by the XPS manufacturer Phi-Ulvac) allows for automated element identification and quantification, and has been calibrated for the XPS instrument used in this work. The quantification algorithm consists of background subtraction of inelastically scattered electrons and integration of signal peak areas between user defined limits, multiplying the integrated areas by the RSF, and then displays the results. Element identification is also automated, and peaks are assigned by comparing measured data to an extensive built-in reference library of peak position versus binding energy, as calibrated specific to that instrument. Relative atomic concentrations C_x where x is any element besides H or He can then be quantified as:

$$C_x = \frac{n_x}{\sum n_i} = \frac{I_x/RSF_x}{\sum I_i/RSF_i} \qquad \textbf{\textit{3.16}}$$

where n_x, the total number of atoms/cm^3 of element x, n_i the total number of atom of element i detected in the analysis volume, I_x the peak area of element x, RSF_x the RSF of x, I_i the individual peak intensity areas of element i in the analysis volume, and RSF_i the individual RSF for all element i in the analysis volume.

Angle-resolved XPS (ARXPS) was used to characterize ALD films as well. ARXPS is simply XPS performed at various take-off-angles (TOA) theta which are defined as the angle between the sample surface normal and the line from the sample-to-detector. ARXPS can be used to distinguish what components are closer to the surface by performing XPS at a more obtuse angle compared to a more acute, e.g., XPS at 90° and XPS at 15° will observe greater contributions from the bulk at 90° and greater contributions from the surface at 15°. The analysis depth *d* has an angle dependence expressed as:

$$d = \lambda sin\theta \qquad \textbf{3.17}$$

with parameters defined above.

XPS was used in this work to analyze and compare the ALD grown thin films. The films were exposed to room air during storage and transport before XPS analysis. Additionally, MBE grown CdTe on silicon substrates were used to compare against the ALD films. This strategy of using *external standards* allows us to determine the relative amounts of Cd and Te within a single sample and between samples, as well as the amount of tellurium bound in TeO_2 versus CdTe. Also, we can identify and quantify the relative amount of impurities within the sample, identify their location within the depth of the film using ARXPS, and identify different chemical environments of the impurities (e.g. SiO_2 versus another unique Si species).

XPS was performed in a Phi-Ulvac Versaprobe 3 XPS tool with a base pressure of 10^{-10} Torr. After initial survey and detailed scans of the as-delivered surface, argon sputtering at 3 keV for 0.5 minutes was used to clean adventitious carbon, oxygen, and the native oxide of the CdTe. A take-off angle of 45° between sample surface and incident x-ray probe was used to lower, with respect to 90°, contributions from the bulk of the sample while still maintaining sufficient signal to noise. Charging of the sample under analysis was compensated for by using a neutralizing beam of electrons and low-energy argon ions. Phi Multipak was used to quantify the survey spectra using relative sensitivity factors calibrated to this specific XPS tool by the manufacturer. CasaXPS[53] was used to peak fit the elemental scans to determine relative atomic concentration of individual peak components (e.g., oxidized Te versus Te in CdTe[54]). Full-width-half-maximum (FWHM) of individual peaks are constrained to be the same from pre-sputter data sets to post-sputter data sets to maintain consistency of analysis. The initially collected binding energy spectra were uniformly shifted to place the Cd 3d5/2 peak at a binding energy of 404 eV, because this peak showed no chemical shift across analysis of any sample. A Shirley background was used to fit the data. Collected counts were not smoothed to avoid introduction of artifacts. Additional XPS was performed on an MBE-grown CdTe on silicon sample. Multipak was used to calculate atomic percentages of the MBE-grown CdTe sample as a baseline to compare the ALD film against.

AFM was performed in atmosphere using a Veeco Nanoman AFM. Images were collected then analyzed using the Veeco Nanoprobe software to calculate amplitude, height, and phase in an attempt to correlate ellipsometry derived thickness to AFM derived height and root-mean-squared roughness. Also, AFM provides sub-micron topographical information on the film growth that neither SE derived parameters nor XPS chemical spectroscopy can provide.

3.4. Minority Carrier Lifetime Measurements

Focal plane arrays fabricated from MCT have various figures of merit for quantifying their performance, which are dependent on the minority carrier recombination lifetime (‘lifetime’) of the material.[13] In a semiconductor, the minority carrier recombination lifetime is a measure of the average time, upon generation of a free carrier, which an excited free electron (hole) remains in the conduction (valence) band before recombining.[55] Lifetime measurements are used to quantitatively characterize material quality, and the lifetime itself is dependent on material properties: the intentionally engineered properties of alloy composition and doping concentration, and on the unintentionally introduced concentration of bulk crystal defects and surface crystal quality, which result from non-ideal material growth and processing. In general, lifetime is maximized for semiconductor crystals containing minimal bulk and surface defects. Passivation reduces the concentration of surface states within the bandgap, thereby increasing the minority carrier lifetime.

PCD is used to measure lifetime, which involves the generation of charge carriers with light and then measuring the rate of recombination of charge carriers. Charge carriers are generated by electrical injection from an electrode or injection by absorption of above band-gap photons. Recombination of carriers can be the result of annihilation of an excited electron (hole) with a hole (electron) in the valence (conduction) band, releasing energy in the form of a photon, phonon, or kinetic energy transferred to an additional free carrier (

Figure 3.7). Also, recombination can take place through an energy level within the forbidden band-gap of the material, also known as the trap level. The trap level can be introduced through impurities, defects, and other deviations from an ideal crystal, including the presence of the semiconductor surface. The recombination rates are temperature dependent. When PCD is measured as a function of temperature, the technique is known as lifetime spectroscopy (LS). The passivation material effects on the minority carrier lifetime of MCT can be quantified through lifetime spectroscopy techniques[56] as discussed below.

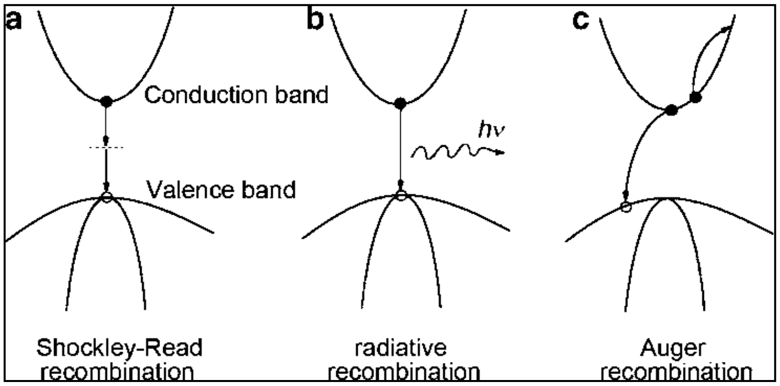

Figure 3.7. Recombination mechanisms in semiconductors.[56]

The criteria for effective passivation process include conformal deposition, low trapped charge density, and a good lattice match to MCT.[57]The effect of the passivation layer on the electrical properties of the substrate can be quantitatively analyzed through LS, where the carrier lifetime in a semiconductor material is measured as a function of temperature. A sample of material in thermal equilibrium will have an equilibrium concentration of charge carriers. For the example of an n-type semiconductor, the equilibrium concentration is given as:

$$n_0 = N_D \frac{1}{1 + \exp\frac{E_C - E_F}{kT}} \qquad \textbf{\textit{3.18}}$$

where N_D is the density of electron states in the conduction band, E_C the energy level of the conduction band minimum, E_F the Fermi level (dependent on dopant concentration), k is Boltzmann’s constant, and T is temperature in Kelvin. When excess carriers are introduced (e.g., through illumination of the semiconductor by above-bandgap light) excess carriers recombine, and the excess population will decay, re-establishing equilibrium. This is the lifetime and is referred to as the minority carrier lifetime when minority charge carriers are the source of recombination. In general, the recombination rate R of any process is simply the inverse of the lifetime τ of that process.

$$R = (\tau)^{-1} \qquad \textbf{\textit{3.19}}$$

The recombination of carriers occurs through intrinsic mechanisms and extrinsic mechanisms. Intrinsic recombination is present in an ideal semiconductor (i.e. a semiconductor crystal with no defects). Extrinsic recombination mechanisms result from the presence of non-idealities, such as surfaces, defects, impurities, etc. Extrinsic processes present parallel and competing mechanisms of recombination to the intrinsic processes. Intrinsic recombination in a semiconductor occurs through radiative recombination and Auger recombination. Extrinsic recombination takes place through Shockley-Read-Hall (SRH) and surface recombination (

Figure 3.7). Since each respective recombination pathway is possible, the total effective carrier lifetime (τ_{eff}) is given as:

$$\boldsymbol{\tau_{eff} = \left(\frac{1}{\tau_A} + \frac{1}{\tau_R} + \frac{1}{\tau_{SRH}} + \frac{1}{\tau_s}\right)^{-1}} \qquad \textbf{\textit{3.20}}$$

where τ_A is the Auger, τ_R the radiative, τ_{SRH} the SRH lifetime, and τ_s the surface carrier lifetime.

Radiative recombination occurs when an electron in the conduction band and a hole in the valence band annihilate across the band gap, and a photon with the energy of the bandgap is released to conserve total energy. Radiative recombination in this sense can be described as a two body interaction. When this process is present in an indirect bandgap semiconductor, a phonon is also involved. Therefore, in indirect bandgap materials, radiative recombination via a three body interaction is less probable when compared with a direct bandgap material. The radiative lifetime is given as:

$$\tau_R = \frac{1}{B(n_0 + p_0 + n_e)} \qquad \textbf{\textit{3.21}}$$

where n_e is the excess carrier density, which is experimentally controlled by changing the carrier injection density, n_o and p_o are the equilibrium electron and hole density, respectively. The parameter B is known as the thermal equilibrium spontaneous radiative generation rate:

$$B = 5.8 \times 10^{-13} \varepsilon^{1/2} \left(\frac{m_0}{m_e^* + m_h^*}\right)\left(1 + \frac{m_0}{m_e^*} + \frac{m_0}{m_h^*}\right)\left(\frac{300}{T}\right)^{3/2} \left(E_g^2 + 3kTE_g + 3.75k^2T^2\right) \tag{3.22}$$

where m_0 is the electron rest mass, m_e* and m_h* the effective electron and hole masses respectively, ε is the dielectric constant, k is Boltzmann's constant, T is the temperature, and E_g is the electronic band gap.

Auger recombination is a three body interaction in which an electron in the conduction band annihilates with a hole in the valence band, with the energy of the transition being transferred as kinetic energy to an additional free carrier in either the conduction or valence band as shown in

Figure 3.7. In n-type MCT, the Auger-1 (τ_{A1}) process is the dominant type of Auger recombination, where the energy released by the electron-hole pair annihilation is transferred as kinetic energy to another electron in the conduction band. The Auger-1 lifetime, τ_{A1},is given as:

$$\tau_{A1} = \frac{2{n_i}^2}{(n_0 + p_0 + n_e)(n_0 + n_e)} \tau_{A1}^i \tag{3.23}$$

$$\tau_{A1}^i = 3.8 \times 10^{-18} \varepsilon^2 \left(\frac{m_0}{m_e^*}\right)(1 + \mu)^{\frac{1}{2}}(1 + 2\mu)\left(\frac{E_g}{kT}\right)^{3/2} \exp\left(\frac{1 + 2\mu}{1 + \mu} * \frac{E_g}{kT}\right)|F1F2|^{-2} \tag{3.24}$$

where μ is the minority carrier mobility and |F1F2| is the overlap integral, which is used as a fitting parameter.[58] A constant value of 0.21 was used in this work.

SRH recombination is an extrinsic recombination mechanism, introduced by material defects, such as dislocations, vacancies, impurities, interfaces and surface states. It is a two body interaction, where an electron in the conduction band is trapped by a defect at an energy level in the band gap, followed by hole capture from the valence band. The carriers annihilate and release a phonon. The SRH lifetime is given as:

$$\tau_{SRH} = \frac{\tau_{n0}(p_0 + p_1 + n_e) + \tau_{p0}(n_0 + n_1 + n_e)}{p_0 + n_0 + n_e} \tag{3.25}$$

where n_0 and p_0 are the majority and minority carrier concentration, n_1 and p_1 are the electron and hole SRH carrier densities, respectively, n_e is the excess injected carrier concentration, and τ_{n0} and τ_{p0} are the electron and hole SRH lifetimes, respectively, given as:

$$\tau_{n0} = (N_t \sigma_n v_{th})^{-1} \tag{3.26}$$

$$\tau_{p0} = \left(N_t \sigma_p v_{th}\right)^{-1} \tag{3.27}$$

where N_t is the SRH center density, σ_n and σ_p are the capture cross sections of the SRH hole and electron capture centers, respectively, and v_{th} is the thermal velocity. The electron and hole SRH carrier densities are given by:

$$n_1 = N_C \, exp\left(-\frac{E_C - E_T}{kT}\right) \tag{3.28}$$

$$p_1 = N_V \, exp\left(-\frac{E_T - E_V}{kT}\right) \tag{3.29}$$

where N_C and N_V are the effective conduction and valence band densities,[5] E_T is the energy level of the SRH recombination center within the bandgap measured in proportion to E_g, E_V is the valence band maximum, and E_C is the conduction band minimum. From the SRH lifetimes, it is possible to obtain the $N_t\tau_p$ product.

However, it is not possible to unambiguously decouple the SRH center densities (i.e., N_t, the defect densities) from their capture cross sections.

The explicit temperature dependence of each recombination lifetime is used to model the experimental data gathered through PCD experiments, making it possible to measure the lifetime of the sample versus temperature to extract E_T, τ_{n0} and τ_{p0}. An example from previous work is shown below. An increase of the SRH lifetime after passivation therefore indicates a decrease in surface defect density (N_t), surface defect capture cross-section ($\sigma_{p,}\sigma_n$), or both. For example, previous work using MBE CdTe to passivate shown in Figure 3.8, lifetimes of samples from the same wafer of MCT were measured. One sample was measured as-grown, one was measured after growth then annealed under a Hg saturated atmosphere to remove Hg-vacancies, and a third one was measured after growth, anneal, and passivation by MBE CdTe. This figure illustrates qualitatively how the lifetime improves after anneal and further after passivation. Annealing MCT is required to annihilate Hg vacancies, which create a SRH trap state at ~0.75 E_g.[18,59] By fitting the experimental data to the above expressions for recombination lifetimes, it is possible to show that the SRH lifetime improves, indicating that passivation by CdTe was effective. The more important conclusion is that surface recombination was significant, and that passivation was necessary.

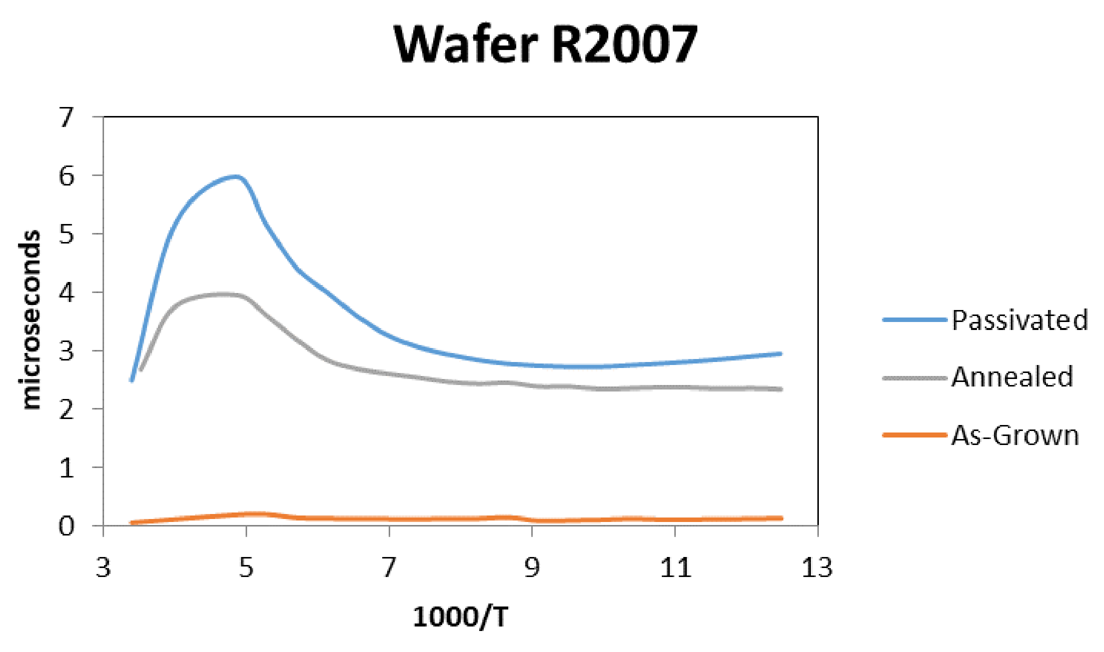

Figure 3.8. Tracking the minority carrier lifetime in MCT passivated by MBE CdTe through measurements of the as-grown, annealed, and then passivated lifetime demonstrates an increase in the effective lifetime after each beneficial process treatment.

3.4.1. The Photoconductive Decay Experiment

When above band-gap light is absorbed in MCT, e-h pairs are generated and carrier concentration of both majority (n) and minority carriers (p) increase above their thermal equilibrium values, which increases the sample conductivity σ_{total}:[57]

$$\sigma_{total} = \sigma_n + \sigma_p \quad \textbf{\textit{3.30}}$$

$$\sigma_n = n\mu_n q \quad \textbf{\textit{3.31}}$$

$$\sigma_p = p\mu_p q \quad \textbf{\textit{3.32}}$$

where σ_n, σ_p, μ_n, μ_p, and q are conductivity due to electrons (majority carriers), conductivity due to holes (minority carriers), electron mobility, hole mobility, and elementary charge, respectively. The majority carrier concentration n is controlled by the doping level. In the samples studied here, the doping is nominally 1 x 10^{15} cm^{-3}. Therefore, the minority carrier concentration in thermal equilibrium is $p=n_i^2/N_D$ (about 2 x 10^{11} cm^{-3} at 77 Kelvin) and orders of magnitude lower than the majority carriers. Photons with energy greater than the bandgap of the sample are injected into the sample during PCD using a 1550 nm solid-state laser. The injection level is kept below the doping concentration so that the change in majority carrier concentration by photon injection is negligible compared with the change in minority carrier concentration, which is an increase of many orders of magnitude. For example, given a doping of 1 x 10^{15} cm^{-3}, injecting 1 x 10^{13} cm^{-3} per pulse photons only changes the majority population by 1%, whereas the minority carrier population changes by 50 times. Therefore, the change in conductivity of the sample is then due to minority carrier generation and subsequent recombination. Contribution from majority carriers are negligible, and therefore change in conductivity is proportional to change in minority carrier population:

$$\Delta\sigma = \Delta p \mu_p q \qquad \textbf{\textit{3.33}}$$

The change in carrier population is time dependent. The continuity equation[5,55,60] for electron-hole (e-h) generation and recombination is a first order differential equation:

$$\frac{\partial \Delta p}{\partial t} = G - R \tag{3.34}$$

where G is the generation rate and R is the recombination rate, defined as the change in excess carrier population as a function of time:

$$R = \frac{\Delta p}{\tau} \tag{3.35}$$

where τ tau is the total recombination lifetime as defined in equation *3.2*. In the PCD technique,[57,61] the sample itself is used as a voltage divider in a simple bias-T circuit[61,62] seen in Figure 3.9 where V_0 is the battery voltage, R1 is the load resistance, and R2 is the sample resistance. As light is injected by a laser pulse, the conductivity of the sample increases as carriers are generated, then as the light turns off the carriers recombine back to their equilibrium value. The resistance across the load resistor R1 is converted to a voltage ΔV by the simple circuit and read out on an oscilloscope. As the light is turned off (G=0) the above equation becomes:

$$\frac{\partial \Delta p}{\partial t} = 0 - R = -\frac{\Delta p}{\tau} \tag{3.36}$$

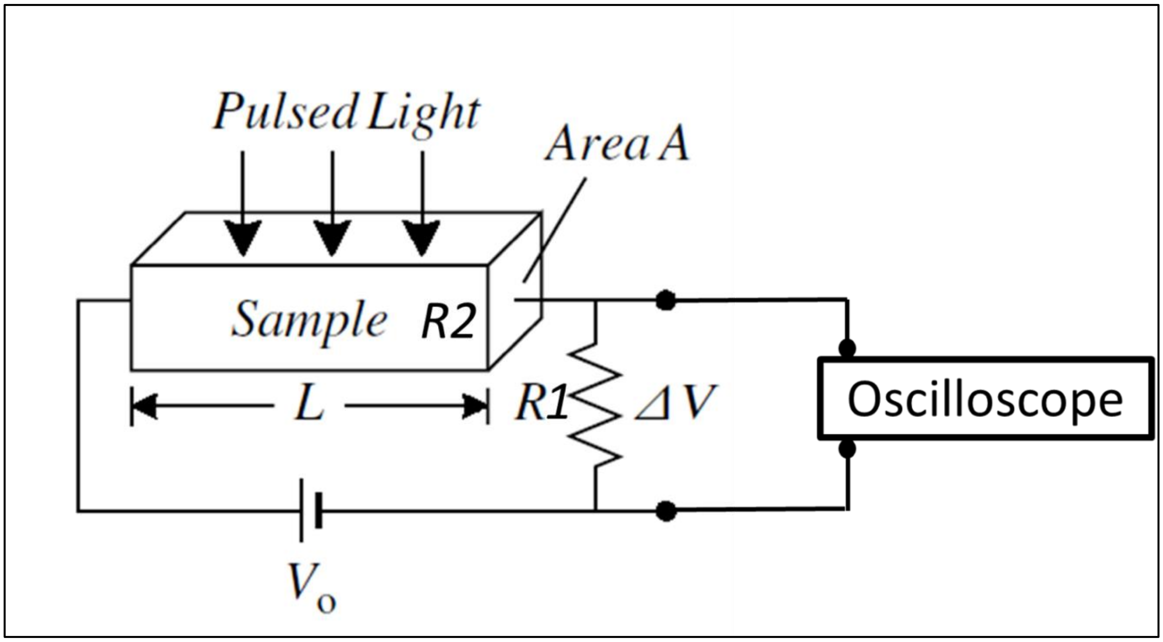

Figure 3.9. Bias-T circuit for measuring the voltage decay caused by e-h pair recombination (after [61]).

Separating variables to solve for Δp leads to the following equations:

$$\frac{d\Delta p}{\Delta p} = \frac{-1}{\tau} dt \tag{3.37}$$

Integration of left hand side (LHS) and right hand side (RHS) leads to:

$$\int \frac{d\Delta p}{\Delta p} = \ln(\Delta p) \tag{3.38}$$

$$\int \frac{-1}{\tau} dt = \frac{-1}{\tau} t \tag{3.39}$$

Solving for Δp results in an exponential time-dependence of the decay of the recombination lifetime:

$$\Delta p = e^{\frac{-t}{\tau}} \tag{3.40}$$

The excess carrier population will decay back to equilibrium through Auger, radiative, and SRH recombination mechanisms.

Now the voltage across the load resistor must be converted to a carrier concentration. Since the sample is used as a voltage divider, Ohm's Law V=iR can be re-arranged to show that the voltage across the bias-T resistor R1 is proportional to the sample conductivity.

$$\Delta V = \Delta i R1 \qquad \textbf{3.41}$$

$$\Delta V = \left(i_{on} - i_{off}\right) R1 \qquad \textbf{3.42}$$

where i_{on} is the current through R1 with the light on and i_{off} is the current through R1 in the dark. We define conductance as:

$$\Delta g = \Delta\sigma \frac{A}{L} \qquad \textbf{3.43}$$

where L is the sample length and A the cross-section. Now i_{on} and i_{off} are redefined using resistance defined as the inverse of conductance:

$$R_{on,off} = \frac{1}{\Delta g_{on/off}} \qquad \textbf{3.44}$$

$$i_{on/off} = V_0 \Delta g_{on/off} \qquad \textbf{3.45}$$

where $R_{on,off}$ and $\Delta g_{on,off}$ are the resistance and conductance of the sample during illumination and in the dark, respectively.

And now equation *3.42* re-arranges to give:

$$\Delta V = \frac{R_{off}^2 R1 \Delta g V_0}{\left(R_{off} + R1\right)\left(R_{off} + R1 + R_{off} R \Delta g\right)} \qquad \textbf{3.46}$$

This equation is made tractable by choosing a load resistor value (in this case 50 Ohm) much less than the sample R_{off} value (~10 kΩ at 77 K). Then we collapse equation *3.46* into:

$$\Delta V = \frac{R_{off}^2 R1 \Delta g V_0}{(R_{off})(R_{off} + R_{off} R \Delta g)} = \frac{R1 \Delta g V_0}{(1 + R\Delta g)} = R1 \Delta g V_0 \left(1 - \frac{\Delta V}{V_0}\right) \qquad \textbf{3.47}$$

The important conclusion in this derivation is that the change in voltage across the resistor R1 is proportional to carrier density if $R1 << R_{off}$ and $\Delta V << V_0$. R1 is intentionally chosen at 50 Ohms, and both low-level injection and using a D-cell battery with V_0=1.5 V ensures $\Delta V << V_0$. Then equation *3.47* collapses to

$$\Delta V = R1 \Delta g V_0 = R1 \Delta \sigma \frac{A}{L} V_0 = R1 \Delta p \mu_p q \frac{A}{L} V_0 \qquad \textbf{3.48}$$

Therefore,

$$\Delta V = \left(R \mu_p q \frac{A}{L} V_0\right) \Delta p \qquad \textbf{3.49}$$

$$\Delta V \sim \Delta p \qquad \textbf{3.50}$$

And with equation *3.40* plotting the logarithm of voltage as a function of time gives a linear relationship, where the slope is equal to the negative inverse of lifetime:

$$\ln \Delta V(t) \sim \ln \Delta p(t) \ = \ -\frac{t}{\tau} = -\frac{1}{\tau} t \qquad \textbf{3.51}$$

Thus, by plotting the natural log of voltage decay versus time and calculating the slope gives the lifetime.

3.4.2. Experimental Details

The samples to be measured by PCD were first placed into a vacuum micromanipulated cryostat (Janis Cryostation ST-500) and pumped out to <10^{-6} Torr using a Pfeiffer turbo pump cart to remove atmosphere and avoid condensation of water vapor onto the surface of the sample on cooling. A basic circuit diagram in Figure 3.9 outlines the bias-T circuit used to measure PCD. The cryostat allows the sample to be cooled down to cryogenic temperature, and able to apply contacts to the sample through micromanipulated tungsten probe tips internal to the cryostat. The probes are electrically fed through to the exterior of the cryostat. Then, the sample was cooled down to 77 K using flowing nitrogen into the cold finger of the cryostat. After stabilizing at 77 K, a thermocouple in contact with the cold finger, and a thermocouple in contact with the cryostat chuck were both at 77 K to confirm that the temperature was stable. A 1550 nm laser (Newport Laser, 5 mW/cm^2) was pulsed using an arbitrary function generator (AFG, model Tektronics AFG3000K). The oscilloscope was triggered to the same function generator. The laser was pulsed at 5 kHz repetition rate, 2% duty cycle (which equates to a 200 us period where the laser is on for 10 us and off for 190 us) to generate carriers in the sample (after first aligning the laser to the center of the sample with a visible 635 nm laser). A 1.5 V D-cell battery was used as a constant voltage source. The sample was electrically contacted by tungsten probe tips onto smashed indium contacts on the sample surface. The other contact was coupled by BNC cables to the front of the oscilloscope, where the final bias-T resistor (R1) was fed to ground. This allowed the DC portion of the current through the sample to flow to ground, while the AC component of the circuit was fed into the impedance-match input of the oscilloscope. The laser and oscilloscope were triggered by the same AFG clock in order to time the oscilloscope measurements. The voltage transients on the oscilloscope were then read out by custom LabView Virtual Instrument algorithms programmed by the author, stored on the PC, and then fitted to a log voltage graph by linear least squares algorithm to extract the slope of the log of voltage decay, and hence, the lifetime.

Chapter 4. Argon Plasma-Enabled Low Temperature Atomic Layer Deposition of CdTe from DMCd and DETe

4.1. Introduction

In this chapter a low-temperature plasma assisted ALD of CdTe was developed. SE was the primary characterization method used to optimize the ALD parameters. Through modelling of the growing ALD film, SE enabled observation of the change in thickness and ellipsometry parameters to be measured as a function of time, and to observe when these parameters reached an unchanging, steady state. This allowed direct observation of self-limited chemisorption of the precursor chemicals onto the growing surface and the self-limited decomposition of the surface adsorbed DMCd into Cd metal. Characterization of the grown films by XPS and AFM gave insight into the growth mechanism.

MCT is a narrow-gap semiconductor used in production of IR sensing devices. Mercury will out-gas from MCT during high temperature device processing and create Hg-vacancies (V_{Hg}). Vacancies limit the performance of the device by creating defect centers where charge carries recombine, lowering signal-to-noise (SNR). Parasitic dark currents (I_{dark}) can also limit performance. One major source of I_{dark} is the unpassivated or poorly passivated MCT surface. Passivation is a material and/or process which renders the surface benign during transport of charge through the device, i.e., the charge carriers do not recombine at the passivated surface. Developing a process for the low temperature ALD of CdTe is motivated by the need to maintain low processing temperatures of MCT semiconductor devices and to find a conformal deposition technique that can passivate the non-planar geometries found in MCT devices. Past work in MOCVD and ALD has demonstrated the process window for deposition of CdTe from DMCd and various tellurium precursors (e.g., DETe).[23-26,28] Film growth at temperatures lower than 220 °C have not been attained, and 220 °C is already too hot for processing MCT due to V_{Hg} formation. The rate limiting step to thermal MOCVD or ALD of CdTe has been determined[25] to be the decomposition of DMCd into cadmium metal, which catalyzes the Te-precursor decomposition into the growing CdTe surface.

As discussed in Chapter 2, surface passivation has typically been accomplished by UHV thermal evaporation of CdTe or other II-VI semiconductors (CdS, ZnS, and ZnSe). For example,

Figure 1.5 shows a cross section of mesa structures etched in MCT and subsequently coated with CdTe by MBE. Note the void formations, which are due to the inability of the line-of-sight deposition to deposit in a conformal manner on the surface. Infrared detector FPA architectures are either planar structures with minimal surface area, or mesa-delineated structures which can be highly non-planar. The mesa architectures have high-aspect ratio (HAR) structures that can present a challenge to evaporation of passivation materials due to the line-of-sight fashion of deposition, as shown in the above-mentioned figure. ALD offers a more conformal deposition technique where the surface to be passivated is exposed to vapor-phase sources rather than beams of sources. Although the eventual goal is to show conformal passivation of HAR structures, in this study, preliminary attempts at low-temperature ALD were conducted on planar silicon surfaces to demonstrate that an argon plasma can enable the decomposition of

DMCd at low temperate to enable ALD of CdTe. The atomic concentrations of the ALD film was compared to an MBE-grown sample.

4.2. Experiment

ALD of CdTe experiments were carried out in a KJLC ALD-150LX reactor (described previously in Chapter 3) with and without the use of a remote ICP plasma. The precursors studied in this project were DMCd and DETe supplied by SAFC HiTech.

4.2.1. Substrates

Prime-grade high-resistivity (001) oriented silicon wafers were used as-delivered to optimize ALD process conditions. The native oxide on the Si substrates was not removed before deposition experiments. Initial experiments attempted hydrofluoric acid wet etches to remove the native oxide and passivate the starting silicon surface by hydrogen termination. This oxide removal was motivated by using a starting substrate surface that was single-crystal, rather than amorphous as is the native oxide on SiO2. Deposition onto a single crystal substrate could allow for single crystal ALD films, as observed in MOCVD of CdTe onto Si(211).[63] However, after HF etching these substrates showed no growth activity by SE with or without the use of plasma. Oxygen/Argon, Hydrogen/Ar and argon only plasmas were attempted also to remove native oxide surfaces and no change in thickness or optical constants was observed by SE, indicating that no significant modification of the surface chemistry occurred. Chemisorption of DMCd onto oxidized surfaces was successful, but no further reaction with DETe was observed (without first the use of plasma to decompose the DMCd). Pulsing of DETe first onto the substrates exhibited no chemisorption as observed by SE. Therefore, the starting substrates used in this study always had the native oxide intact and DMCd was used as the first precursor pulse. H_2/Ar plasmas have been demonstrated to create a Cd-rich surface during etching of MCT in ICP etch reactors, hypothesized to be from formation of volatile hydrogen telluride (H_2Te) and non-volatile cadmium metal upon the etched surface.[64] The hypothesis tested by using H2/Ar plasma exposures of the DMCd exposed surface was to create a Cd metal terminated surface by reduction of DMCd to Cd by atomic hydrogen. Use of H_2/Ar plasma exposures onto the DMCd covered surface showed immediate decrease in thickness for any controllable level of H_2 flow into the ICP source (from 0.4 to 10 sccm at the nominal 200 sccm Ar flow through the ICP tube necessary to maintain laminar flow). Therefore, use of argon only was pursued.

4.2.2. In-situ spectroscopic ellipsometry observations

In-situ spectroscopic ellipsometry (iSE) was used to monitor the film growth and changes in surface chemistry. The Ψ and Δ are the raw data collected by the SE and used to model the optical constants of the growing film, the native oxide, and the substrate. This fitting in turn allows for determination of thickness as a function of time using a Cauchy model as discussed in Chapter 3. The Δ data can be shown in addition to the modelled thickness to demonstrate that while the model can be quantitative within the standard error calculated, the raw ellipsometry data is a qualitative measure of change that doesn't require extrapolation by a model to track the change in optical constants of the film, i.e., **unchanging Δ values alone can indicate when the surface reaches a self-limited state under exposure to precursor or plasma**. The modelled thickness values can give the growth-per-cycle which then can be used to indicate the fractional monolayer coverage per sub-cycle. An ideal ALD growth of CdTe in a complete monolayer per sub-cycle should have a growth per cycle (GPC) of 1.6 Å/cycle: one complete monolayer of Cd followed by one complete monolayer of Te should result in ¼ the unit cell lattice parameter of ~6.4 Å.[26] CompleteEASE software from JA Woollam was used to control the hardware and construct the model of film growth. SE enables rapid determination of growth rate and changes in surface chemistry to optimize the process parameters. Process development of the proper pulse length of precursor at deposition temperatures consists of exposure of the starting surface to the pulses of varying length and observing when saturation of the surface occurs as indicated by no further *increase* in thickness (e.g. Figure 4.1, with the Avrami Fit optimization explained below) or *change* in the ellipsometry parameters Ψ or Δ (e.g. Figure 4.2). Reaching steady state of any of these values indicates the composition and thickness of the film has reached a steady state and is self-limited. The length of time of the precursor pulses were thus developed to saturate the surface but avoid excess precursor consumption for both the DMCd and DETe sources. In a similar fashion, the plasma exposure time was developed.

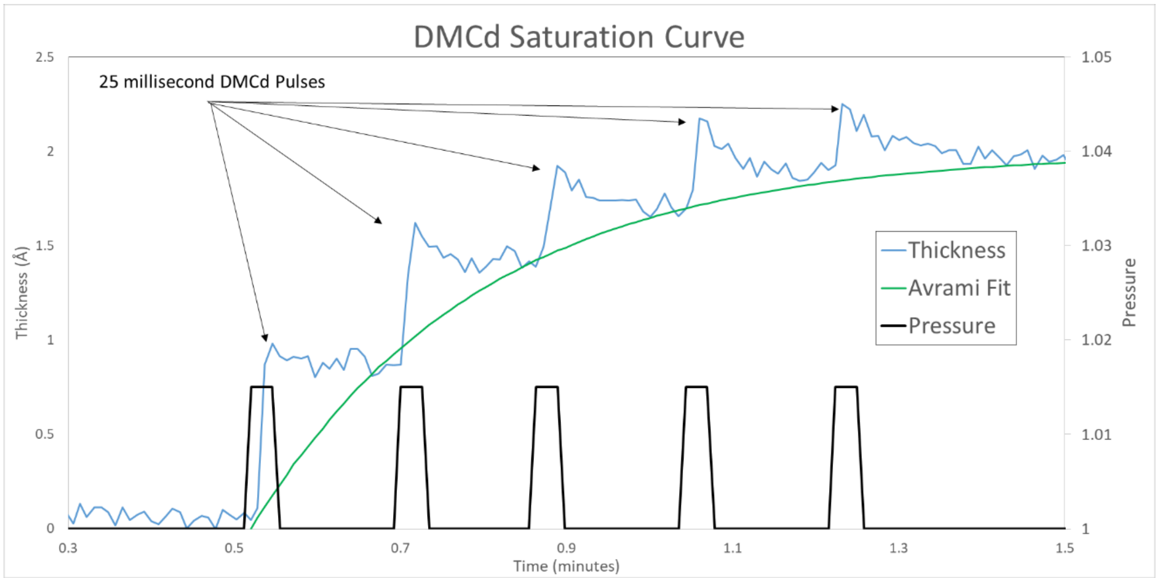

Figure 4.1. Saturated chemisorption of DMCd: observation of thickness increase by SE (left axis) during pulsing of DMCd. The thickness saturates after 5 consecutive pulses of 25 ms each, (indicating sufficient DMCd exposure is attained. The 25 ms pulses results in a 15 mTorr rise in base pressure (schematic; right axis). The dashed line is added as a guide to the eye.

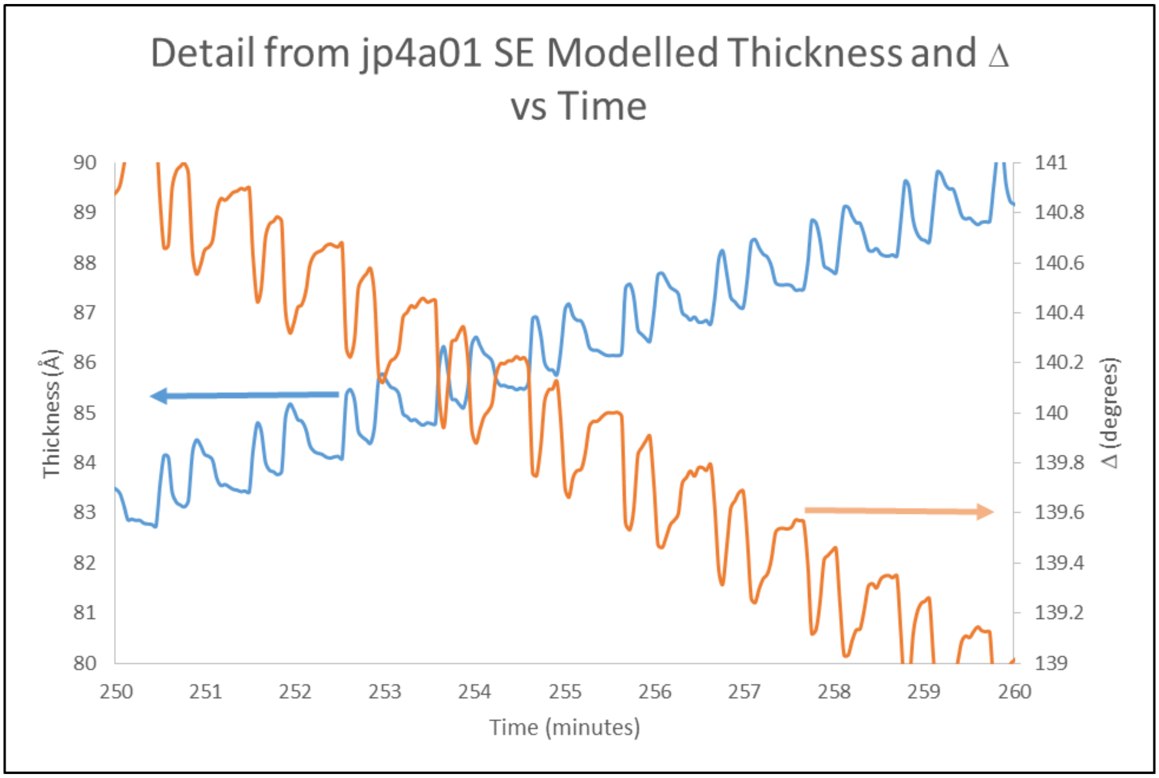

Figure 4.2. Thickness and Δ value versus time, showing that a steady value of thickness is reached when a steady value of Δ is unchanging versus time.

4.3. Results

All experiments were conducted at a temperature compatible with MCT processing (100° C) and additional growth temperature studies are left for future work.

4.3.1. In-situ Spectroscopic Ellipsometry

The ALD cycle consists of 1) exposure of the growth surface to pulses of DMCd, 2) purging of excess DMCd and by-products from the chamber, 3) exposure of the surface to argon plasma, 4) purging of plasma by-products, 5) exposure of the surface to DETe, and finally 6) purging of excess DETe and by-products. The following section explains how these parameters were developed, and relied solely on the use of in-situ SE.

For example, an increase in thickness during DMCd or DETe pulsing indicates irreversible chemisorption onto the surface, while exposure to argon plasma show a decrease in thickness. Irreversible chemisorption means once the molecular monolayer chemisorbs onto the surface, no amount of purging (purge time) would remove the monolayer at that specific deposition temperature and enables conformal deposition. Continued argon plasma exposure does not show a continued decrease in apparent thickness, indicating no sputtering of the surface takes place by the remote ICP source. Additionally, after the plasma exposure is ceased, no increase nor decrease in apparent thickness is observed, indicating the surface has both reached a steady state, and this state is irreversible until further exposure to Te precursor. Both the thickness increase and decrease during these processes reach a saturated value, indicating either self-limited chemisorption or steady state of decomposition is reached. In-situ SE enabled rapid process development of precursor pulse duration and plasma exposure times.

Thermal ALD of CdTe was attempted and the process was observed by in-situ SE using DMCd and DETe at 100 °C onto silicon with their native oxide starting substrates. No co-reactivity between these two precursors nor film growth was observed by SE in this temperature range without plasma. Exposure of the starting surface to DMCd leads to irreversible and saturated chemisorption as observed by SE (e.g., Figure 4.1**Error! Reference source not found.**), but no chemisorption of DETe onto either the starting surface or the DMCd terminated surface was observed during pulsing of DETe. However, exposure of the DMCd terminated surface to argon plasma leads to self-limited decomposition of the DMCd precursor as observed by SE. **Error! Reference source not found.**A sufficiently long plasma exposure of this surface reduces the SE thickness of the DMCd saturated surface down to a saturated value, and further exposure of the surface to plasma does not reduce the thickness any further, indicating that a steady-state of the surface has been reached. This surface is then reactive to the subsequent DETe precursor exposures, which irreversibly chemisorbs as observed by SE. Repeating the sequence of DMCd pulsing and purging, argon plasma exposure and purging, and DETe pulsing and purging resulted in film growth, while ***no growth was observed without the plasma step***.

4.3.2. Process Development

The first parameter to optimize was step 1, the DMCd pulse duration (see figure 4.1). The duration was developed for saturated monolayer formation, because DETe cannot chemisorb directly onto the substrate surface. This was accomplished by increasing the DMCd precursor pulses in duration, only to the point where no further thickness increase can be observed by SE, i.e., demonstrate the absorption is self-limiting and irreversible. This was intended to balance minimal use of precursor chemical against complete surface chemisorption coverage, in order to increase the number of experiments possible with a single canister of chemical.

The ICP source on the ALD reactor has a maximum output power of 1000 W. A power of 250 W was used during plasma exposure to not exceed similar ICP powers from previous ICP etching experiments.[66] Due to early success and schedule constraints, no other power levels were explored. The next parameter to be developed was step 3, the argon plasma exposure time. The initial 30 second exposure was reduced until the SE parameters reached a steady state at 12s based on the change of value of the modelled thickness of the DMCd layer during argon plasma exposure. Further reduction of the plasma exposure time below 12 s did not lead to SE parameters reaching steady state, or equivalently, the thickness did not reach a constant value. Therefore 15 s was chosen to both ensure complete decomposition of the DMCd into cadmium metal, while also lowering the plasma exposure time to lower the total time for the deposition to complete. The last parameter to be developed was step 4, the DETe pulse duration. This was developed by finding the minimum pulse time for complete self-limiting chemisorption of the plasma-exposed DMCd saturated surface, as observed by a self-limited thickness increase of the SE model. Again, no chemisorption, self-limiting or otherwise, was observed at all during DETe pulsing unless the DMCd saturated surfaces was exposed to argon at 250 W for a minimum of 15 s. The purge times were simply carried over from previously developed experiments using TMA and O_2 plasma for Al_2O_3 ALD.[66] The precursor vapor pressures are similar to TMA (~15 Torr) so the purge times are sufficiently long. Similarly, the argon plasma purge time was carried over, because effective O_2 purge time was previously demonstrated at the same process pressure and higher plasma gas flow rates. The developed parameters are listed in

Table 4.1 which consisted of 5 pulses of DMCd of 0.025 seconds each, separated by 0.5 seconds. Then, the chamber was purged for 10 seconds. The substrates were exposed to an Ar plasma at 250 W of power for 15 s, and then purged for 15 s. Then the DETe was pulsed for 0.100 seconds, then purged for 10 s. These sequential steps completed one cycle of CdTe ALD.

Table 4.1. Developed ALD parameters based on depositions onto silicon substrates from in-situ SE experiments.

DMCd multi-pulse	**DMCd multi-pulse purge**	**DMCd purge**	**Plasma Power**	**Plasma exposure time**	**Plasma purge**	**DETe pulse**	**DETe purge**
0.025 s	0.5 s	10 s	250 W	15 s	15 s	0.1 s	10 s

An iSE plot of film thickness versus time can be seen for a growth of CdTe at 100 °C (Figure 4.3). The measured parameters of Ψ and Δ are used to model the growing surface stack. The time-dependent model consists of a silicon substrate with a native oxide layer on top as the starting surface, and then an additional Cauchy-modelled film evolves on top during deposition (shown inset). The self-limited nature of the growth process is evidenced by the modelled thickness versus time data where each step in the developed ALD cycle is highlighted in Figure 4.4. The self-limited behavior can also be seen in the raw data for the Δ parameter, which also shows a self-limited change in the optical constants of the growing film, where the Δ value saturates after steps 1, 3, and 5 in the ALD cycle (Figure 4.4).

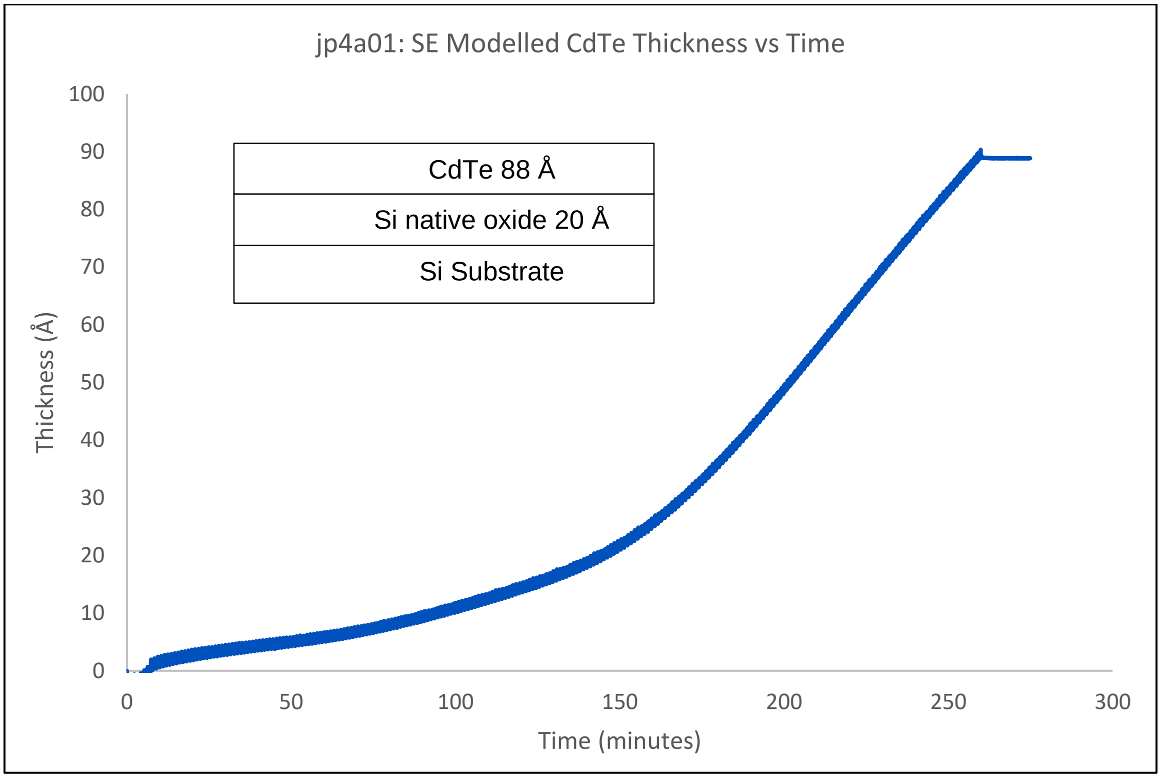

Figure 4.3. Modelled thickness vs time of 250 cycles of CdTe ALD growth on native oxide of silicon substrate at 100 °C. Inset stack shows layers and thickness of the layers used for modelling SE data (not to scale).

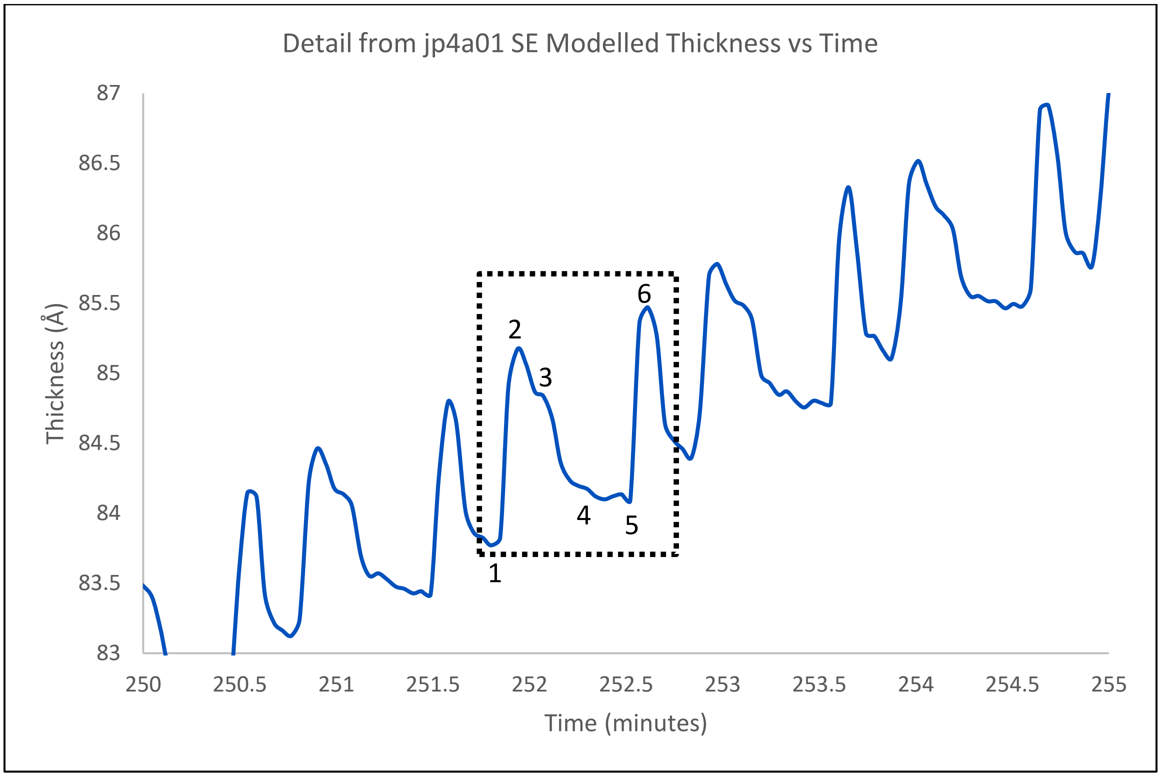

Figure 4.4. Zoomed in detail from to highlight the ALD process cycle: 1) DMCd pulse, 2) purge, 3) argon plasma exposure, 4) purge, 5) DETe pulse, and 6) purge which completes one cycle of CdTe PE-ALD. Dashed box outlines one complete cycle of ALD.

4.3.3. Yield Improvement Model

A quantitative model to optimize yield improvement by implementing CdTe ALD into a product line versus cost of processing is derived in general. Yield (y) is defined as a per-Å of added value (in dollars) to the product line as a linear function of thickness (h). The cost (k) is defined as per-second cost of the deposition process (in dollars) as a linear function of time. The thickness increase versus time was fit with the Avrami equation[65] (Figure 4.1), an empirical model for kinetics of chemisorption which can be part of. The form of the equation used was:

$$h = h_0\left(1 - e^{-t/\tau}\right) \qquad \mathbf{4.1}$$

where h_0 is the self-limited thickness of DMCd surface coverage and τ the time constant to reach this process. An example of fitting to experimental data gives values of 1.99 Å for h_0 and 16.5 s for τ, and the near self-limited thickness obtained at 5τ is 1.93 Å. Then to optimize the profit (P) as a function of time we have:

$$P = yh_0\left(1 - e^{-t/\tau}\right) - kt \qquad \mathbf{4.2}$$

Taking the first derivative of equation 4.2, setting to zero, and solving for maximum P at time t gives:

$$P' = -\frac{yh_0}{\tau}\left(e^{-t/\tau}\right) - k = 0 \qquad \mathbf{4.3}$$

$$\left(e^{-t/\tau}\right) = -\frac{k\tau}{yh_0} \qquad \mathbf{4.4}$$

$$-t/\tau = ln\left(-\frac{k\tau}{yh_0}\right) \qquad \mathbf{4.5}$$

$$t = -\tau \, ln\left(\frac{k\tau}{yh_0}\right) \qquad \textbf{4.6}$$

This general equation gives the optimal time t for values of $\ln(k\tau/yh_0)<0$, meaning $k< yh_0\tau$, meaning the cost of deposition product with tau must be less than the product of yield and h_0.

4.3.4. X-ray photoelectron spectroscopy

XPS analysis confirms that the ALD films are CdTe with a native oxide overlayer that is partially removed upon sputtering. XPS detailed spectra of the ALD films are shown in Figure 4.5. Peak assignments are consistent with previous XPS analysis of CdTe and its native oxide.[54] The CdTe is presumed to form a native oxide instantaneously on exposure to room air. The spectra were collected from the films as-grown (Figure 4.5 left column) to the XPS analysis chamber and again after sputtering (Figure 4.5 right column) by 3 keV argon ions for 30 seconds at a 45° angle with respect to the sample surface. Note that the angle of sputter will have shadowing effect on non-smooth surfaces (see discussion below). The Cd 3d peak does not show any shift or splitting as-delivered, nor after sputtering, consistent with previous reports.[67] The $Te3d^{5/2}$ spectra for the as-delivered sample (Figure 4.5c) exhibits two chemically different binding energy peaks, which are assigned to Te^{4+} from TeO_2 (576 eV) and Te^{2-} which is assigned to the tellurium from CdTe (572 eV). After sputtering (Figure 4.5d), the Te^{4+} or TeO_2 peak is reduced, indicating significant removal of the native oxide. The oxygen 1s peak as-delivered (Figure 4.5e) is a singlet, indicating one oxidized species is on the surface, which is assigned to the oxygen in TeO_2. The singlet splits into a doublet after sputtering (Figure 4.5f), and some TeO_2 remains present after sputtering. A second oxide peak is also observed, which is assigned to the oxygen in the SiO_2 native oxide on the silicon growth substrate. The appearance of the SiO_2 growth surface is due to the island-like microstructure of the ALD film as explained in the AFM section below. The as-delivered carbon 1s peak (Figure 4.5g) has three peaks, which are called C1, C2, and C3. After sputtering (Figure 4.5h), the C1 is absent, and as a result C1 peak is assigned to the adventitious carbon contamination from room air, although the low signal-to-noise of Figure 4.5h contains much higher uncertainty than the other photoelectron peaks. Qualitatively, the area of C2 and C3 peaks which remain after sputtering are quite small, indicating much less carbon content. C2 and C3 are left unassigned, but either peak possibly could be from the carbon in the methyl ligand of DMCd, which would be in a similar chemical environment, hence the same binding energy, to the terminal carbon of the ethyl ligand in DETe. That would indicate the other peak would be assigned to the ethylene carbon in DETe (closest to Te atom). Removal of the carbon contamination is left as future work, and its impact on passivation is unclear.

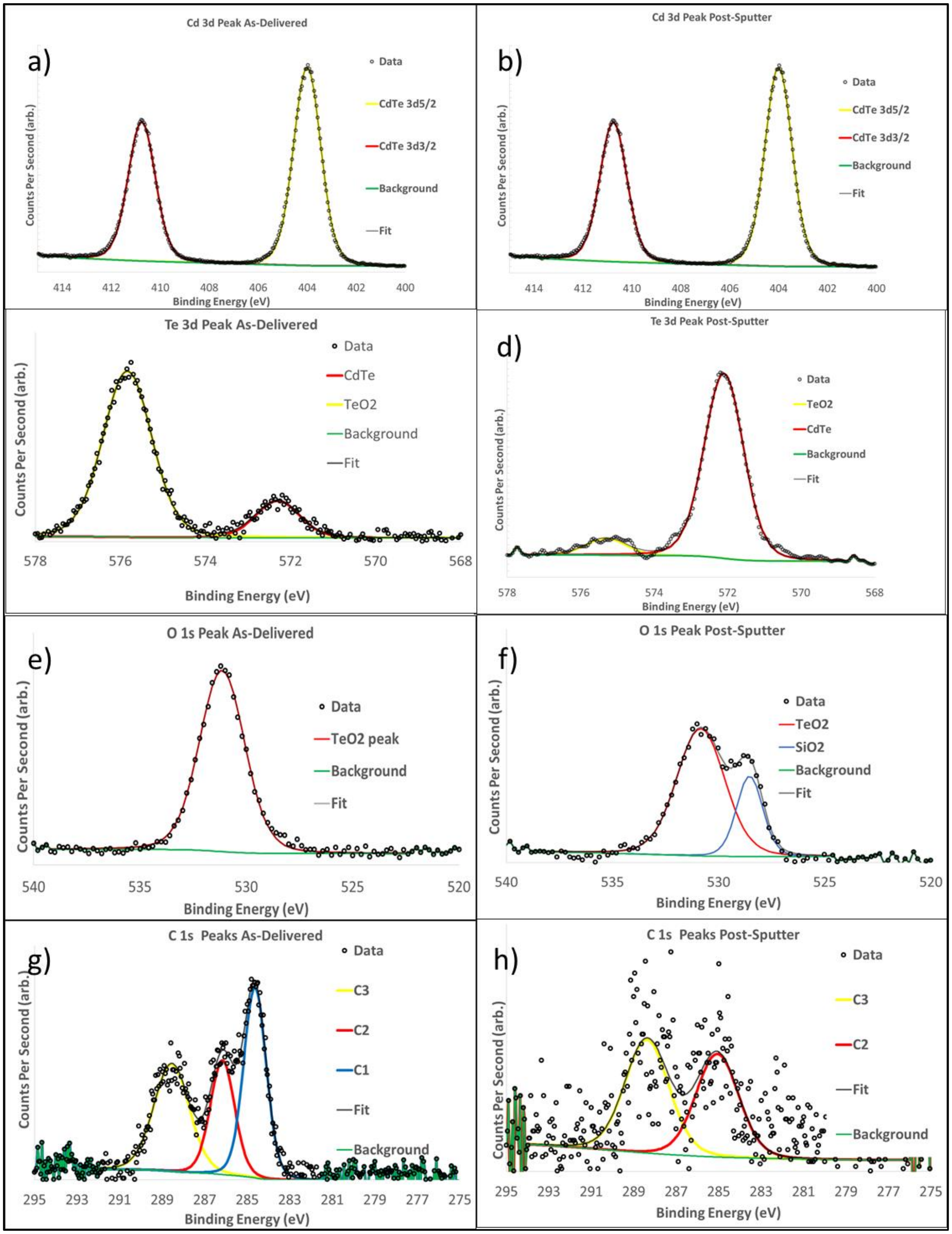

Figure 4.5. XPS spectra of as-grown (left column) and post-sputter (right column) CdTe ALD film surfaces. Cd (a,b), Te (c,d), O(e,f), and C 1s (g,h) are displayed.

The atomic percentages of the ALD film as a function of depth are compared against an 9 micron thick MBE-grown CdTe film grown on a silicon wafer. Both films show a Te deficiency in the as-delivered films. The Te deficiency is hypothesized to be a result of exposure to lab air because MBE grown CdTe sample also exhibits the same Te deficiency when exposed to air, while being grown by a different technique, and needs further investigation. Upon sputtering for 0.5 minutes at 3 keV argon ions, the stoichiometry is ~1:1 CdTe in the MBE film, while the stoichiometry of the ALD deviates further. After sputtering again for 2 minutes, the MBE film had a Cd:Te ratio of 1.2 indicating preferential sputtering of Cd from the MBE film, and the ALD film had no peaks besides C, O, and Si, indicating complete removal of the CdTe film.

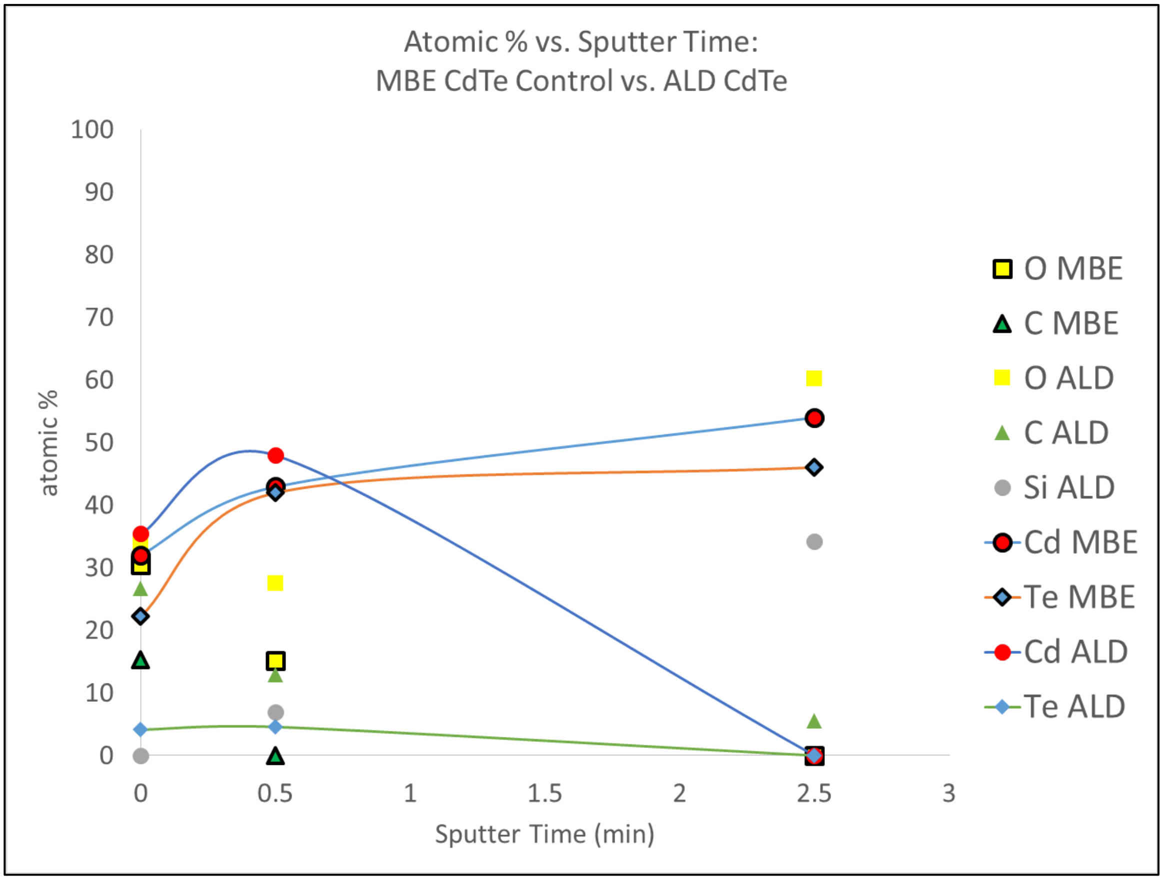

Figure 4.6. XPS depth profile of MBE grown CdTe sample: atomic concentration vs. sputtering time (depth). Cd:Te ratio deviates from 50:50 even after 2 min of sputtering.

4.3.5. Atomic Force Microscopy

AFM images from a 1 micron by 1 micron area are shown in Figure 4.7**Error! Reference source not found.Error! Reference source not found.**. Height images indicate islands of varying height upon a uniform background, while the phase images indicate, in conjunction with the height images, that the background material (brown color) differs from the island materials in topography, elasticity and/or adhesion properties.[68] The AFM is consistent with either a) complete CdTe monolayer formation followed by CdTe island growth, with the phase image resulting from microscopy on a flat background with curved islands of identical material, or b) CdTe island growth upon a silicon oxide surface, with bare silicon surface without CdTe nucleation sites nor growth of an ALD layer. The SE thickness is provided in Figure 4.3. Modelled thickness vs time of 250 cycles of CdTe ALD growth on native oxide of silicon substrate at 100 °C. Inset stack shows layers and thickness of the layers used for modelling SE data (not to scale). has two distinct growth-per-cycle regions, which indicates either a) a lower GPC region of sparse nucleation followed by a higher GPC region of denser growth, or b) a lower GPC region of smoother (complete monolayer) growth followed by a higher GPC region of rougher (island) growth of CdTe.

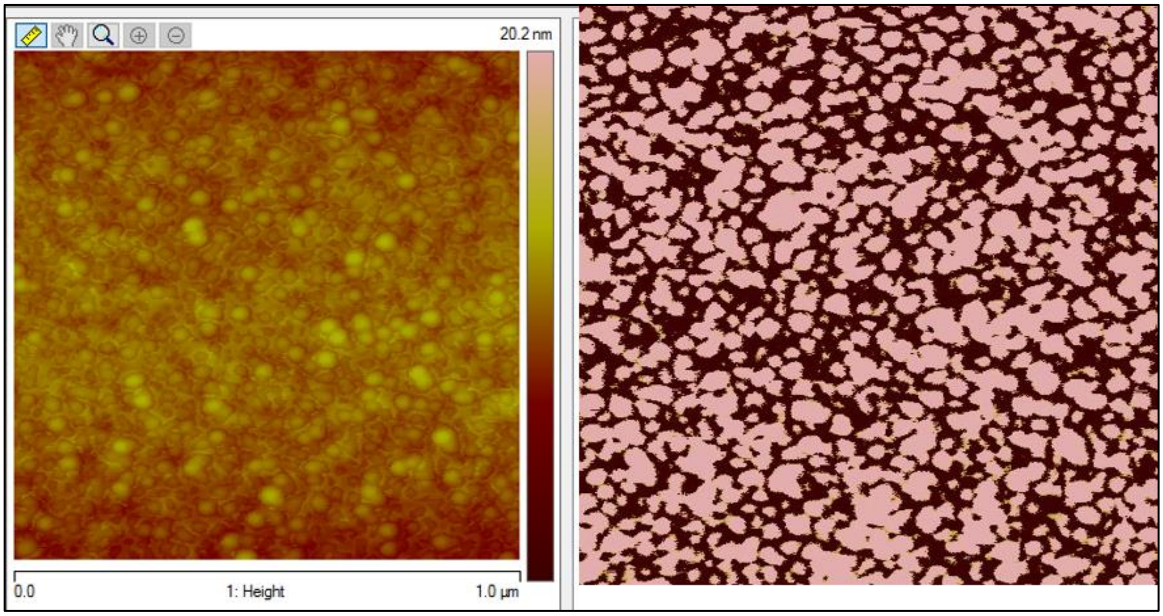

Figure 4.7. Atomic force microscope images of PA-ALD of CdTe on native oxide on silicon, indicating island formation. Left: height image of surface, showing nucleation sites. Right: Phase image, showing contrast between island sites (pink) against substrate/film (brown). Note the varying diameter of islands.

4.4. Summary, Discussion and Conclusions

At a substrate temperature of 100°C, in the absence of a plasma step, the ALD process for CdTe exhibits no growth, while including a plasma to decompose the DMCd surface enables growth as observed by SE. The completed films are CdTe with an over-layer of TeO_2, which can be removed by sputtering as indicated by XPS. Residual carbon remains in the film after sputtering. The AFM images indicate rough island-like growth, consistent with a substrate inhibited nucleation and coalescence, also indicated by the two distinct GPC regions observed with in-situ SE; and consistent with a small TeO_2 peak remaining after sputtering due to the 45° angle of argon ion sputtering relative to the substrate. The rough film would cause a shadowing effect where some TeO_2 will remain post-sputtering.

As discussed in Chapter 2, the rate-limiting step in MOCVD CdTe is thermal decomposition of CdTe into Cd-metal. In this work, Ar* is hypothesized to decompose the surface adsorbed DMCd into Cd metal. Metal ALD onto dielectric substrates often exhibits sparse nucleation of metal sites first, then growth by increasing the metal nanoparticle (NP) size until coalescence occurs and layer-by-layer (LBL) growth mechanism initiates[69,70] (e.g., PA-ALD of Pt onto SiO_2 substrates[71,72]). The wetting of a high-surface energy metal (e.g. Cd) onto a low-surface energy dielectric (e.g., SiO_2) leads to a high surface contact angle at the Cd-SiO_2 interface, driven by minimization of surface energies and chemical potentials [73]. During some ALD process, diffusion and incorporation of small NP to larger ones (Ostwald ripening) leads to a broad size distribution. When diffusion is absent, the NP size distribution is narrow (see Figure 4.8**Error! Reference source not found.**). The AFM height image shows a distribution of island diameters, consistent with both 1) Ar* decomposition of DMCd into Cd metal, and 2) diffusion of Cd NP into islands, leading to island CdTe growth. The overall mechanism specific to the CdTe system of this chapter is illustrated in Figure 4.9**Error! Reference source not found.**.

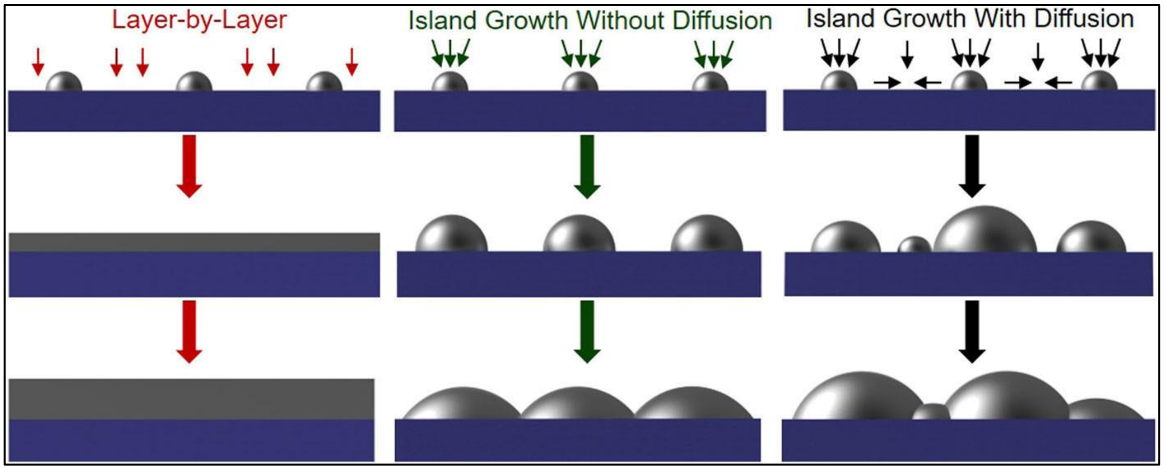

Figure 4.8. Illustration of LBL growth (red arrow), island growth without diffusion (green arrow), and island growth with diffusion (black arrow).[70]

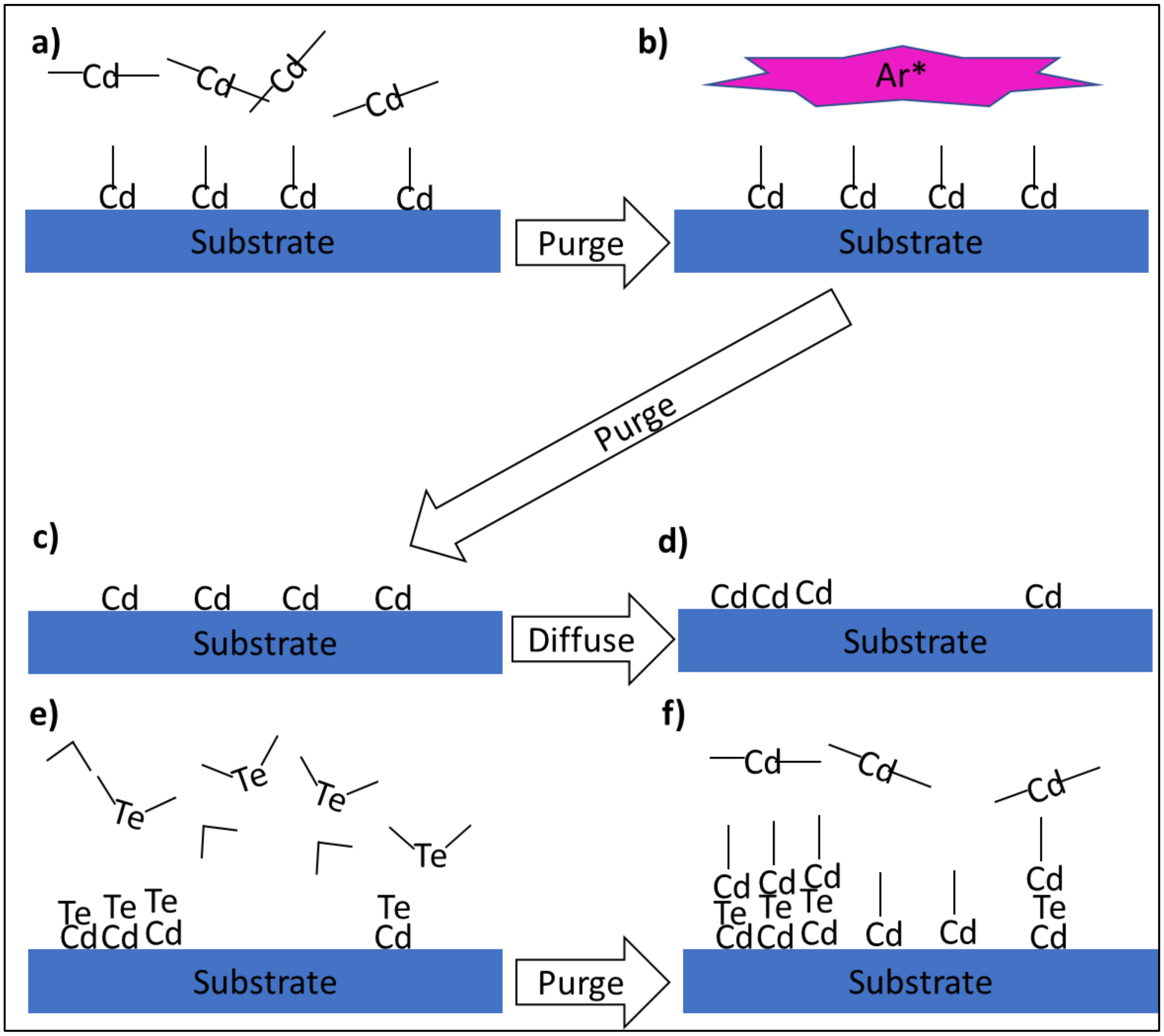

Figure 4.9. Proposed growth mechanism of the developed ALD process: a) DMCd pulse leads to chemisorption onto SiO2 surface (substrate) followed by purging; b) Ar* exposure of DMCd and purge into c) Cd metal sites, d) which diffuse and form islands, e) which catalytically decompose DETe into CdTe islands, then f) pulsing of DMCd returns surface to condition a).

Thus, the argon plasma enables rough CdTe film growth at temperatures lower than that possible with any thermal deposition technique by decomposition of surface DMCd into Cd metal. Future work will include growing and characterizing thicker films to illuminate the growth mechanism, which is critical for understanding and controlling the microstructure of the ALD CdTe films. Also, electrical characterization of ALD CdTe grown on MCT surfaces should be studied to demonstrate effective passivation. ALD onto high-aspect ratio structures should also be tried, to demonstrate conformal deposition. The activation of the DMCd through argon plasma exposure has been demonstrated at a proof-of-concept level for the low-temperature PE-ALD of CdTe.

Chapter 5. Plasma Enabled Atomic Layer Deposition of CdTe from Bis(trimethylsilyl)telluride (BTMSTe) and Dimethylcadmium

5.1. Introduction

Substituting BTMSTe for DETe in plasma enabled ALD of CdTe was investigated. BTMSTe offers a substitute for the more toxic DETe. Also, BTMSTe is now offered by more vendors due to increased research in the deposition of germanium antimony telluride (GST) by ALD for phase change memory applications. Deposition onto both native oxide/silicon and MCT substrate surfaces was investigated as a function of temperature.

5.2. Experiment

The ALD investigations presented in this chapter were carried out in the same reactor as those described in chapter 4, with the BTMSTe precursor substituted for DETe. This process is referred to as Process **A**. The pulse duration for BTMSTe was developed in the same fashion as the DETe: to lower precursor consumption, while ensuring complete self-limited chemisorption, in the same way as for the precursors in chapter 4. The pulse sequence is the same as in chapter 4, except for the use of BTMSTe instead of DETe in step 5.

In addition to growth on native oxide-silicon substrates, growths were conducted on MCT substrates. The MCT substrates were oriented (211)B, meaning the Te sub-lattice terminates the growth direction. The MCT substrates were prepared by 30 second etch in 200 μL bromine dissolved in 100 mL ethylene glycol, to etch into the surface approximately 250 nm prior to ALD growth.

Thermal ALD onto silicon substrates was done at 100 °C, in an attempt to directly co-react DMCd and BTMSTe. The attempt used the developed Process A parameters, but without steps 3 and 4, the plasma exposure and purge steps, discussed below.

Separate layers were grown using Process A at various temperatures: 50, 75, 100, 115, 125, and 150 °C onto silicon substrates to study the film GPC dependence on temperature. Also, growth at 50, 115, and 150 °C was attempted onto MCT substrates to understand the GPC temperature dependence, although the higher temperatures are not compatible with MCT device processing, it could illuminate the growth mechanism.

Process A was repeated 250 times for each experiment at temperature. The 250 cycle layer was selected to grow thicker layers compared to Chapter 4 with an anticipated result of analysis by XPS to reveal less oxidation upon sputtering away the native oxide that the CdTe ALD film was expected to form upon air exposure after unloading from the ALD reactor.

Film GPC was measured in-situ using the Woollam M2000 SE. Surface chemistry was analyzed by XPS. Additionally, TEM was performed on cross-sections of growth on silicon and MCT growth substrates. High-brightness XRD was used to examine film orientation on MCT substrates.

5.3. Results

5.3.1. Thermal growth for Process A

Developed ALD parameters are listed in Table 5.1 For the attempts at thermal ALD using BTMSTe, the ALD was performed at 75 °C and the sequence consisted of 1) exposure of the growth surface to pulses of DMCd, 2) purging of excess DMCd and by-products from the chamber, 3) exposure of the surface to BTMSTe, and finally 4) purging of excess BTMSTe and by-products. The pulse durations were developed as in Chapter 4 to lower precursor consumption while still reaching a saturated GPC. The precursor pulses were self-limited within steps 1 and 3. However, GPC continually decreased until no further thickness increase was possible around ~17 Å total thickness after DMCd and BTMSTe were each pulsed 5 times, demonstrating that thermal ALD using co-reaction between DMCd and BTMSTe is not feasible without the use of argon plasma exposure of the DMCd saturated surface. This is in contrast to the process in Chapter 4 using DETe: no growth at all was observed after any number of DETe pulses onto the DMCd saturated surface, while some initial growth was observed here with BTMSTe, although eventually saturating. Additionally, when cycle steps 1 and 3 were interchanged, i.e. BTMSTe was pulsed first as step 1, a very large thickness increase was observed on the first pulse, and no additional growth was possible regardless of the number or length of pulses after that first BTMSTe pulse, in agreement with observations by Eom, et al.[74] and is attributed to surface site de-activation/self-passivation effect of the silyl ligands of BTMSTe.

Table 5.1. Developed ALD parameters based on depositions onto silicon substrates.

DMCd multi-pulse	DMCd multi-pulse purge	DMCd purge	Plasma Power	Plasma exposure time	Plasma purge	BTMSTe pulse	BTMSTe purge
0.025 s	0.5 s	10 s	250 W	15 s	15 s	0.1 s	30 s

5.3.2. PA-ALD

For plasma based Process A, on silicon and MCT substrates, in-situ SE was used to monitor the thickness evolution during each growth at each temperature. Figure 5.1 is a plot of the average GPC from each growth vs temperatures, which revealed a non-linear decrease of GPC as a function of temperature for growth on silicon. This could be due to either increased roughness of the film deposition or site de-activation by the silyl ligand. The error in the fitted data is less than1% as calculated by the CompleteEASE software and model. The growth on MCT substrates could be independent of temperature. Figure 5.2 is a plot of SE derived thickness vs time for each growth on silicon substrates at temperature for each 250 cycle ALD run. Again, this highlights the decrease in GPC with temperature. The initial thickness increase during the first few pulses increases with temperature, while the overall GPC decreases. TEM results discussed below confirm that the thickness measurement is nominally the same as SE and confirms the SE modelled GPC does not include thickness due to roughness. The GPC are summarized in

Table 5.2. The GPC of ALD on silicon shows a decrease as the

temperature increases.

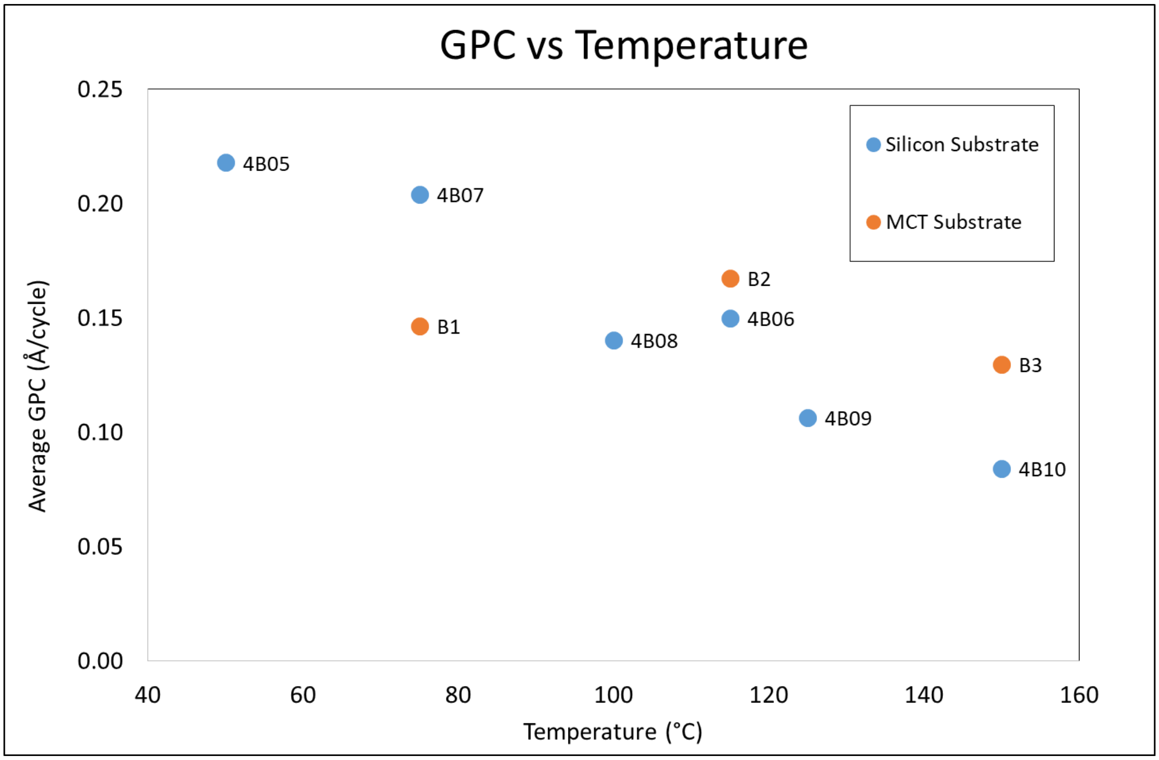

Figure 5.1. Temperature dependence of growth-per-cycle of ALD of CdTe on Si and MCT substrates.

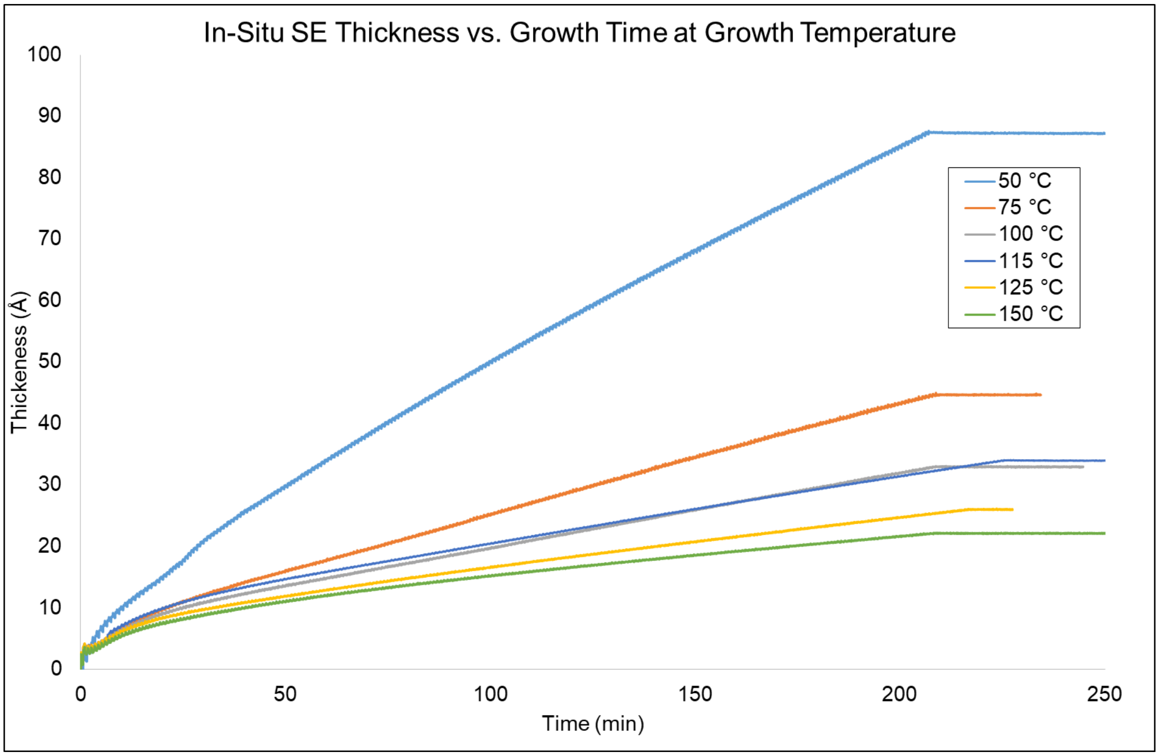

Figure 5.2. In-situ SE of ALD on Si substrates. SE-derived thickness versus growth time at various growth temperatures.

Table 5.2. Substrate, growth temperature, number of cycles, and SE-derived thickness and growth-per-cycle.

Sample	Substrate	Temp. (°C)	# of cycles	Thickness (Å)	GPC (Å/cycle)
4B05	Si	50	250	54	0.22
4B07	Si	75	250	51	0.20
4B08	Si	100	250	35	0.14
4B06	Si	115	250	38	0.15
4B09	Si	125	250	27	0.11
4B10	Si	150	250	21	0.08
B1	MCT	75	250	37	0.15
B2	MCT	115	250	42	0.17
B3	MCT	150	250	32	0.13

An expanded view of the SE data (Figure 5.3) demonstrates similar growth behavior using BTMSTe to CdTe ALD using DETe: each pulse and purge step can be seen, indicating layer-by-layer growth: as highlighted in the figure 5.3: 1) DMCd pulse and purge, showing a sharp increase in thickness, 2) Argon plasma exposure and purge, showing an exponential decrease in thickness during exposure, and 3) BTMSTe pulse and purge, showing a sharp increase in thickness.

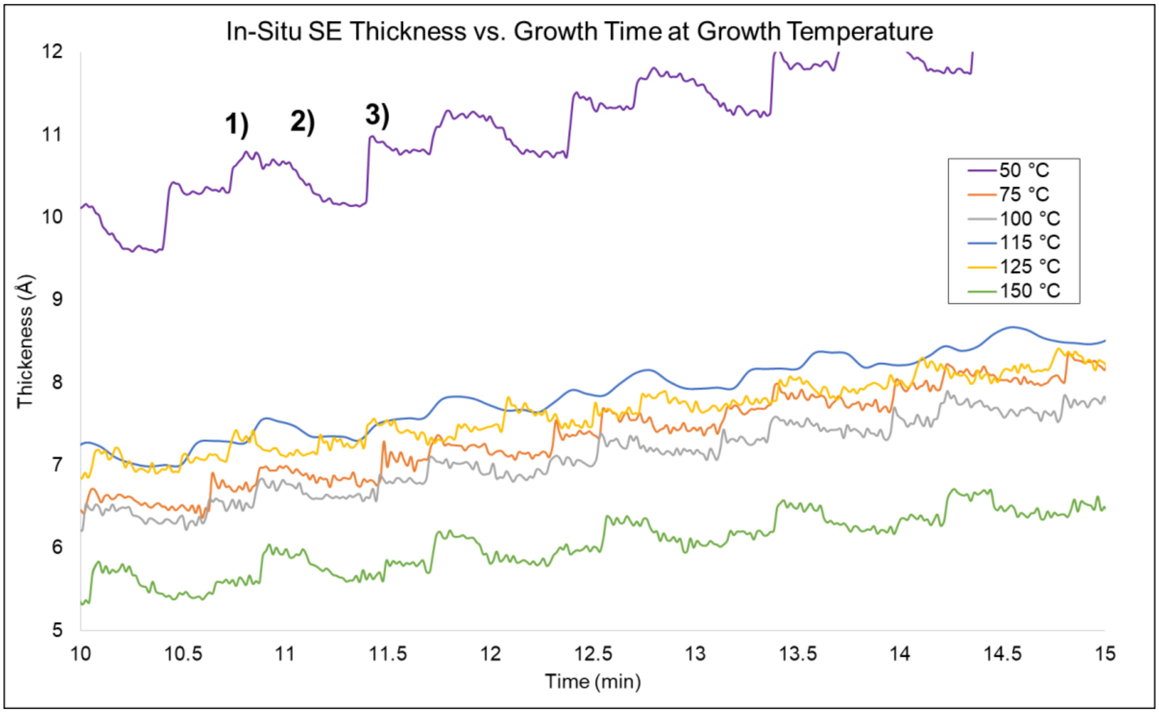

Figure 5.3. Expanded view of the In-situ SE-derived thickness data versus growth time at various growth temperatures, showing the thickness change during individual pulses of precursor and plasma exposure: 1) DMCd pulse and purge, 2) Argon plasma exposure and purge, and 3) BTMSTe pulse and purge.

5.3.3. TEM of Process A

TEM of growth on silicon was performed at Arizona State University through a collaboration with the US Army Research Laboratory (**Error! Reference source not found.** and **Error! Reference source not found.**). This growth was 250 cycles of Process A onto silicon at 75 °C. The TEM showed the ALD films consist of rough grains in texture and of nominally the same thickness as calculated by the in-situ SE model. The grains in the CdTe film have several orientations. Lattice spacing measurements of 3.25 Å indicate the grains are CdTe, as the lattice spacing can be indexed to the <002> directions of CdTe (Figure 5.5). For cubic materials like CdTe, lattice spacing can be indexed according to the formula:

$$d = \frac{a}{\sqrt{h^2 + k^2 + l^2}} \tag{5.1}$$

where d is the measured lattice spacing, a is the lattice constant of the unit cell (i.e., 6.478 Å), and the lattice directions are h, k, and l. There is no orientation in registry to the substrate, as there is an amorphous native silicon dioxide present. Also, the grains are polycrystalline and appear to be randomly oriented.

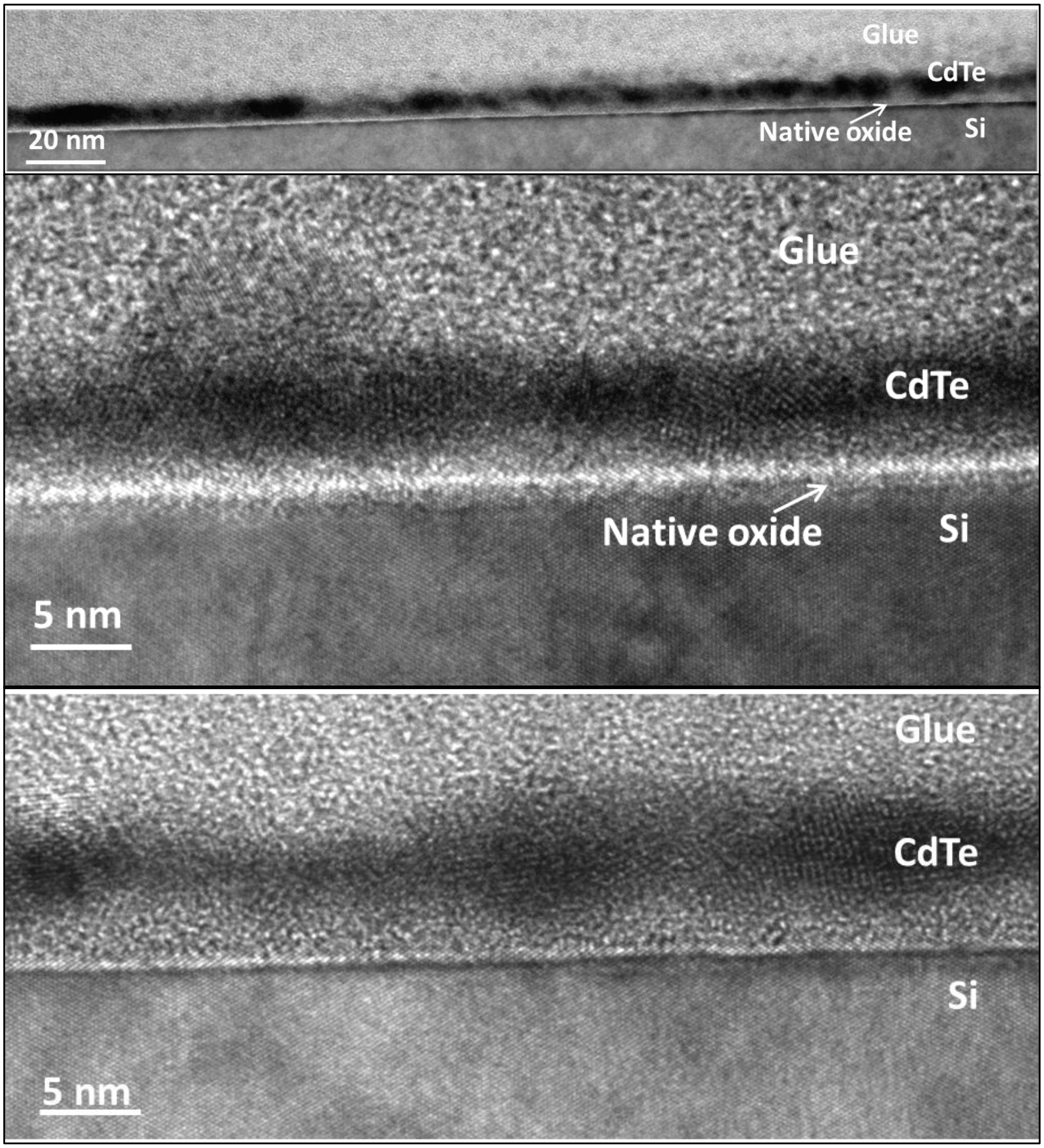

Figure 5.4. Cross-sectional TEM images of 250 cycles of CdTe ALD onto silicon substrate deposited at 75 °C, showing nanocrystalline nuclei of CdTe.

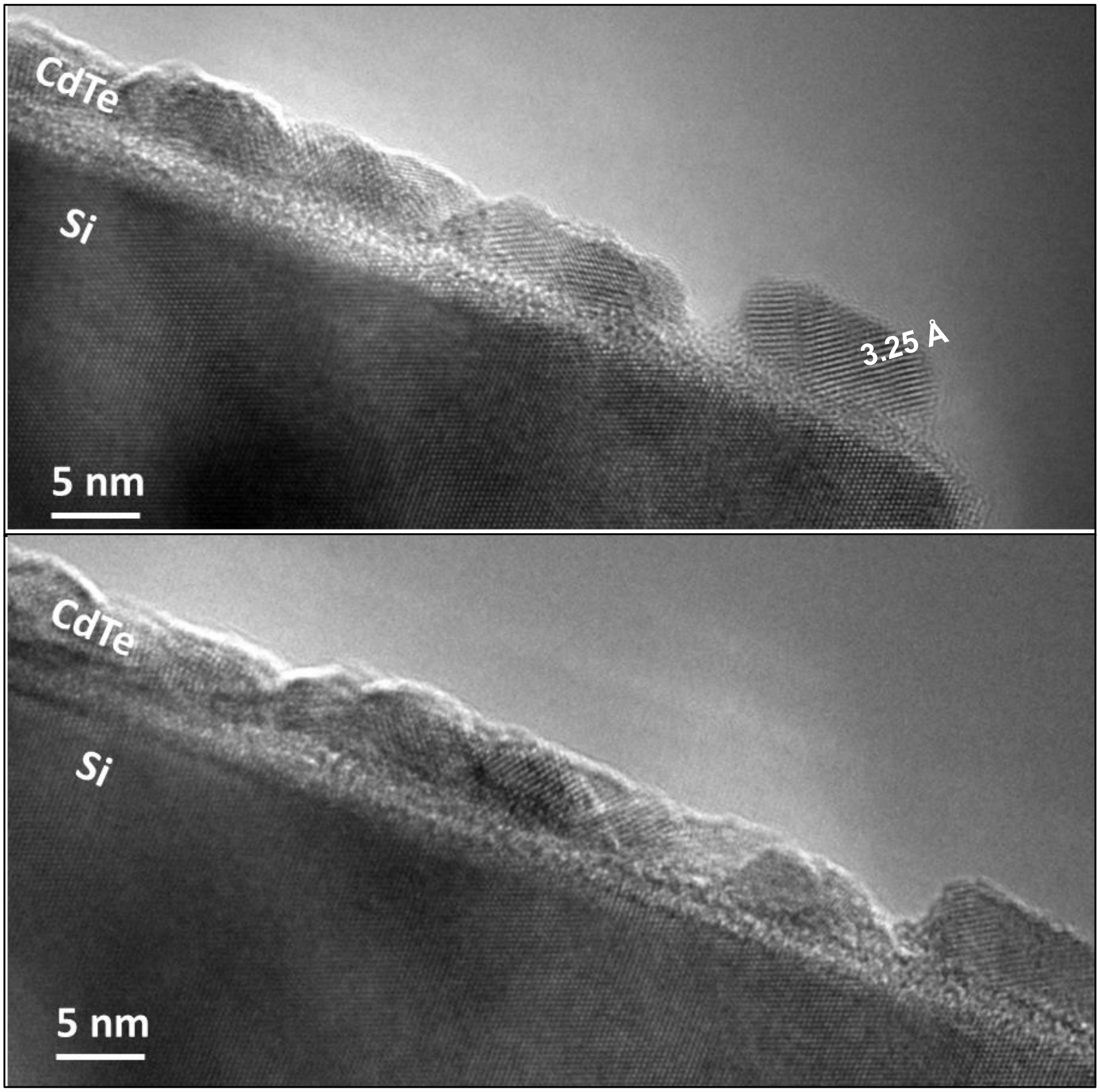

Figure 5.5. Cross-sectional TEM of sample in Error! Reference source not found.**. Crystal planes spacing are approximately 3.25 Å in the labeled grain, indicating a (002) oriented crystal of CdTe with a=6.478 Å lattice constant.**

5.3.4. XPS of Process A

Angle-resolved XPS was performed on the growths on silicon substrates at 75 °C and 150 °C. The XPS indicated that the ALD films consisted of CdTe with a native oxide and carbon contamination on the surface region that is reduced upon sputtering inside the XPS chamber, similar to the films examined in Chapter 4. These samples were sputtered by Ar+ ions for 30 s at 3 keV, removing most of the TeO_2 peak, indicating removal of most of the native oxide, which could be around 10 Å. Table 5.3 lists the atomic percentages before and after sputtering at 90° and 15° for samples grown at 75 and 150 °C. Analysis at 90° reveals atomic percentages that are weighted towards the bulk, containing contributions from both the surface and bulk of the ALD film and the surface of the growth substrate. Analysis at 15° is weighted towards the surface and the ALD film. The films grown at lower temperature contain higher atomic percentages of CdTe. The films grown at higher temperature have much higher silicon and carbon contamination. Sputtering removes some carbon from the films at both growth temperatures and at both angles of analysis. However, sputtering increases the atomic percentages of silicon in both angles of analysis and both growth temperatures. Silicon at% is much higher at 15° which indicates silicon is contained within the ALD film and is a contaminant from the BTMSTe. Additional silicon peaks come from the silicon growth substrate. Carbon contamination is higher at higher growth temperature. Oxygen is reduced upon sputtering in the lower growth temperature films, while it is increased at higher growth temperatures. This observation could support that the TeO_2 is reduced upon sputtering of the lower growth temperature, while at higher growth temperature, the sputtering probably removes what little CdTe and CdTe oxides are present to reveal more of the silicon oxide substrate, which would increase the oxygen atomic percentages after sputtering the surface.

Table 5.3. Relative atomic concentration of the surfaces of samples 4b07 and 4b10, CdTe ALD films grown at 75 and 150 °C, respectively, on silicon, as quantified by survey spectra from 90° and 15° angle of analysis, relative to surface normal. Film thickness of 4b07 and 4b10 were 51 and 21 Å respectively (see Table 5.1).

	4b07	**C1s**	**O1s**	**Si2p**	**Cd3d5**	**Te3d5**	**Si:Cd**	**C:Si**
90°	As-delivered	47	20	11	11	10	1.0	4.1
	Sputter x1	32	22	16	16	14	1.0	2.0
15°	As-delivered	51	22	7	12	9	0.6	6.9
	Sputter x1	38	9	19	19	15	1.0	2.0
	4b10	**C1s**	**O1s**	**Si2p**	**Cd3d5**	**Te3d5**	**Si:Cd**	**C:Si**
90°	As-delivered	61	18	19	1	1	16.2	3.2
	Sputter x1	29	36	33	1	1	40.9	0.9
15°	As-delivered	75	10	12	1	1	9.1	6.2
	Sputter x1	46	29	22	1	1	17.4	2.0

The Te 3d5/2 (Figure 5.6) peak as-delivered and after sputtering is consistent with CdTe with a native oxide ([75]). Since these films were grown on silicon, some PE coming from the Si wafer substrate are expected to be collected. However, comparing at% from 90° (weighted towards collecting PE from the substrate) and 15° (weight towards PE collected from the ALD film) indicates silicon contamination within the ALD film itself, arising from the silicon atoms in the BTMSTe precursor. The Si at% is particularly elevated in growth at 150 °C compared to 75 °C, while the film is poor in CdTe. Also, the ratio Si:Cd is much greater at elevated growth temperature. Again this is consistent with BTMSTe having a site-blocking effect, which appears to be more significant at elevated temperature.

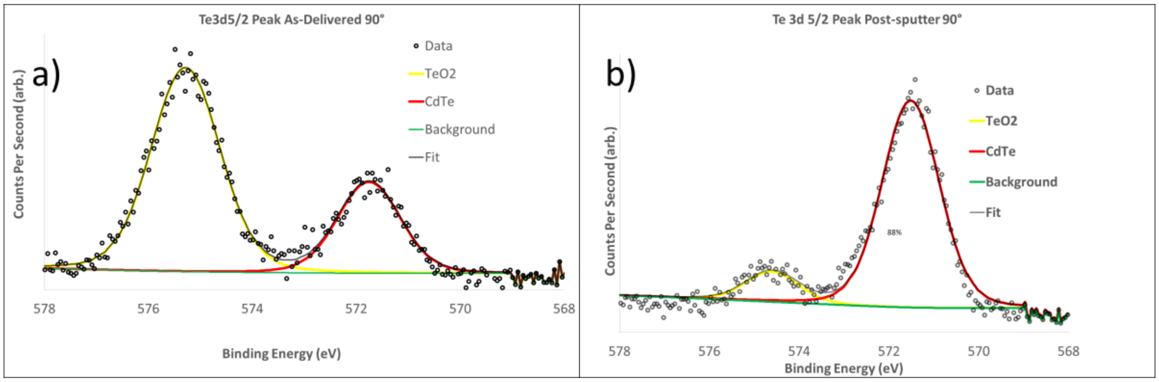

Figure 5.6. XPS of Te 3d5/2 peak of 4b07; a) as-delivered, showing Te from CdTe and TeO2, and b) after sputtering, showing removal of oxide overlayer of CdTe.

Angle-resolved XPS was used to examine the silicon 2p peak from both growth temperatures of samples 4B07 and 4B10 (Figure 5.7) grown at 75 and 150 °C, respectively. Two components were assigned to the peaks: Si 2p and Si^{4+} (this 4+ charge state is consistent with the formal oxidation state of Si present in the BTMSTe precursor). The Si 2p peak is assigned to the PE from the substrate, while the Si^{4+} peak is assigned to the ALD film contamination. At 15°, the Si^{4+} to Si 2p ratio is higher than at 90°, confirming the Si^{4+} peak is originating in the ALD film. After sputtering the surface of sample 4b07 grown at 75 °C, the substrate peaks at both angles become more prominent, consistent with etching of the CdTe ALD material and revealing more of the Si substrate. After sputtering of the surface of 4b10, the Si^{4+} peak becomes more prominent which could be explained by argon preferentially sputtering the CdTe component of the film compared to the Si^{4+} component.

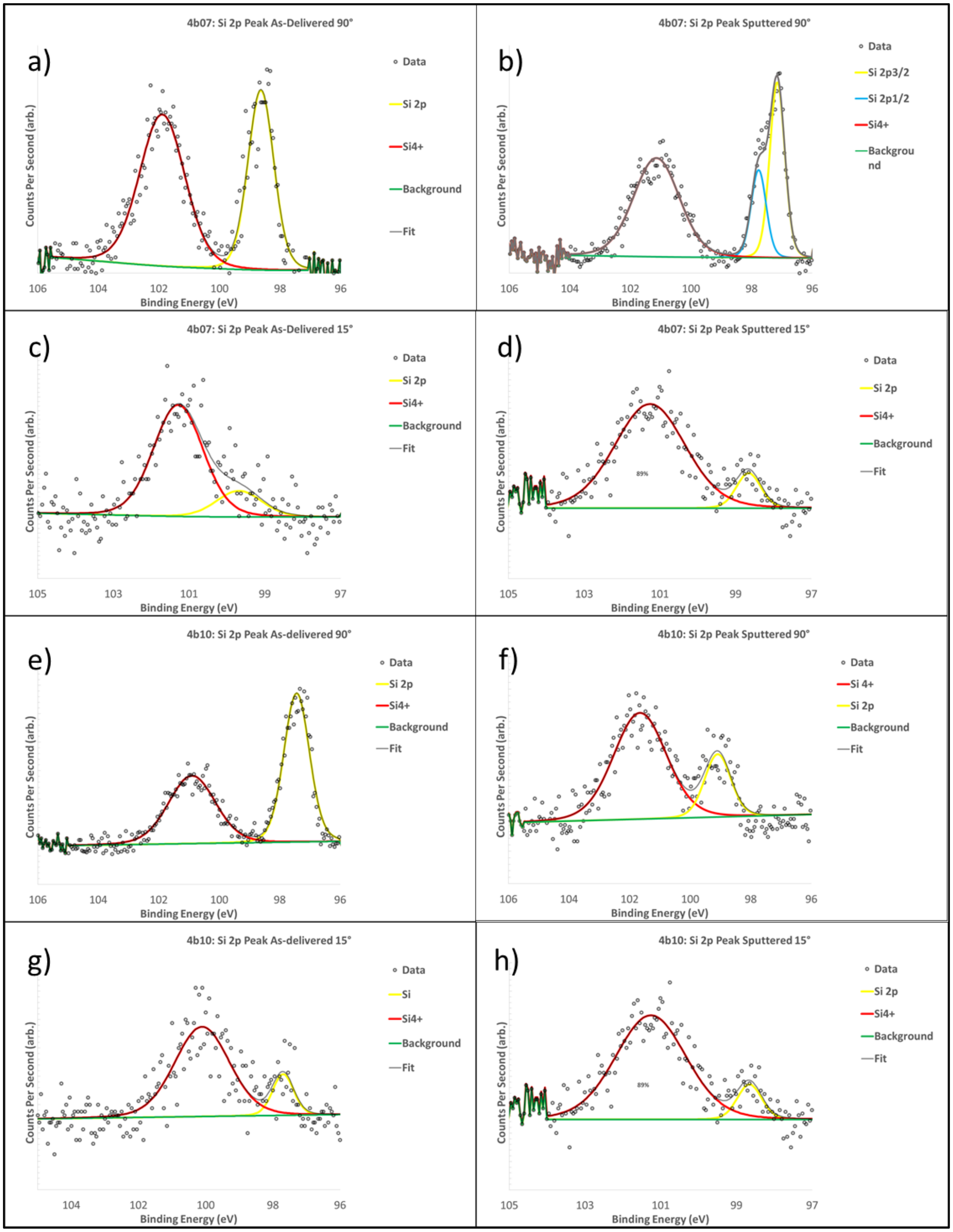

Figure 5.7. Angle-resolved XPS of the Si 2p peak from sample 4b07 (a-d) and 4b10 (e-h), as-delivered (left figures), after sputter (right figures), at 90° take-off-angle (a,b,e,f) and 15° (c, d, g, h).

5.3.5. XRD and TEM of ALD CdTe on MCT

A section of MCT sample B2 was sent to US Naval Research Lab in Washington, D.C. for high-brightness x-ray diffraction. XRD of sample B2 (growth onto MCT at 115 °C) is shown in Figure 5.8. The diffraction peak from the substrate has a much higher intensity than the ALD layer, as the ALD layer was much thinner. However, a shoulder on the low angle side of the substrate peak was observed and can be assigned to the lattice constant of CdTe (6.478 Å). Observing both (422) reflections from substrate and ALD layer indicates the ALD layer is epitaxial with the substrate.

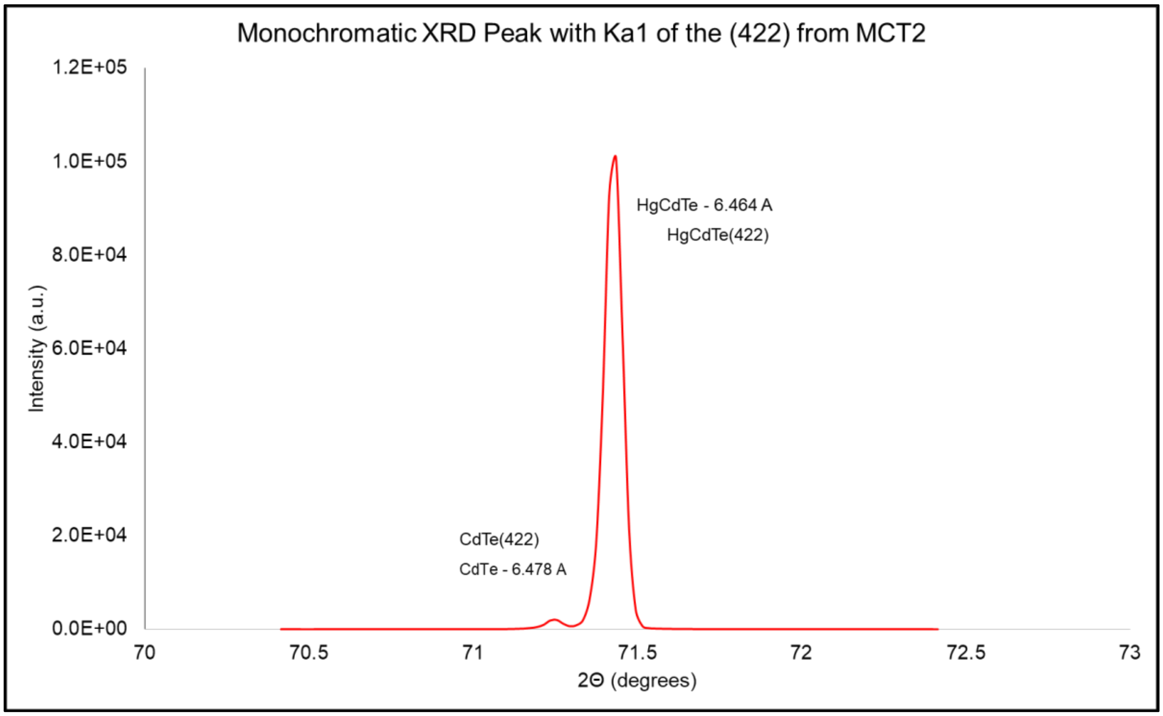

Figure 5.8. High-brightness monochromatic x-ray diffraction peak from sample B2: the strong peak is the (422) reflection from the MCT substrate, while the small intensity peak to the lower angle side is from the (422) reflection from the CdTe ALD layer.

A section of the same sample was sent to Evans Analytical Group (Raleigh, NC) for TEM investigation. Preparation of the TEM sample from MCT was difficult, but after many attempts was successful. As seen in Figure 5.9, TEM near the interface of the ALD layer with the substrate reveals that the ALD is epitaxial, yet rough and island-like in texture. An inverse Fast-Fourier transform of the TEM image was performed to reveal that the ALD layer was in registry with the substrate. A faint line at the interface indicates possibly a native oxide remained intact underneath the growing ALD film. The (211) orientation of the substrate can be seen, and extends into the ALD layer. Lattice spacing measurement of 3.7 Å is consistent with the <111> direction of CdTe.

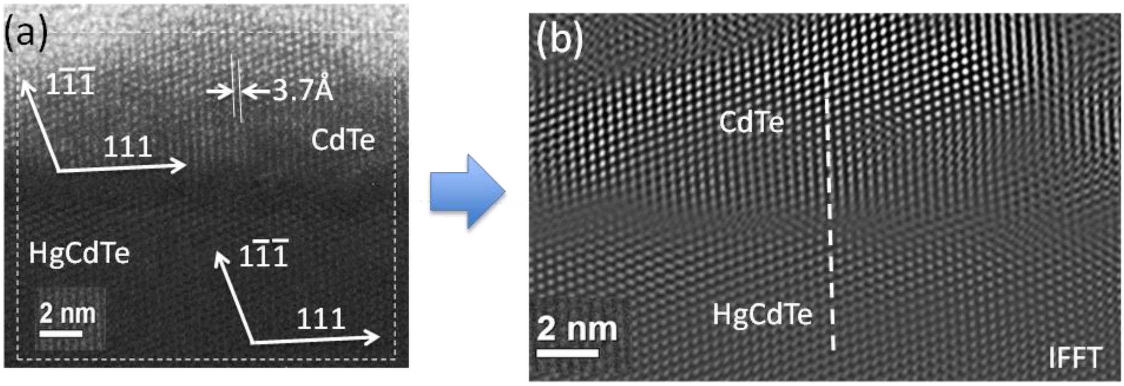

Figure 5.9. (a) HR-TEM from a lamella of CdTe deposited on MCT sample B2. A lattice spacing measurement indicates 3.7 Å. Equivalent crystal orientations are overlaid. (b) Inverse Fast-Fourier Transfer of the left TEM image. Dotted line highlights atomic registry between substrate and ALD layer.

5.4. Summary and Conclusions

Using BTMSTe as a Te ALD source was successful at deposition of CdTe onto both native oxide/Si and MCT surfaces as observed by SE, XPS, TEM, and XRD.

The GPC decreased with increasing substrate temperature. However, within a growth attempt at any single temperature, both the DMCd and the BTMSTe precursors demonstrated self-limited thickness increase. Meaning, pulsing of either Cd or Te precursor onto the substrate was observed to increase the thickness to a saturating value, and not increase the thickness with additional pulsing of the same precursor beyond this point.

The GPC decrease with increased substrate growth temperature could be due to deposition site de-activation and surface passivating due to the bulky silyl ligand chemistry of BTMSTe, as observed by other researchers,[74,76] in agreement with the use of other silyl ligand precursors used in selective-area ALD[77] which is detailed in the discussion section below and discussed in Chapter 3. GPC decrease due to reversible chemisorption, has been observed by other researchers using BTMSTe.[78,79] However in this work, no thickness decrease after pulsing BTMSTe was ever observed, consistent with irreversible chemisorption.

BTMSTe was successfully used as a substitute for DETe for CdTe ALD. Consistent with the growth method used in Chapter 4, an argon plasma step was necessary to promote growth. Unlike DETe, BTMSTe has some chemisorption site-deactivating nature which interferes with thermal growth and plasma growth by inhibiting chemisorption. For the growth temperature studies on silicon substrates, there appears to be a temperature dependence to the GPC, which could be due to increased chemisorption site de-activation/self-passivation by BTMSTe, consistent with previous researchers' observations.[74,79] Oxygen sites from the native oxide of Si may offer adventitious sites for silyl ligand chemisorption, consistent with the ligand exchange reactions proposed by Gwon, et al[48] who observe similar self-passivation and attribute to the pristine BTMSTe precursor. Process A uses the same Ar* decomposition of DMCd into Cd metal, so the expectation is that the Cd metal diffuses and nucleates in a similar fashion as the method used in Chapter 4 process (see Figure 5.10a-c). The different Te-precursor chemistry of Process A, with the silyl ligand, could lead to site deactivation through chemisorption of BMTSTe by dissociation on to the substrate (Figure 5.10d). Also, catalytic decomposition of BMTSTe on Cd metal sites results in formation of CdTe along with release of silyl ligands, which could then chemisorb onto the surface and deactivate chemisorption sites (Figure 5.10d and e).

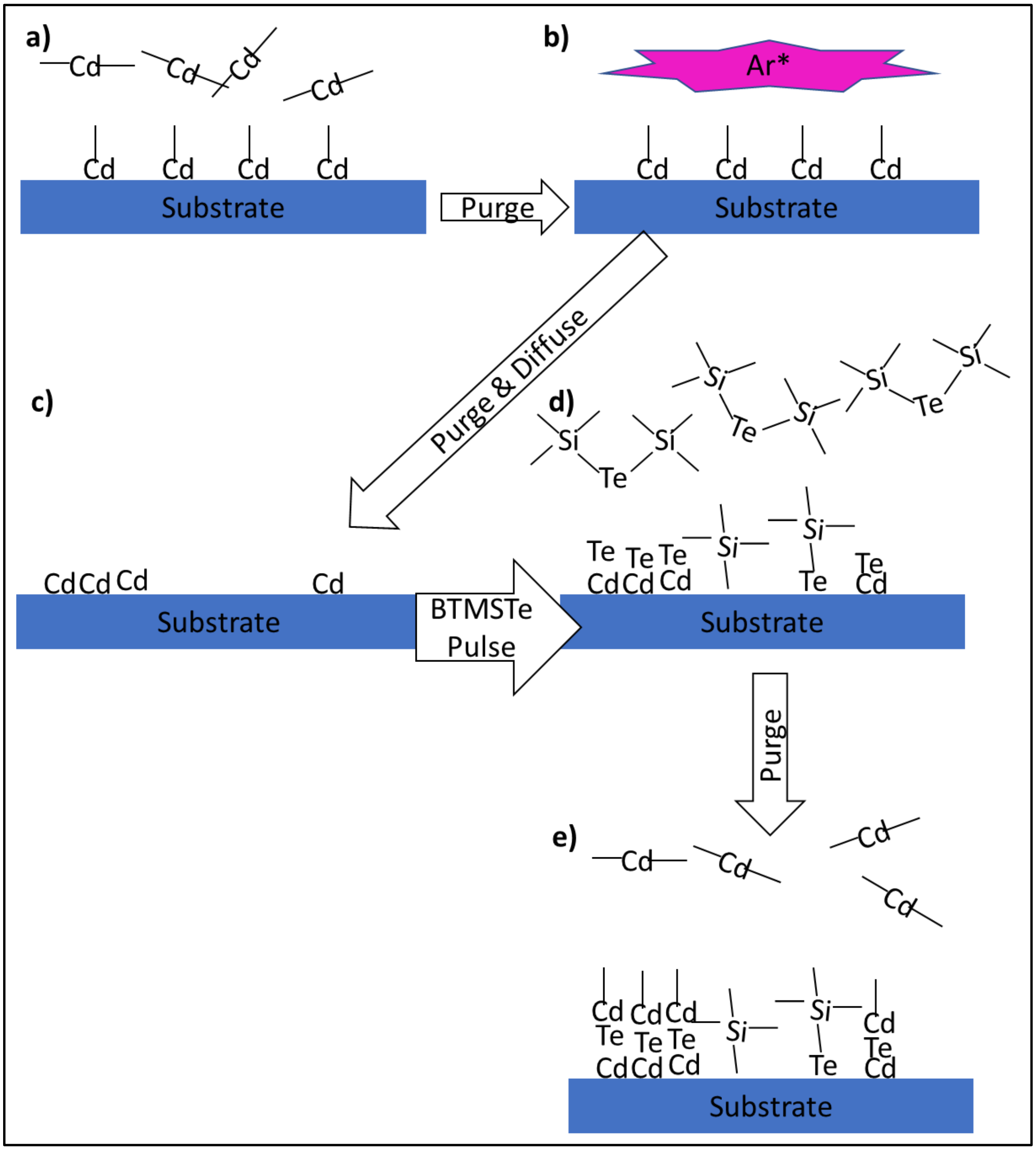

Figure 5.10. Proposed explanation of growth mechanism of Process A: a) DMCd pulse leads to chemisorption onto SiO_2 surface (substrate) followed by purging; b) Ar* exposure of DMCd and purge into c) Cd metal sites which diffuse and form islands, c) pulsing and purging of BTMSTe leads to either catalytic decomposition of BTMSTe into CdTe with release of silyl ligands, which either pump away, or chemisorb onto the surface, or chemisorption of BTMSTe onto bare SiO_2, again leading to site de-activation, followed finally by e) pulsing of DMCd, returning the surface to a) but with significant Si and C contamination.

This model could explain the lower temperature dependence of the GPC on MCT, where the TEM indicates an almost oxide-free starting surface, possibly due to the use of argon plasma to reduce the native oxide on MCT, which is not as stable as native oxides of Si; or possibly, the DMCd might have a reducing effect, as seen in TMA reduction of MCT native oxides.[80,81] Another mechanism could be that in contrast to the low surface energy of SiO_2, the surface of MCT at all deposition temperatures is that of a degenerate semiconductor, where the surface becomes metallic: this would provide for a high energy surface compared to SiO_2, more similar to that of Cd metal, lowering the contact angle between Cd metal and MCT surface, and suppressing diffusion of Cd.

XPS of the CdTe ALD film on silicon contains two oxides throughout: the native TeO_2 overlayer discussed previously, and an un-assigned peak from O 1s. This could correspond to SiO_2 in the ALD film, which would result from moisture contamination of the BTSMTe precursor, or oxidation of residual silyl groups upon exposure to air after ALD growth. Further experiments are needed to clarify the source of contamination from Si, C, and O. However, the ALD of CdTe using BTMSTe as the tellurium precursor was successfully enabled by use of plasma.

Chapter 6. Promoting Increased Growth-Per-Cycle in CdTe ALD by Solution-Phase Based Techniques

In an attempt to increase the GPC of the ALD Process A of Chapter 5, two strategies were investigated. The XPS of samples 4b07 and 4b10 from Chapter 5 revealed C, Si, and O contamination within the ALD films along with CdTe. The contamination is hypothesized to be from incomplete reaction or removal of the alkylsilyl ligands of BTMSTe, and motivated the following experiments. Removal of contamination could increase the number of active sites on the growing surface for ALD to occur, as the attempts at thermal ALD between DMCd and BTMSTe exhibited a surface site de-activation towards further growth.

Introduction of an additional co-reactant Acetyl Bromide (AcBr) was explored as inspired from wet chemical, solution-phase chemistry from previous researchers experimenting with either BTMSTe or DMCd,[82-84] and also as inspired from vapor-phase ALD experiments using *dehalosilylation* reactions (defined and reviewed below).[79,85,86] Dehalosilylation reactions in the ALD reactor could enable many new ALD film chemistries as discussed below. Incorporating AcBr as an additional precursor after the BTMSTe pulse/purge into Process A led to the increased GPC in Process B.

6.1. Acetyl Bromide Co-reactant

6.1.1. Dehalosilylation Reactions

Metal halides co-react with alkylsilyl ligand ($(CH_3)_3Si$-) bearing molecules in what is called the dehalosilylation reaction. Silane based ligands, such as alkylsilyls, are known as halophiles, or halide loving functional groups. Alkylsilyl ligand is a hard acid (strong acid), and BTMSTe is an example of a strong acid bonded to a soft (weak) base (Te^{2-}). Most metal halides (MX_y) are soft acids (M-) bonded to hard bases ($-X_y$). Reactions between these two pairs are promoted by what is call a hard-soft acid base exchange (HSAB), were the spontaneous reaction results from the hard-hard pairing of acids and bases along with the soft-soft pairing.[87] An example of a dehalosilylation reaction due to HSAB exchange include reacting tris(trimethylsilyl)arsine with GaX_2 to form Gallium Arsenide in solution:[85,86]

$$((\mathrm{CH_3})_3\mathrm{Si})_3\mathrm{As} + \mathrm{GaX_3} \rightarrow \mathrm{GaAs} + 3((\mathrm{CH_3})_3\mathrm{Si})\mathrm{X};\ \mathrm{X} = \mathrm{Cl}, \mathrm{Br} \qquad \textbf{6.1}$$

Previous ALD work using vapor-phase precursors has shown direct thermal co-reactivity between trichlorogermane $GeHCl_3$ and BTMSTe to deposit GeTe and form volatile trimethylsilyl chloride (TMSCl) and HCl. The elementary reaction sub-cycles are shown below, each as a dehalosilylation reaction:[78,79]

$$\mathrm{Sf} - \mathrm{Te}(\mathrm{Si}(\mathrm{CH_3})_3) + \mathrm{HGeCl_3} \rightarrow \mathrm{Sf} - \mathrm{TeGeCl_2} + ((\mathrm{CH_3})_3\mathrm{Si})\mathrm{Cl} + \mathrm{HCl} \qquad \textbf{6.2}$$

$$\mathrm{Sf} - \mathrm{TeGeHCl_2} + (\mathrm{Si}(\mathrm{CH_3})_3)_2\mathrm{Te} \rightarrow \mathrm{Sf} - \mathrm{TeGeTe} + 2((\mathrm{CH_3})_3\mathrm{Si})\mathrm{Cl} \qquad \textbf{6.3}$$

where Sf designates a surface active site, as in Chapter 2. These previous works demonstrate the feasibility of attempting dehalosilylation reactions in the vapor phase (and also that TMSCl doesn’t co-react and incorporate into the film).

6.2. PA-ALD with Acetyl Bromide Co-reactant

6.2.1. Process B

AcBr was incorporated into the plasma-assisted Process A after the BTMSTe sub-cycle, in an attempt to improve GPC when the DMCd was first decomposed by argon plasma. Thus, the second process (Process B) introduced acetyl bromide as a fourth sub-cycle. This recipe consisted of 1) exposing pulses of DMCd onto the growth surface, 2) purging of excess DMCd and by-products from the chamber, 3) argon plasma exposure to the surface, 4) purging plasma exposure by-products, 5) exposing pulses of BTMSTe to the surface, 6) purging of excess BTMSTe and by-products from the chamber, 7) exposing pulses of AcBr to the surface, and 8) purging excess AcBr and by-products from the chamber. (Removing the plasma sub-cycle from Recipe B also resulted in an initial thickness increase and then no additional increase was observed, regardless of the number or duration of additional DMCd or BTMSTe pulses.) Process B elementary equations are hypothesized to consist of the following, with equation 6.6 and **Error! Reference source not found.** as a parallel, competing pathways to CdTe formation:

$$\mathrm{Sf} + \mathrm{Cd(CH_3)_2} \rightarrow \mathrm{Sf} - \mathrm{CdCH_3} + {}^{\bullet}\mathrm{CH_3} \tag{6.4}$$

$$\mathrm{Sf} - \mathrm{CdCH_3} \xrightarrow{Ar*} \mathrm{Sf} - \mathrm{Cd} + {}^{\bullet}\mathrm{CH_3} \tag{6.5}$$

$$\mathrm{Sf} - \mathrm{Cd} + \mathrm{(Si(CH_3)_3)_2Te} \rightarrow \mathrm{Sf} - \mathrm{CdTe} + {}^{\bullet}\,2\mathrm{Si(CH_3)_3} \tag{6.6}$$

$$\mathrm{Sf} - \mathrm{Cd} + \mathrm{(Si(CH_3)_3)_2Te} \rightarrow \mathrm{Sf} - \mathrm{CdTe{-}Si(CH_3)_3} \tag{6.7}$$

$$\mathrm{Sf} - \mathrm{CdTe{-}Si(CH_3)_3} + \mathrm{(CH_3)COBr} \rightarrow \mathrm{Sf} - \mathrm{CdTeCO(CH_3)} + \mathrm{((CH_3)_3Si)Br} \tag{6.8}$$

$$\mathrm{Sf} - \mathrm{CdTeCO(CH_3)} + \mathrm{Cd(CH_3)_2} \rightarrow \mathrm{Sf} - \mathrm{CdTeCdCH_3} + \mathrm{(CH_3)_2O} \tag{6.9}$$

These elementary reactions are illustrated in **Error! Reference source not found.**.

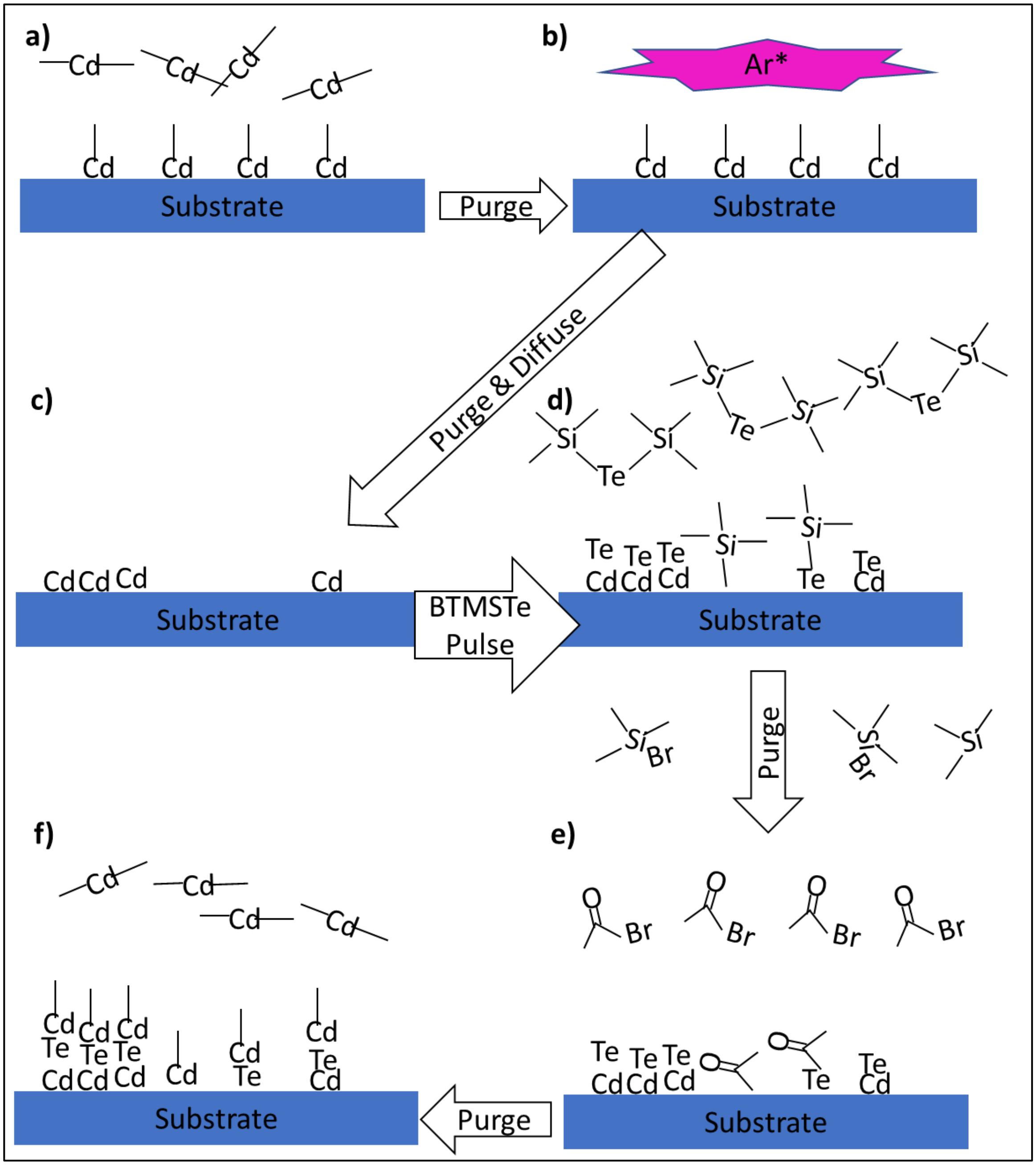

Figure 6.1. Elementary reactions of Process B: a) DMCd pulse (Equation *6.4*), b) argon plasma exposure (Equation *6.5*), c) Cd-terminated surface, d) BTMSTe pulse indicating incomplete catalytic removal of silyl ligand (Equations *6.6* and *6.7*) leading to site blocking, e) AcBr pulse ligand exchange, converting any silyl groups present to acetyl ligands (Equation *6.8*Error! Reference source not found.), and f) DMCd pulse, returning the s urface to condition a) (Equation *6.9*).

6.3. Attempts at Thermal CdTe ALD

Cadmium Bromide ($CdBr_2$) would also undergo dehalosilylation reactions with BTMSTe. However, $CdBr_2$ does not have appreciable vapor pressure (~150 mTorr at 300 °C[88]) to be a practical ALD precursor for cadmium telluride. In-situ formation of surface adsorbed $CdBr_2$ (Sf-CdBr, where the Cd is bonded to the surface site and has a single bond to Br) was attempted in the ALD reactor by first pulsing DMCd onto the substrate, purging, then pulsing AcBr and purging, in an attempt to react chemisorbed DMCd to produce $CdBr_2$ and acetone ($(CH_3)_2O$) as products (Equation *6.10*). Then the Cd-Br could undergo dehalosilylation to deposit CdTe and form volatile trimethylsilylbromide (Equation *6.11*):

$$\mathrm{Sf-CdCH_3 + AcBr \rightarrow Sf-CdBr + (CH_3)_2O} \qquad \textbf{6.10}$$

$$\mathrm{Sf-CdBr + (Si(CH_3)_3)_2Te \rightarrow Sf-CdTe-(Si(CH_3)_3) + ((CH_3)_3Si)Br} \qquad \textbf{6.11}$$

AcBr was used as a co-reactant in an attempt to remove the silyl ligand from the chemisorbed BTMSTe, and replace with a more reactive ligand, or to remove the ligand completely. The reaction of BTMSTe with acyl halides (e.g. AcBr) in the solution phase (Equation *6.12*) has been demonstrated to remove the silyl ligand, and form diacetyl telluride intermediate [84].

$$\mathrm{((CH_3)_3Si)_2Te + 2(CH_3CO)Cl \rightarrow 2(CH_3)_3SiCl + (CH_3CO)_2Te} \qquad \textbf{6.12}$$

In-situ SE indicated a reaction between the chemisorbed BTMSTe and the AcBr at 75 °C and is shown below in Figure 6.2 as evidenced from increased GPC of Process B when pulsing AcBr after BTMSTe, not before. If the silyl ligand could be exchanged with an acetyl ligand, this would promote reaction with DMCd. DMCd can ligand exchange with acetyl-bearing molecules in solution phase, hence this was attempted in the vapor phase. Before the advent of Grignard reagents used in organic chemistry to form carbon-carbon bonds, DMCd was used to form C-C bonds by reaction with acyl halides in solution, resulting in ketone and CdX_2 as products[82,83], where X=F, Cl, Br or I.

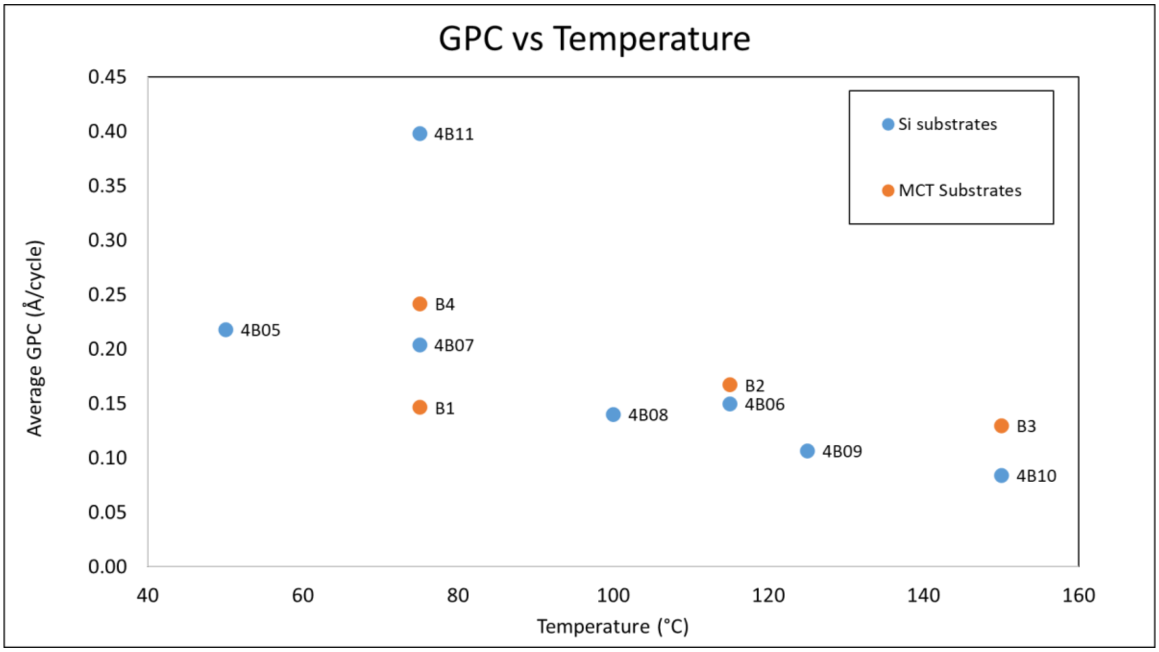

Figure 6.2. Temperature dependence of growth-per-cycle of ALD of CdTe on Si and MCT substrates using Process B, along with Process A samples from Chapter 5. Process B samples were 4B11 (on silicon) and B4 (on MCT).

For the attempt at thermal ALD, AcBr was pulsed to react with DMCd exposed surfaces in an effort to form CdBr2 for further dehalosilinization by BTMSTe. In-situ SE did not indicate any change in apparent thickness upon introducing AcBr as an addition sub-cycle after the DMCd sub-cycle and before the Te sub-cycle, indicating no reaction was taking place without the plasma step, and therefore in-situ formation of CdBr2 was abandoned.

6.4. Growth and Film Characterization

Process B was used to deposit 250 cycles of CdTe ALD onto Si and 500 cycles onto MCT substrates at 75 °C using the developed ALD parameters in Table 6.1, where the AcBr sub-cycle is inserted following the BTMSTe pulse and purge. The AcBr was developed by finding the minimal precursor pulse required to saturate the GPC.

Table 6.1. Developed ALD parameters based on depositions onto silicon substrates.

DMCd multi-pulse	DMCd multi-pulse purge	DMCd purge	Plasma Power	Plasma exposure time	Plasma purge	BTMSTe pulse	BTMSTe purge	AcBr pulse	AcBr purge
0.025 s	0.5 s	10 s	250 W	15 s	15 s	0.1 s	30 s	0.1	10 s

Table 6.2. Substrate, growth temperature, number of cycles, and SE-derived thickness and growth-per-cycle using Process B.

Sample	Substrate	Temperature (°C)	# of cycles	Thickness (Å)	GPC (Å/cycle)
4B11	Si	75	250	100	0.4
B4	MCT	75	500	120	0.24

GPC vs. temperature data is plotted in Figure 6.3 for a comparison of Process B (4B11 and B4) against Process A including growth on both Si and MCT substrates. The overall GPC is higher for Process B (see Table 6.2), which indicates the acetyl bromide was co-reacting with the silyl ligand of BTMSTe to produce silyl bromide and acetyl telluride, as shown in Equation *6.11*.

In-situ SE for growth on Si at 75 °C in Figure 6.3 and Figure 6.4 compares Process A (sample 4B07) against Process B (sample 4B11). The ALD film was again characterized using a Cauchy model, as presented in Chapters 4 and 5. Process A has an initial GPC higher than Process B, although at a later time, decreases to lower than Process B (Figure 6.3). This could be due to a large initial chemisorption of silyl ligands onto the surface, blocking further growth sites. Introduction of AcBr in Process B could remove the silyl ligands on the surface, reducing the initial large GPC (see Figure 6.4), while then maintaining a higher GPC throughout the growth by elimination of site-blocking silyl ligands (see Equation *6.11* and Figure 6.1e).

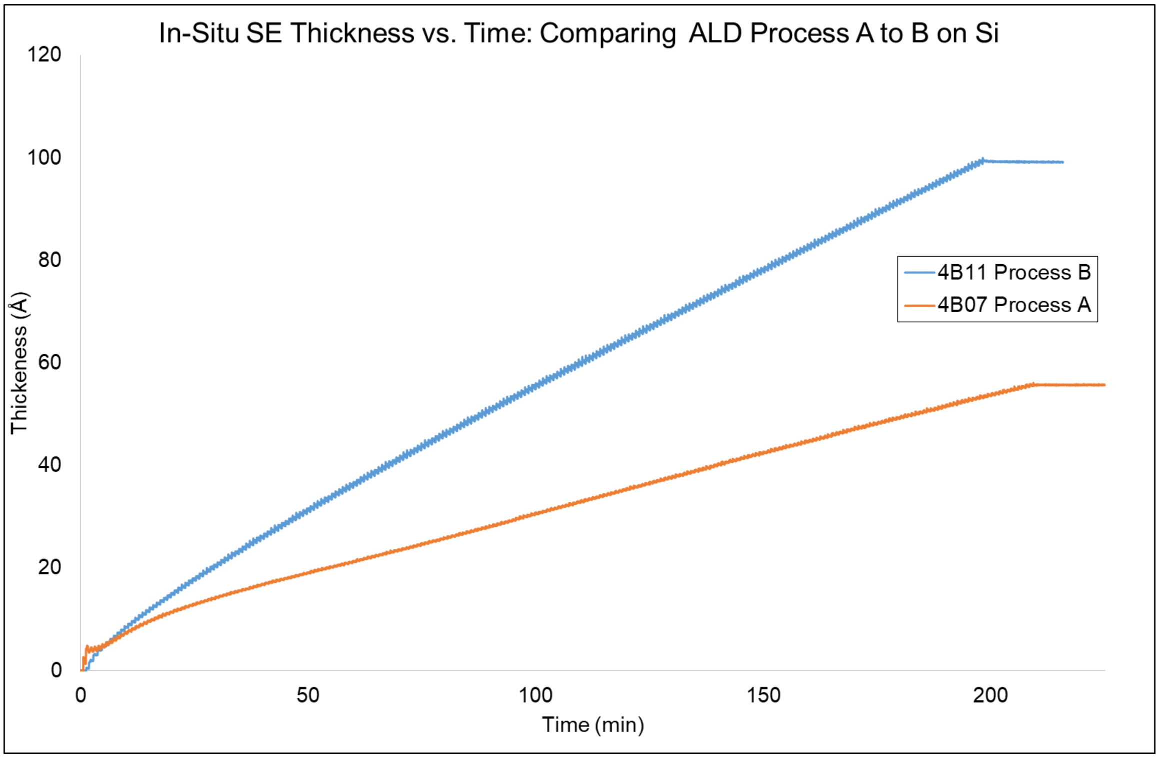

Figure 6.3. Comparing in-situ SE of 4B11 (Process B) to 4B07 (Process A) CdTe ALD onto Si substrates at 75 °C.

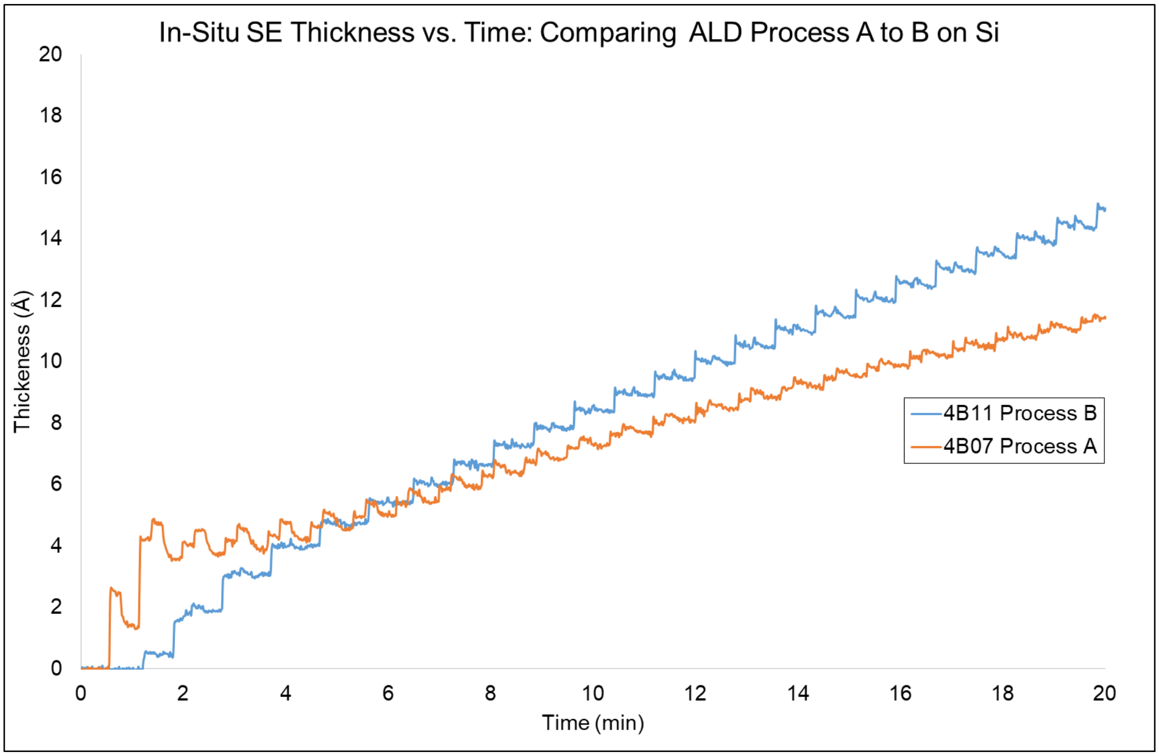

Figure 6.4. Zoom in of Figure 6.3 showing initial ALD growth.

Similarly, in-situ SE for growth on MCT at 75 °C in Figure 6.5 and Figure 6.6 compares Process A (sample B1) to B (sample B4). The ALD film was characterized using a Cauchy model, while the MCT substrate, fully absorbing across the spectrum of the ellipsometer, was modelled using a B-spline, which allowed for extraction of tabulated values of n and k while maintaining physically real solutions to the optical constants.[89] Again, the in-situ SE has a large, initial thickness increase in Process A that is suppressed in Process B which has a higher GPC later in the growth (Figure 6.5), indicating that the growth mechanism on Si and MCT are very similar, namely, that the introduction of AcBr in Process B improves silyl ligand elimination from the growing film during growth initiation and possibly throughout growth (Figure 6.6).

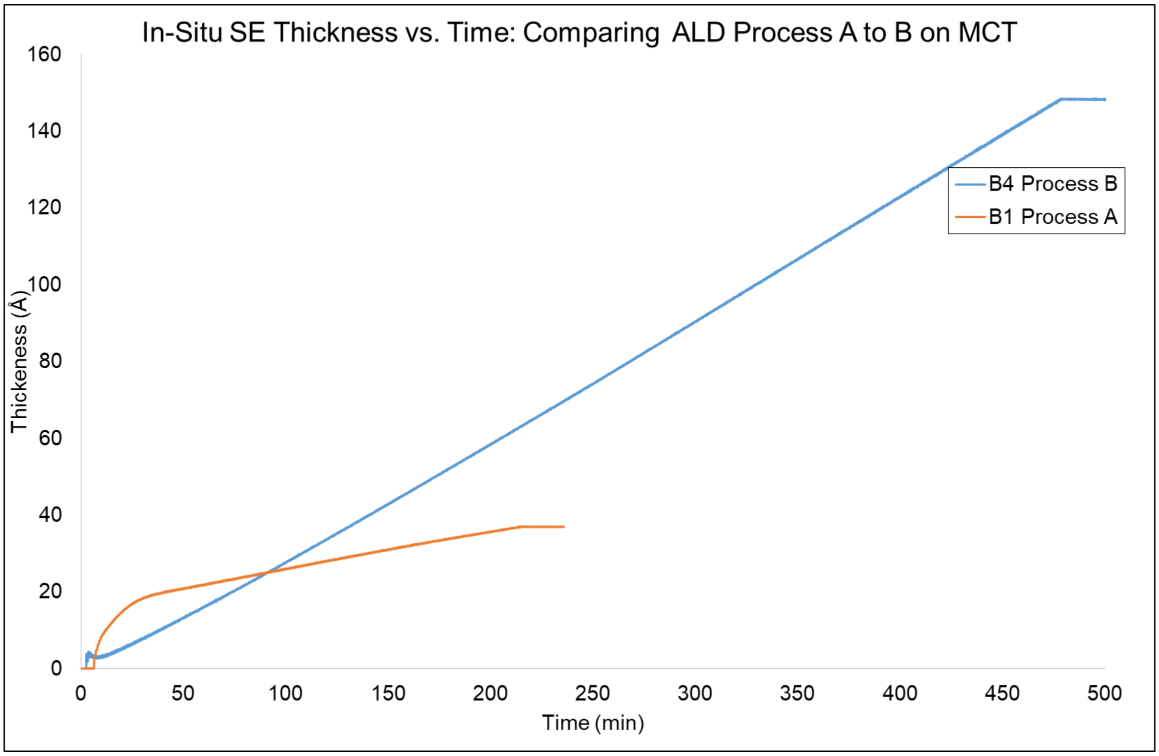

Figure 6.5. Comparing in-situ SE of B4 (Process B) to B1 (Process A) CdTe ALD onto MCT substrates at 75 °C. Note B4 had 500 cycles while B1 had 250 cycles of CdTe ALD.

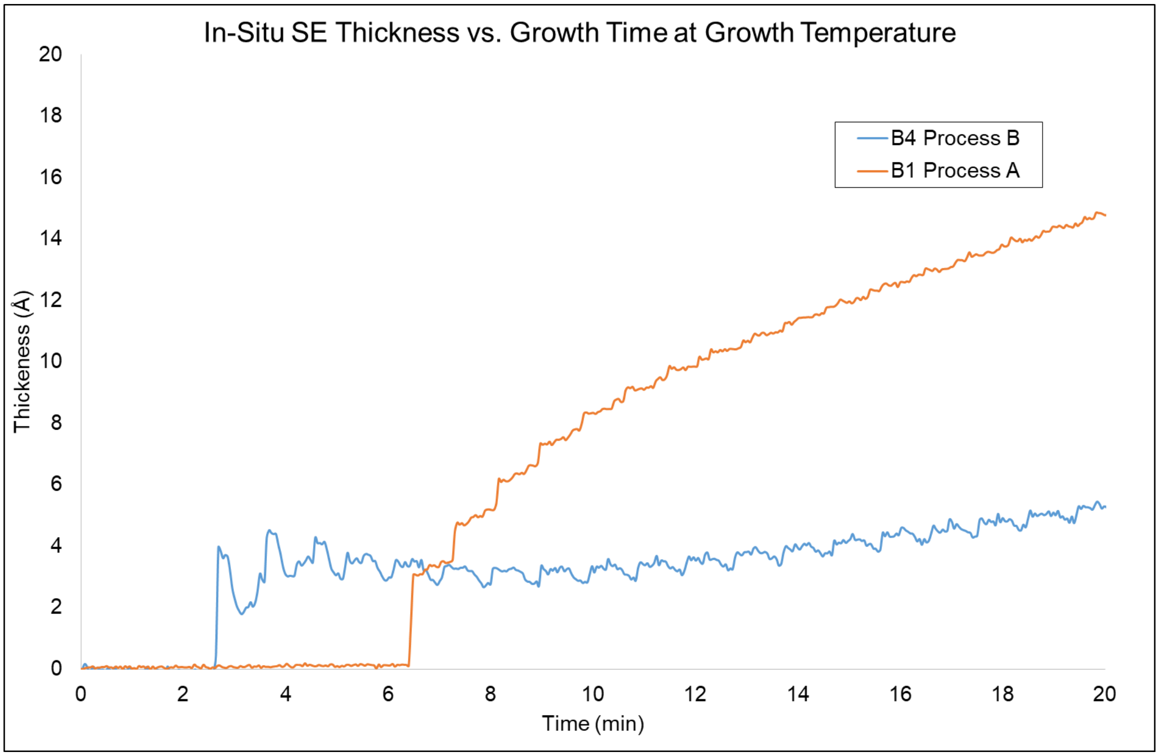

Figure 6.6. Zoom in of Figure 6.5 showing initial ALD growth. Note the slight decrease in apparent thickness of B4 and the large initial increase in thickness of B1. Note that there is an offset of a few minutes of the start of growth in either case, resulting in initiation of growth at different times.

XPS of the Process B depositions onto Si demonstrates CdTe is present, along with Si, C, O, and Br contamination. Sample 4B11 was examined as delivered, argon sputtered for 30 seconds at 3 kV, then for 2 minutes, and again for 2 minutes, and examining after each sputter duration. Atomic concentrations were calculated from survey spectra, and shown in Table 6.3. Compared to Table 5.2 for the at% calculated for sample 4B07, grown at the same temperature as 4B11 (75 °C) but using Process A, Process B shows similar contamination levels of Si, C, and O but with additional Br contamination not present in Process A.

Table 6.3. Relative atomic concentration in % of the surfaces of samples 4B11, as quantified by survey spectra from 90° and 15° take-off angle from sample surface plane.

	Total Sputter Time (min)	**Cd**	**Te**	**O**	**C**	**Si**	**Br**
90°	0	18	13	18	38	10	3
	0.5	21	17	17	29	13	3
	2.5	22	18	14	30	13	3
	4.5	21	19	14	27	17	3
15°	0	32	21	8	4	21	13
	0.5	22	15	9	4	28	22
	2.5	28	15	13	3	22	19
	4.5	27	13	17	2	22	19

TEM images were collected at Arizona State University using a JEOL ARM200F AC-STEM. TEM cross sections of 250 cycles of Process B onto silicon substrates are shown in Figure 6.7, Figure 6.8, and Figure 6.9. Again, lattice spacing measurements demonstrate the films are CdTe. Also, like Process A, TEM indicates CdTe ALD proceeds by island nucleation, rather than LBL. Also, an amorphous matrix of unknown composition can be observed in which the CdTe islands are imbedded.

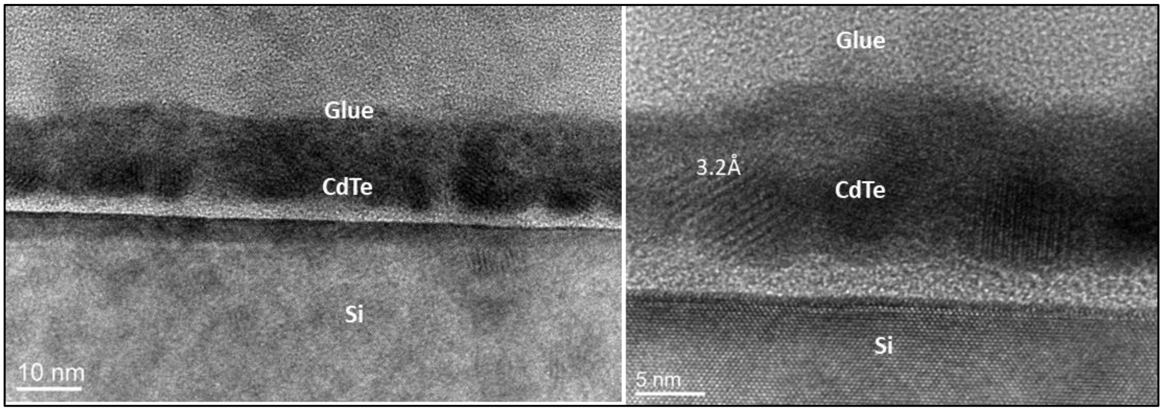

Figure 6.7. Cross-sectional BF TEM (left) and HRTEM (right) images of sample 4B11, showing higher nucleation density than 4B07 (Process A). Note the island-like growth of CdTe on top of the amorphous SiO_2.

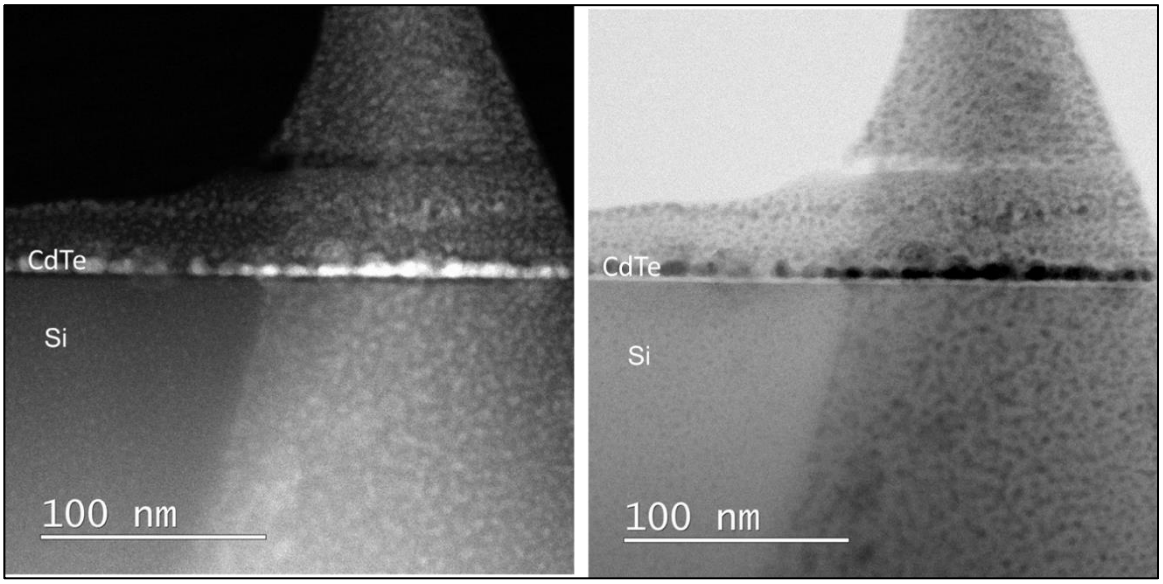

Figure 6.8. HAADF image (left) and BF STEM image (right) of 250 cycles of Process B onto Si substrate, showing the island-like growth of the CdTe, Si substrate and silicon oxide interface.

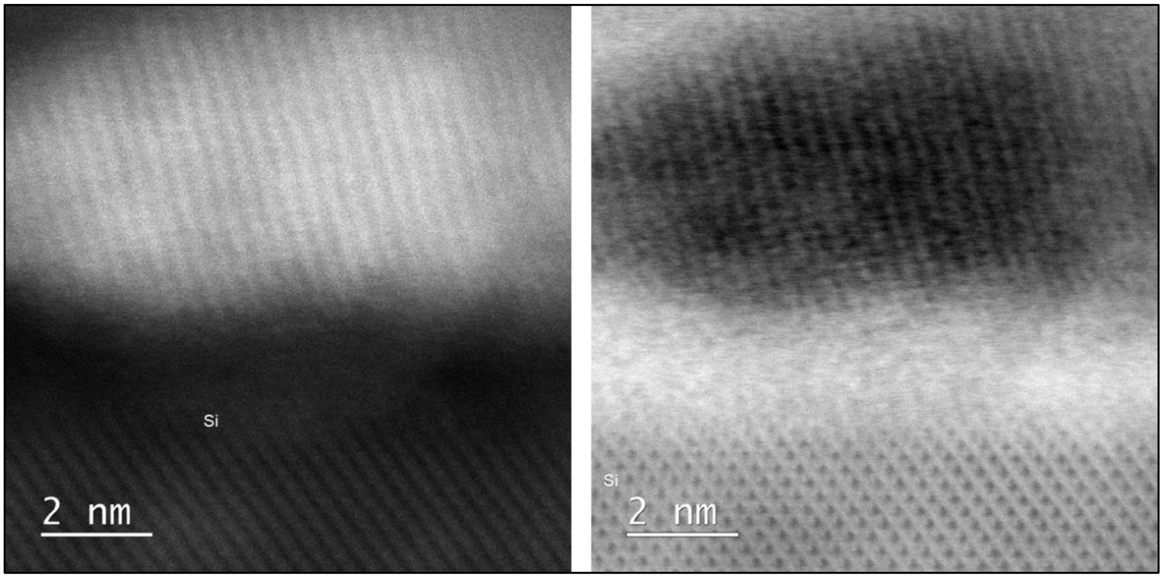

Figure 6.9. HAADF TEM (left) and BF STEM (right) images of 250 cycles of Process B onto Si substrate, showing crystalline substrate, amorphous native oxide, and crystalline CdTe film with island growth.

6.5. Conclusion

AcBr used in Process B increased the GPC on both Si and MCT substrates over Process A, but had Br contamination in addition to the Si and C contaminants in Chapter 5. Plasma was necessary to promote the decomposition of DMCd into Cd, to catalytically decompose BMTSTe and react to form CdTe, while direct thermal co-reaction of DMCd, AcBr and BTMSTe was unsuccessful. Several elementary reactions were proposed to explain the differences between Processes A and B: catalyzed decomposition of BTMSTe into CdTe after chemisorption onto the Cd-metal site is in competition with incomplete removal of silyl ligands on Te surface sites. Further optimization of the process is left for future work.

Chapter 7. Characterization of CdTe ALD Passivation by Photoconductive Decay Measurements

7.1. Carrier Recombination in MCT

The effectiveness of the surface passivation by CdTe ALD onto the surface of MCT can be quantified through PCD measurement, a technique used to study bulk and surface recombination lifetimes in semiconductors. Photoconductive decay is the process by which excited electron hole pairs in a semiconductor decay back to ground states and is a time dependent process. The minority carrier recombination rate, and hence the minority carrier lifetime can be extracted from PCD measurements. Samples with various treatments (untreated, annealed, and/or passivated by ALD) were measured by PCD. One set of samples were measured at 77 K, while another set was measured from 77 K to 295 K. The first set at a single temperature explored the effects of annealing in combination with CdTe ALD passivation on the lifetime of both annealed and unannealed MCT, and compared against the theoretical maximum lifetime at 77K. The second set of lifetime measurements as a function of temperature was compared against the theoretical maximum lifetime vs temperature which enabled extraction of the SRH recombination parameters, which is useful for comparing additional future ALD experiments not included in this dissertation. The measurements demonstrate that passivation by CdTe ALD is effective and increased the lifetime over the untreated and/or annealed samples.

Measuring the lifetime of the sample versus temperature allows parameterization and extraction of E_t, the trap level measured in proportion to the band gap (i.e., E_g=1), (Equation *3.28*) τ_{n0} (Equation *3.26*) and τ_{p0} (Equation

3.27).[57,58] By fitting the experimental data to the above expressions for recombination lifetimes, it is possible to show how the SRH lifetime improves, indicating that passivation by CdTe was effective. Also, extraction of the parameters allows insight into where the effective defect level lies relative to the bandgap (i.e., surface recombination and bulk recombination levels), quantification of the product of their capture cross-section and trap density (Equations *3.26* and *3.27*), and how that changes upon treatment or processing. The more important conclusion (regarding this research) is that surface recombination was significant, and that passivation was necessary and an effective process to improve lifetime.

However, it is also possible to extract the τ_{SRH} at a single temperature if measuring at low temperature (in the extrinsic region) and both the doping and composition are known. Then the effectiveness of surface passivation can be evaluated without the need for temperature variation during measurement. However quantification of E_t, τ_{n0}, and τ_{p0} is not possible to uniquely solve without measuring lifetime at several temperatures from the extrinsic to intrinsic regions (i.e., 77 K to 300 K).

7.2. Experimental Details

In this chapter, four samples from the same MCT wafer grown by MBE at the US Army Research Laboratory are compared after specific treatments to study the effectiveness of surface passivation by CdTe ALD: 1) the baseline unannealed, unpassivated sample, 2) annealed, unpassivated sample, 3) unannealed, passivated sample, and 4) annealed, passivated sample. Studying the effect of annealing on the lifetime was necessary because as-grown, unannealed MCT has Hg vacancy densities which act as SRH recombination center and lower the τ_{SRH}. Comparing the effect of annealing and passivation on lifetime can reveal the magnitude of effect of each treatment independent of the other.

PCD curves were measured at 77 K as detailed in Chapter 3. The samples are nominally identical in doping, x-value, and starting Hg vacancy concentration because they come from the same wafer. The unannealed, unpassivated sample is the baseline and is compared against the other three experiments. Even without quantitatively comparing the τ_{SRH} of each sample, any increase in lifetime over that of the baseline would be evidence that the process (i.e., annealing or passivation) improves the lifetime.

Additionally, two other samples' PCD versus temperature were measured, as detailed in Chapter 3, to extract the SRH parameters by fitting the temperature dependence of the PCD lifetimes.

7.3. Results and Discussion

Six 1 x 1 cm samples of MCT were prepared from the same wafer. The nominal material parameters were MBE grown n-type MCT on cadmium zinc telluride (CZT) substrates with (111) orientation, doping levels ~1e15 cm^{-3}, 15 um thick. The samples were chosen to be as close in location from the same wafer as practical to minimize variation in doping and composition. All samples received identical wet etch treatments by 0.5% v/v bromine in ethylene glycol to remove ~1 μm and blown dry by N_2 to create the same surface starting conditions. One sample (sample A) was then measured as-delivered from the etch batch. Another had 2000 cycles of CdTe deposited by ALD at 80 °C using Process B described in Chapter 6 (sample B) at the same time as sample D (described next).

The other two samples were annealed under Hg overpressure in a sealed quartz ampoule (samples C and D). The ampoule, plug, and crucible were first cleaned by light HF acid etch, followed by a “flame-off”: placing the plug and crucible into the ampoule, attaching to a vacuum pumping station, pumping to high-vacuum, and heating the entire surface of the ampoule until red-hot using an oxygen-hydrogen torch to remove impurities from the quartz. The quartz was allowed to cool and removed from the vacuum station. Then Hg was placed into the quartz crucible at the back, the samples were placed into the ampoule, and then back onto the pumping station and pumped out to $<10^{-6}$ Torr using sorption pumps, at which point the ampoule was sealed using an oxygen-hydrogen torch. The entire ensemble was then placed into a clamshell furnace and annealed at 425 °C for four hours, followed by 20 hours at 250 °C.

After annealing, one of the annealed samples had 2000 cycles of CdTe deposited during the same ALD run as sample B (sample D). Each sample was measured in the PCD experiment at 77 K for comparison. The PCD curves are plotted in Figure 7.1 where the voltage output has been normalized against the peak values.

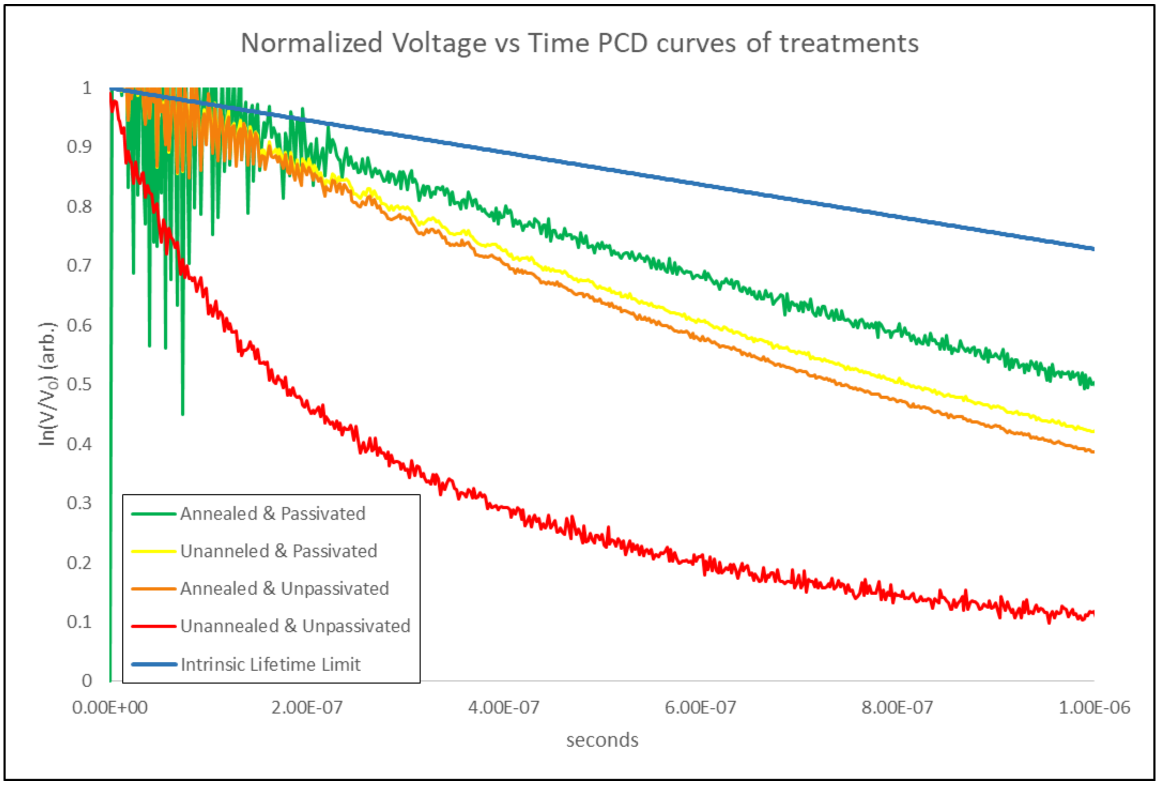

Figure 7.1. Photoconductive decay curves at 77K of Samples A, B, C, and D compared against the intrinsic lifetime limit of an ideal MCT sample of composition x=0.28 and doping 1 x 10^{15} cm^{-3}.

The PCD time and lifetime increases in the series A, C, B, & D as shown in Table 7.1. The magnitude of change in lifetime compared to the baseline indicates passivation has a larger magnitude of effect as compared to anneal. Both, anneal and passivation, have the largest increase in lifetime over baseline. Therefore, passivation by CdTe ALD increases lifetime in the MCT samples.

Table 7.1. List of samples, their treatments, and effective minority carrier lifetime.

Sample	Annealed?	Passivated?	τeff (ns)
A	no	no	779
B	no	yes	980
C	yes	no	900
D	yes	yes	1080

Intrinsic Limit			3960

The final two samples were characterized by PCD as a function of temperature. Due to time constraints, only two samples were measured and compared: as-delivered with a wet etch as above (sample E), and a sister sample that was wet etched then 2000 cycles of CdTe ALD as above (sample F). Again, CdTe ALD passivation increases the lifetime of the sample as compared to the as-delivered as shown in Figure 7.2. Using the nominal composition of x=0.28 and doping 1 x 10^{15} cm^{-3} as fixed variables, the τ_p, τ_n, and E_t were used as fitting parameters. A custom Labview Levenburg-Marquardt Least Squares algorithm was used to optimize the fit. The extracted values are shown in TABLE 7.2 SRH Parameters. Figure 7.3 is a plot of the discrete points of measured PCD lifetime values versus 1000/T. Also plotted are the Auger, radiative, SRH, and total lifetime as calculated using Equations *3.23*, *3.21*, *3.25*, and *3.20*, respectively; these are included to illustrate what the intrinsic limit of the ideal material would be in the absence of any SRH contributions from bulk or surface defects. As can be seen from Figure 7.2, the lifetime of the ALD passivated sample is higher than the unpassivated sample throughout the extrinsic region where SRH recombination dominates (77 K to ~230 K), demonstrating that the improvement by CdTe ALD passivation was significant and successful. Also, as shown in Table 7.2 the SRH hole lifetime (t_{p0}) was significantly higher in the ALD passivated sample, again confirming CdTe ALD passivation was successful.

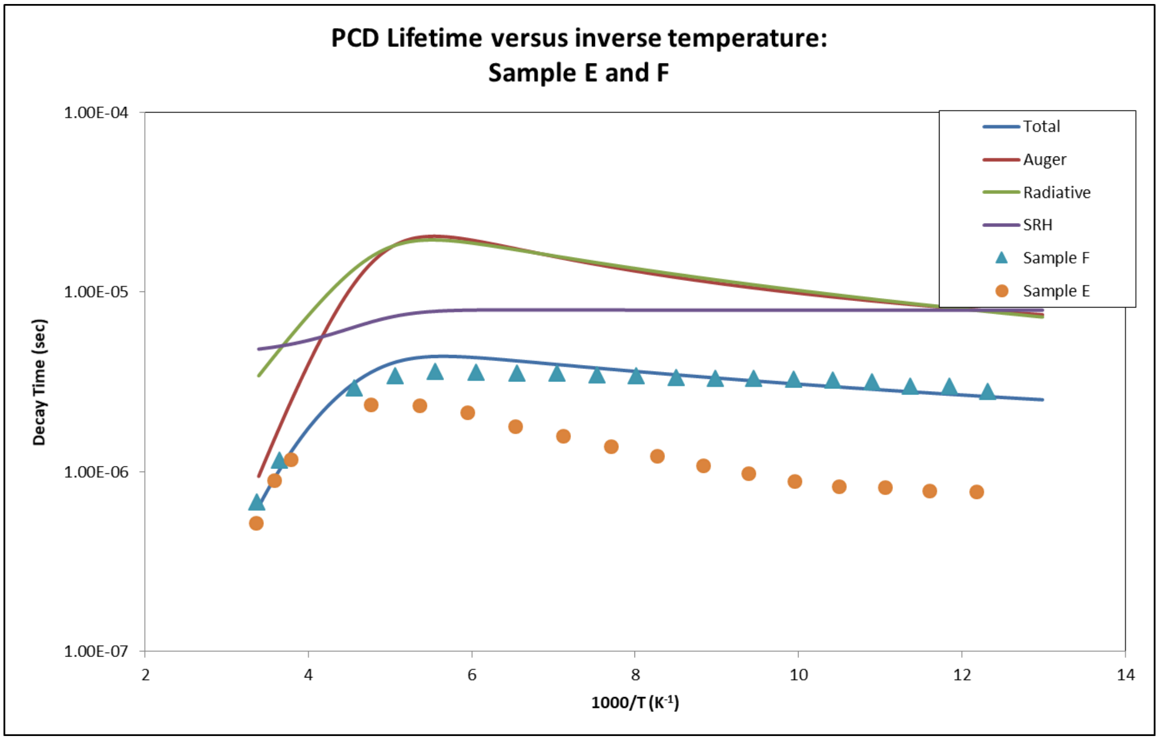

Figure 7.2. PCD time versus 1000/T of samples E and F. Data fit to modelled Equation *3.20* using least-squares algorithm using E_t, t_{n0}, and t_{p0} for both E and F as fitting parameters.

Table 7.2. SRH Parameters.

SRH Parameters	**Etch**	**Etch+ALD**
Et (vs. Eg)	0.82	0.5
tn0 (s)	1E-08	1E-08
tp0 (s)	1.00E-06	7.94E-06

7.4. Conclusion

PCD experiment is a quantitative measure of the minority carrier recombination lifetime in semiconductors and it was applied here to MCT. Passivation by CdTe ALD sample C was effective in increasing the lifetime compared to baseline samples. Annealing increased the lifetime compared to a baseline sample. Passivation combined with annealing increased the lifetime even higher compared to the baseline. Passivation had the largest magnitude of effect compared to annealing. PA-ALD CdTe passivation was shown to be effective on MBE grown MCT.

Sample F passivated by Process B did not reach the intrinsic limit. However, for future work, the author will optimize all the efforts here to increase the lifetime to the intrinsic limit. The PA-ALD CdTe process is expected to have a large impact on current and next generation MCT devices. Incorporation of the ALD process into full device fabrication is warranted based on these preliminary but very exciting results. In parallel, future work on the process development is discussed in Chapter 8, and some very simple, testable experiments are outlined and will be examined with the characterization techniques used to explain the observations presented in this thesis. New samples must be further characterized by PCD experiments because the SRH lifetime of any passivation process is the real required parameter to optimize for all practical application of CdTe ALD passivation.

Chapter 8. Summary and Future Work

8.1. Summary

Low-temperature ALD of CdTe was investigated and achieved in this dissertation. Innovative plasma assisted decomposition of DMCd was demonstrated. Growth of CdTe by ALD was demonstrated by first exposing growth substrates to DMCd, then Ar plasma to decompose the DMCd into Cd metal, then exposure to either DETe (see Chapter 4), BTMSTe (see Chapter 5), or BTMSTe followed by exposure to AcBr (see Chapter 6). Mechanisms of ALD were proposed and supported by characterization and observation. A variety of surface chemistries were explored. New hypotheses for thermal CdTe were created for investigation in the future. A CdTe ALD process was transferred to MCT to successfully demonstrate increased minority carrier lifetime by PCD. More work and success with CdTe ALD is to come, and will transfer into existing domestic MCT factories.

A low-temperature CdTe ALD surface passivation process compatible with the process temperature requirement of the MCT alloy system was developed. This method suppressed out-gassing of Hg and vacancy formation which occurs at elevated temperatures. This work accomplished PA-ALD at 100°C, much lower than the thermal CdTe deposition previously demonstrated at temperatures higher than 200 °C. As past work in CdTe MOCVD has identified thermal decomposition of DMCd into Cd metal as the rate-limiting step and PA-ALD has been previously demonstrated to enable lowering the temperature of deposition for various processes, a PA-ALD CdTe process, and alternate chemistry processes were proposed to overcome the rate limiting step and to enable low-temp ALD.

8.2. Novel Contributions to the Field

Beginning with the work captured in Chapter 4, argon plasma was demonstrated to decompose the surface chemisorbed DMCd into Cd metal. Self-limited growth from DMCd, Ar plasma, and DETe was observed by in-situ SE. CdTe formation during ALD, along with native oxides of CdTe after exposure of ALD grown films to atmosphere, were observed by XPS. Island growth and coalescence were observed by AFM. A model to explain these observations was proposed: exposure of the starting substrate to DMCd leads to self-limited chemisorption of DMCd. This was followed by exposure to Ar plasma, which decomposed the DMCd exposed surface to Cd metal. This was then followed by exposure to DETe, which was catalytically decomposed by the Cd metal sites to form CdTe.

Chapter 5 demonstrated a similar catalytic decomposition of Te-precursor BTMSTe using Process A, which was the same process outlined in the previous paragraph, but had BTMSTe simply substituted for DETe as the tellurium precursor. Also, a temperature dependent GPC was observed by SE, with GPC decreasing with increasing substrate temperature. XPS revealed CdTe formation occurred in parallel with silicon, carbon, and oxygen contamination. TEM revealed CdTe island formation by lattice spacing measurements on the surface of Si native oxide, consistent with Chapter 4 growth model. Growth on MCT exhibited epitaxy in registry with the substrate, with evidence for partial native oxide at the ALD CdTe/MCT interface. Reduction of MCT by DMCd or Ar plasma was proposed to explain the partial MCT native oxide. Again, a model was proposed to explain the growth mechanism and presence of impurities: BTMSTe decomposes on Cd islands like DETe-based growth. However, incomplete decomposition and/or dissociative chemisorption of BTMSTe onto the growth surface leads to incorporation of impurities into the film and a site-passivating or -blocking effect which is more pronounced at higher temperatures.

Chapter 6 introduced Process B: the use of AcBr for direct co-reaction between it and either DMCd and BTMSTe. Evidence of co-reaction of AcBr and the growth surface by pulsing AcBr after the BMTSTe sub-cycle was observed as an increase in GPC on both Si and MCT substrates. A more linear thickness vs. time was observed by SE as compared to Process A. TEM revealed CdTe island formation. XPS revealed Br contamination, along with silicon, carbon, and oxygen. A growth model was proposed to explain the growth mechanism of Process B: similar to Process A, but the added AcBr reacts with silyl ligands, to unblock DMCd absorption sites. Also, direct thermal ALD was attempted by converting surface DMCd into cadmium bromide to co-react with BTMSTe silyl ligand by dehalosilinization, but this reaction was not successful.

Chapter 7 showed results from PCD experiments on samples of MCT that had been treated by either passivation, annealing, both or neither to compare the effect of surface treatments and bulk treatment on the effective minority carrier lifetime of the samples. In PCD the voltage is proportional to the carrier concentration, which enables extraction of the minority-carrier recombination lifetime after generation of eh pairs by illumination. A single temperature (77 K) PCD experiment demonstrated higher lifetime in ALD passivated and annealed samples, with surface passivation having a stronger effect on the lifetime. Temperature dependent (77 to 300 K) PCD experiments compared two samples: MBE grown vs. MBE grown then passivated by CdTe ALD (both samples were prepared by nominally the same wet chemistry). The passivated sample had higher lifetime through the extrinsic region (77 K to ~ 200 K), consistent with surface passivation. The trap level E_t along with SRH electron- and hole-lifetimes were extracted by fitting experimental data against the theoretical MCT temperature dependent lifetime. The passivated sample did not reach the theoretical limit (Auger and radiative lifetime limited value), indicating further development of the ALD process and a Hg overpressure anneal might still be needed to achieve these values.

8.3. Future Work

All demonstrations of ALD CdTe passivation of MCT should be characterized by PCD to demonstrate that the samples are surface, and not bulk, limited to provide conclusive observation of the effect of the passivation. This requires bulk limited starting material (i.e., high quality MCT epilayers that are Auger and Radiative recombination rate limited) that have passivated and unpassivated surfaces.

High-aspect ratio features should be fabricated and used as substrates to demonstrate conformal deposition across more challenging topography. However, planar samples must be used for any PCD experiments, as to decouple the fabrication processes used to make high-aspect ratio features from the ALD process itself.

The DETe process should be revisited to passivate the MCT surface for PCD experiments. AFM and cross-sectional TEM of various thicknesses of deposition should be pursued to highlight the growth mechanisms of the process using DETe. Additional AFM characterizations could illuminate the growth mechanism.

Thermally activated decomposition of DMCd is dependent on carrier gas choice.[29,90] Although this effect could be secondary to the substrate temperature, previous work on the temperature and carrier gas dependent thermodynamics has proven that using hydrogen rather than helium (or other “inert” gases [e.g., argon, nitrogen]) results in a lowering of the activation energy of deposition.[29] Growth of CdTe ALD under H_2 flow could provide lowering the temperature of decomposition of DMCd and hence thermal ALD temperature,[91] but remains as a future work.

Co-reaction between DMCd and AcBr should be further pursued. Introduction of an additional carrier gas, such as dichloromethane (DCM), could enable the reaction, followed by dehalosilinization of the bromide group by BTMSTe to form CdTe. Chamber pressure should be systematically studied to increase the flux of AcBr and DCM chemical on the growth surface. Measuring the GPC versus chamber pressure could illuminate whether chamber pressure (flux of AcBr to growth surface) can increase GPC.

Introduction of dichloromethane to a neat mixture of DMCd and BTMSTe analogs promotes direct co-reaction in the solvent phase.[49] Mimicking this in the vapor phase would enable thermal CdTe ALD. Direct co-reaction might suppress island formation as the metal island forming step is avoided. The effect of reactor pressure on GPC is the primary parameter to explore.

Also, Process B should be revised to include a simple, easy to test sub-cycle to mitigate any site-blocking effect of BTMSTe: after the plasma decomposition step, pulse DMCd and do not follow by Ar plasma. This may, through steric hindrance, block any BTMSTe from chemisorbing anywhere but on Cd metal, removing incorporation of Si and C into the growing film.

Finally, demonstrating effective passivation onto a photodiode array would be a step further toward application of the process.[92] Variable area diode arrays should be fabricated from MCT and passivated by ALD. This requires either implant of a dopant or in-situ doping during growth of MCT and etching of mesas to delineate pn junctions. Fabrication convolutes the effect of the ALD passivation process with all other fabrication process, so optimized fabrication is essential.

References

1 Capper, P. & Inspec. *Properties of narrow gap cadmium-based compounds*. (INSPEC, the Institution of Electrical Engineers, 1994).

2 Hansen, G. L. Energy gap versus alloy composition and temperature in Hg1−xCdxTe. *Journal of Applied Physics* **53**, 7099, doi:10.1063/1.330018 (1982).

3 Brice, J. C. & Capper, P. *Properties of mercury cadmium telluride*. (INSPEC, Institution of Electrical Engineers, 1987).

4 Mönch, W. *Semiconductor surfaces and interfaces*. Vol. 26 (Springer Science & Business Media, 2013).

5 Sze, S. M. *Semiconductor Devices: Physics and Technology*. (Wiley, 2001).

6 Nemirovsky, Y. & Bahir, G. Passivation of mercury cadmium telluride surfaces. *Journal of Vacuum Science & Technology A: Vacuum, Surfaces, and Films* **7**, 450-459 (1989).

7 Beck, J. D., Kinch, M. A., Esposito, E. J. & Chapman, R. A. THE MIS PHYSICS OF THE NATIVE OXIDE-HG1-XCDX TE INTERFACE. *Journal of Vacuum Science & Technology* **21**, 172-177, doi:10.1116/1.571706 (1982).

8 Kinch, M. in *Semiconductors and Semimetals* Vol. 18 313-378 (Elsevier, 1981).

9 Yang, M. J., Yang, C. H., Kinch, M. A. & Beck, J. D. Interface properties of HgCdTe metal-insulator-semiconductor capacitors. *Applied Physics Letters* **54**, 265, doi:10.1063/1.100985 (1989).

10 Nemirovsky, Y. & Rosenfeld, D. Surface passivation and 1/f noise phenomena in HgCdTe photodiodes. *Journal of Vacuum Science & Technology A: Vacuum, Surfaces, and Films* **8**, 1159-1166 (1990).

11 Kasap, S., Willoughby, A., Capper, P. & Garland, J. *Mercury Cadmium Telluride: Growth, Properties and Applications*. Vol. 38 (John Wiley & Sons, 2011).

12 Dhar, N. K. *et al.* in *Infrared Technololgy and Applications Xxix* Vol. 5074 *Proceedings of the Society of Photo-Optical Instrumentation Engineers (Spie)* (eds B. F. Andresen & G. F. Fulop) 157-165 (2003).

13 Reine, M., Sood, A. & Tredwell, T. Photovoltaic infrared detectors. *Semiconductors and semimetals* **18**, 201-311 (1981).

14 Reine, M. B., Krueger, E. E., O'Dette, P. & Terzis, C. L. in *GOES-8 and Beyond.* 501-518 (International Society for Optics and Photonics).

15 Dhar, N. K. & Tidrow, M. Z. in *Optical Science and Technology, the SPIE 49th Annual Meeting.* 34-43 (International Society for Optics and Photonics).

16 Robinson, J., Kinch, M., Marquis, M., Littlejohn, D. & Jeppson, K. in *Image Sensing Technologies: Materials, Devices, Systems, and Applications.* 91000I (International Society for Optics and Photonics).

17 Nemirovsky, Y., Rosenfeld, D., Adar, R. & Kornfeld, A. Tunneling and dark currents in HgCdTe photodiodes. *Journal of Vacuum Science & Technology A: Vacuum, Surfaces, and Films* **7**, 528-535 (1989).

18 Wijewarnasuriya, P. S., Lange, M. D., Sivananthan, S. & Faurie, J. P. CARRIER RECOMBINATION IN INDIUM-DOPED HGCDTE(211)B EPITAXIAL LAYERS GROWN

BY MOLECULAR-BEAM EPITAXY. *Journal of Applied Physics* **75**, 1005-1009, doi:10.1063/1.356506 (1994).

19 Pattison, J. & Wijewarnasuriya, P. Investigating the passivation of mercury cadmium telluride by atomic layer deposition of aluminum oxide. *Infrared Sensors, Devices, and Applications and Single Photon Imaging Ii* **8155**, 6, doi:10.1117/12.893760 (2011).

20 Suntola, T., Antson, J., Pakkala, A. & Lindfors, S. in *Proc. SID Symp. Dig. Tech. Papers.* 108-109.

21 Hanwell, M. D. *et al.* Avogadro: an advanced semantic chemical editor, visualization, and analysis platform. *Journal of cheminformatics* **4**, 17 (2012).

22 Cremers, V., Puurunen, R. L. & Dendooven, J. Conformality in atomic layer deposition: Current status overview of analysis and modelling. *Applied Physics Reviews* **6**, 021302, doi:10.1063/1.5060967 (2019).

23 Licausi, N., Rao, S. & Bhat, I. Low-Pressure Chemical Vapor Deposition of CdS and Atomic Layer Deposition of CdTe Films for HgCdTe Surface Passivation. *Journal of Electronic Materials* **40**, 1668-1673, doi:10.1007/s11664-011-1640-y (2011).

24 Bhat, I. B. Low temperature epitaxy of HgTe, CdTe, and HgCdTe using flow modulation techniques. *Journal of Vacuum Science & Technology B: Microelectronics and Nanometer Structures* **10**, 1376, doi:10.1116/1.585871 (1992).

25 Bhat, I. B., Taskar, N. R. & Ghandhi, S. K. ON THE MECHANISM OF GROWTH OF CDTE BY ORGANOMETALLIC VAPOR-PHASE EPITAXY. *Journal of the Electrochemical Society* **134**, 195-198, doi:10.1149/1.2100404 (1987).

26 Dakshinamurthy, S. & Bhat, I. S. Monitoring of CdTe Atomic Layer Epitaxy Using Spectroscopic Ellipsometry. *Journal of Electronic Materials* (1998).

27 Johs, B. D., D.; Pittal, S.; Bhat, I. B.; Dakshinamurthy, S. <Real-time monitoring and control during MOVPE growth of CdTe using multiwavelength ellipsometry.pdf>. *Thin Solid Films* **233**, 4 (1993).

28 Wang, W., Ehsani, H. & Bhat, I. Atomic layer epitaxy of CdTe on GaAs, by organometallic vapor phase epitaxy. *Journal of crystal growth* **124**, 670-675 (1992).

29 Liu, B. C., McDaniel, A. H. & Hicks, R. F. MODELING OF THE COUPLED KINETICS AND TRANSPORT IN THE ORGANOMETALLIC VAPOR-PHASE EPITAXY OF CADMIUM TELLURIDE. *Journal of Crystal Growth* **112**, 192-202, doi:10.1016/0022-0248(91)90924-t (1991).

30 Irvine, S. & Bajaj, J. A study of the growth kinetics of II–VI metalorganic vapour phase epitaxy using in situ laser reflectometry. *Journal of crystal growth* **145**, 74-81 (1994).

31 Baker, L. *et al.* Nucleation and growth of Pt atomic layer deposition on Al2O3 substrates using (methylcyclopentadienyl)-trimethyl platinum and O2 plasma. *Journal of Applied Physics* **109**, 084333 (2011).

32 Kwon, O.-K., Kwon, S.-H., Park, H.-S. & Kang, S.-W. PEALD of a ruthenium adhesion layer for copper interconnects. *Journal of The Electrochemical Society* **151**, C753-C756 (2004).

33 Kumar, N., Yanguas-Gil, A., Daly, S. R., Girolami, G. S. & Abelson, J. R. Remote plasma treatment of Si surfaces: Enhanced nucleation in low-temperature chemical vapor deposition. *Applied Physics Letters* **95**, 144107 (2009).

34 Niwano, M., Terashi, M. & Kuge, J. Hydrogen adsorption and desorption on Si (100) and Si (111) surfaces investigated by in situ surface infrared spectroscopy. *Surface Science* **420**, 6-16 (1999).

35 Knapas, K. & Ritala, M. In Situ Studies on Reaction Mechanisms in Atomic Layer Deposition. *Critical Reviews in Solid State and Materials Sciences* **38**, 167-202, doi:10.1080/10408436.2012.693460 (2013).

36 Seo, B., Kim, J. & You, S. Effects of argon gas pressure on its metastable-state density in high-density plasmas. *Physics of Plasmas* **22**, 053514 (2015).

37 Lee, Y.-K., Moon, S.-Y., Oh, S.-J. & Chung, C.-W. Determination of metastable level densities in a low-pressure inductively coupled argon plasma by the line-ratio method of optical emission spectroscopy. *Journal of Physics D: Applied Physics* **44**, 285203 (2011).

38 Breaux, L., Anthony, B., Hsu, T., Banerjee, S. & Tasch, A. Homoepitaxial films grown on Si (100) at 150 C by remote plasma-enhanced chemical vapor deposition. *Applied Physics Letters* **55**, 1885-1887 (1989).

39 Sakuraba, M., Muto, D., Seino, T. & Murota, J. Si atomic layer-by-layer epitaxial growth process using alternate exposure of Si(1 0 0) to SiH4 and to Ar plasma. *Applied Surface Science* **212-213**, 197-200, doi:https://doi.org/10.1016/S0169-4332(03)00072-2 (2003).

40 Franek, J., Nogami, S., Demidov, V., Koepke, M. & Barnat, E. Correlating metastable-atom density, reduced electric field, and electron energy distribution in the post-transient stage of a 1-Torr argon discharge. *Plasma Sources Science and Technology* **24**, 034009 (2015).

41 Chen, F. F. *Introduction to plasma physics*. (Springer Science & Business Media, 2012).

42 Miessler, G., Fischer, P. & Tarr, D. (New York: Pearson Education, Inc, 2014).

43 Carter, R. L. *Molecular symmetry and group theory*. (Wiley New York, 1998).

44 Tanskanen, J. T., Bakke, J. R., Bent, S. F. & Pakkanen, T. A. Molecular level insights into atomic layer deposition of CdS by quantum chemical calculations. *The Journal of Physical Chemistry C* **114**, 16618-16624 (2010).

45 Stinespring, C. & Freedman, A. Surface chemistry of dimethyl cadmium and dimethyl tellurium at 295 K. *Chemical physics letters* **143**, 584-588 (1988).

46 Pore, V., Hatanpaa, T., Ritala, M. & Leskela, M. Atomic layer deposition of metal tellurides and selenides using alkylsilyl compounds of tellurium and selenium. *Journal of the American Chemical Society* **131**, 3478-3480 (2009).

47 Gwon, T. *et al.* Atomic Layer Deposition of GeTe Films Using Ge {N [Si (CH3) 3] 2} 2,{(CH3) 3Si} 2Te, and Methanol. *Chemistry of Materials* **28**, 7158-7166 (2016).

48 Gwon, T. *et al.* Atomic Layer Deposition of GeTe Films Using Ge{N[Si(CH3)3]2}2, {(CH3)3Si}2Te, and Methanol. *Chemistry of Materials* **28**, 7158-7166, doi:10.1021/acs.chemmater.6b03704 (2016).

49 Stuczynski, S. M., Brennan, J. G. & Steigerwald, M. L. Formation of metal-chalcogen bonds by the reaction of metal-alkyls with silyl chalcogenides. *Inorganic Chemistry* **28**, 4431-4432, doi:10.1021/ic00324a001 (1989).

50 Rayner, G. B. (Google Patents, 2017).

51 Tompkins, H. & Irene, E. A. *Handbook of ellipsometry*. (William Andrew, 2005).

52 Woollam, C. J. *M-2000 Ellipsometer*, <https://www.jawoollam.com/products/m-2000-ellipsometer> (2020).

53 Fairley, N. & Casa Software, L. *CasaXPS manual 2.3.15 : CasaXPX processing software for XPS spectra*. (Casa Software Ltd., 2009).

54 Kowalski, B., Orłowski, B. & Ghijsen, J. XPS study of CdTe (110) surface oxidation process. *Surface science* **412**, 544-554 (1998).

55 Blakemore, J. S. *Semiconductor statistics*. (Courier Corporation, 2002).

56 Rein, S. *Lifetime spectroscopy: a method of defect characterization in silicon for photovoltaic applications*. Vol. 85 (Springer Science & Business Media, 2006).

57 Lopes, V., Wright, W. & Syllaios, A. Characterization of (Hg, Cd) Te by the photoconductive decay technique. *Journal of Vacuum Science & Technology A* **8**, 1167-1170 (1990).

58 Lopes, V., Syllaios, A. & Chen, M. Minority carrier lifetime in mercury cadmium telluride. *Semiconductor Science and Technology* **8**, 824 (1993).

59 Wijewarnasuriya, P. S., Lange, M. D., Sivananthan, S. & Faurie, J. P. MINORITY-CARRIER LIFETIME IN INDIUM-DOPED HGCDTE(211)B EPITAXIAL LAYERS GROWN BY MOLECULAR-BEAM EPITAXY. *Journal of Electronic Materials* **24**, 545-549, doi:10.1007/bf02657961 (1995).

60 Rein, S., Rehrl, T., Warta, W. & Glunz, S. Lifetime spectroscopy for defect characterization: Systematic analysis of the possibilities and restrictions. *Journal of Applied Physics* **91**, 2059-2070 (2002).

61 Schroder, D. K. *Semiconductor material and device characterization*. (John Wiley & Sons, 2015).

62 Barnaal, D. *Analog Electronics for Scientific Application*. (Waveland Press, 1989).

63 Kim, K.-C. *et al.* Metalorganic Chemical Vapor Deposition of CdTe(133) Epilayers on Si(211) Substrates. *Journal of Electronic Materials* **39**, 863-867, doi:10.1007/s11664-010-1220-6 (2010).

64 Stoltz, A., Benson, J. & Smith, P. Plasma Passivation Etching for HgCdTe. *Journal of electronic materials* **38**, 1741-1745 (2009).

65 Bergmann, C. P. & Machado, F. M. *Carbon nanomaterials as adsorbents for environmental and biological applications*. (Springer, 2015).

66 Pattison, J. & Wijewarnasuriya, P. Investigating the passivation of mercury cadmium telluride by atomic layer deposition of aluminum oxide. *Infrared Sensors, Devices, and Applications and Single Photon Imaging Ii* **8155**, doi:10.1117/12.893760 (2011).

67 Wagner, C. *et al.* NIST standard reference database 20, Version 3.4 (Web version). *National Institute of Standards and Technology: Gaithersburg, MD* **20899** (2003).

68 Eaton, P. & West, P. *Atomic force microscopy*. (Oxford university press, 2010).

69 Elam, J., Zinovev, A., Pellin, M. J., Comstock, D. J. & Hersam, M. C. Nucleation and growth of noble metals on oxide surfaces using atomic layer deposition. *ECS Transactions* **3**, 271 (2007).

70 Richey, N. E., de Paula, C. & Bent, S. F. Understanding chemical and physical mechanisms in atomic layer deposition. *The Journal of Chemical Physics* **152**, 040902 (2020).

71 Fang, Q., Hodson, C., Xu, C. & Gunn, R. Nucleation and growth of platinum films on high-k/metal gate materials by remote plasma and thermal ALD. *Physics Procedia* **32**, 551-560 (2012).

72 Knoops, H. *et al.* Remote plasma ALD of platinum and platinum oxide films. *Electrochemical and Solid State Letters* **12**, G34 (2009).

73 Adamson, A. W. & Gast, A. P. *Physical chemistry of surfaces*. Vol. 150 (Interscience publishers New York, 1967).

74 Eom, T. *et al.* Conformal Formation of (GeTe2)(1–x)(Sb2Te3)x Layers by Atomic Layer Deposition for Nanoscale Phase Change Memories. *Chemistry of Materials* **24**, 2099-2110, doi:10.1021/cm300539a (2012).

75 Chu, T., Chu, S. S. & Ang, S. Surface passivation and oxidation of cadmium telluride and properties of metal-oxide-CdTe structures. *Journal of applied physics* **58**, 3206-3210 (1985).

76 Pore, V., Hatanpää, T., Ritala, M. & Leskelä, M. Atomic Layer Deposition of Metal Tellurides and Selenides Using Alkylsilyl Compounds of Tellurium and Selenium. *Journal of the American Chemical Society* **131**, 3478-3480, doi:10.1021/ja8090388 (2009).

77 Chen, R., Kim, H., McIntyre, P. C. & Bent, S. F. Controlling Area-Selective Atomic Layer Deposition of HfO2 Dielectric by Self-assembled Monolayers. *MRS Proceedings* **811**, D3.3, doi:10.1557/PROC-811-D3.3 (2004).

78 Cheng, L., Adinolfi, V., Weeks, S. L., Barabash, S. V. & Littau, K. A. Conformal deposition of GeTe films with tunable Te composition by atomic layer deposition. *Journal of Vacuum Science & Technology A: Vacuum, Surfaces, and Films* **37**, 020907 (2019).

79 Gwon, T. *et al.* Atomic Layer Deposition of GeTe and Ge–Sb–Te Films Using HGeCl3, Sb(OC2H5)3, and {(CH3)3Si}2Te and Their Reaction Mechanisms. *Chemistry of Materials* **29**, 8065-8072, doi:10.1021/acs.chemmater.7b01236 (2017).

80 Zakirov, E. R. *et al.* XPS investigation of the ALD Al2O3/HgCdTe heterointerface. *Semiconductor Science and Technology* **34**, 065007 (2019).

81 Voitsekhovskii, A. *et al.* Diffusion-limited dark currents in mid-wave infrared HgCdTd-based nBn structures with Al2O3 passivation. *Journal of Physics D: Applied Physics* **53**, 055107 (2019).

82 BENNEVILLE, P. L. d. The synthesis of keto acids and ketones by the reaction of acid anhydrides with cadmium alkyls. *The Journal of Organic Chemistry* **6**, 462-466 (1941).

83 Cason, J. The use of organocadmium reagents for the preparation of ketones. *Chemical reviews* **40**, 15-32 (1947).

84 Severengiz, T., du Mont, W. W., Lenoir, D. & Voss, H. Novel Reactions of Acyl Halides with Bis (trimethylsilyl) Telluride: C, Te and C, C Bond Formation. *Angewandte Chemie International Edition in English* **24**, 1041-1042 (1985).
85 Wells, R. L., Aubuchon, S. R., Kher, S. S., Lube, M. S. & White, P. S. Synthesis of nanocrystalline indium arsenide and indium phosphide from indium (III) halides and tris (trimethylsilyl) pnicogens. Synthesis, characterization, and decomposition behavior of I3In. cntdot. P (SiMe3) 3. *Chemistry of materials* **7**, 793-800 (1995).
86 Wells, R. L. *et al.* The use of tris (trimethylsilyl) arsine to prepare gallium arsenide and indium arsenide. *Chemistry of Materials* **1**, 4-6 (1989).
87 Isaacs, N. S. *Physical organic chemistry*. (Longman Scientific & Technical, 1995).
88 Petrash, G., Markova, S. & Zemskov, K. Role of ion-ion recombination in population of triplet resonance levels of cadmium and mercury. *Bulletin of the Lebedev Physics Institute* **35**, 368-372 (2008).
89 Weber, J., Hansen, T., Van de Sanden, M. & Engeln, R. B-spline parametrization of the dielectric function applied to spectroscopic ellipsometry on amorphous carbon. *Journal of Applied Physics* **106**, 123503 (2009).
90 Stringfellow, G. B. *Organometallic vapor-phase epitaxy: theory and practice*. (Elsevier, 1999).
91 Mullin, J., Irvine, S. & Ashen, D. Organometallic growth of II–VI compounds. *Journal of Crystal Growth* **55**, 92-106 (1981).
92 Gopal, V. Variable-area diode data analysis of surface and bulk effects in HgCdTe photodetector arrays. *Semiconductor science and technology* **9**, 2267 (1994).